Aspect of classical density functional theory: crystals and interfaces in hard–disk systems and the problem of constructing functionals using machine learning methods

Dissertation
der Mathematisch-Naturwissenschaftlichen Fakultät
der Eberhard Karls Universität Tübingen
zur Erlangung des Grades eines
Doktors der Naturwissenschaften
(Dr. rer. nat.)

vorgelegt von
Shang–Chun Lin
aus Tainan/ Taiwan

Tübingen
2020

Gedruckt mit Genehmigung der Mathematisch-Naturwissenschaftlichen Fakultät
der Eberhard Karls Universität Tübingen.

Tag der mündlichen Qualifikation: 12.02.2021
Stellvertretender Dekan: Prof. Dr. József Fortágh
1. Berichterstatter: Prof. Dr. Martin Oettel
2. Berichterstatter: Prof. Dr. Roland Roth

List of published work

Most results of this thesis have already been published in academic journals, and the corresponding publications are listed as following.

Phase diagrams and crystal–fluid surface tensions in additive and nonadditive two–dimensional binary hard–disk mixtures
Shang-Chun Lin and Martin Oettel, Physical Review E 98.1.012608 (2018), DOI: 10.1103/PhysRevE.98.012608

Abstract: Using density functionals from fundamental measure theory, phase diagrams and crystal–fluid surface tensions in additive and nonadditive (Asakura–Oosawa model) two–dimensional binary hard–disk mixtures are determined for the whole range of size ratios q=small diameter/large diameter, assuming random disorder (lattice points or interstitial occupied by large or small disks at random) in the crystal phase. The fluid–crystal transitions are first order due to the assumption of a periodic unit cell in the density–functional calculations. Qualitatively, the shape of the phase diagrams is similar to the case of three–dimensional hard–sphere mixtures. For the nonadditive case, a broadening of the fluid–crystal coexistence region is found for small q, whereas for large q a vapor–fluid transition intervenes. In the additive case, we find a sequence of spindle , azeotropic, and eutectic phase diagrams upon lowering q from 1 to 0.6. The transition from azeotropic to eutectic is different from the three–dimensional case. Surface tensions in general become smaller (up to a factor 2) upon the addition of a second species and they are rather small. The minimization of the functionals proceeds without restrictions and optimized graphics card routines are used.

Statement of the author: Motivated by the successful results for one–component hard–sphere systems, we systematically investigated crystal–fluid interfaces and phase diagrams in binary hard–disk systems.

A classical density functional from machine learning and a convolutional neural network

Shang-Chun Lin and Martin Oettel, SciPost Phys. 6, 025 (2019),
DOI: 10.21468/SciPostPhys.6.2.025

Abstract: We use machine learning methods to approximate a classical density functional. As a study case, we choose the model problem of a Lennard Jones fluid in one dimension where there is no exact solution available and training data sets must be obtained from simulations. After separating the excess free energy functional into a "repulsive" and an "attractive" part, machine learning finds a functional in weighted density form for the attractive part. The density profile at a hard wall shows good agreement for thermodynamic conditions beyond the training set conditions. This also holds for the equation of state if it is evaluated near the training temperature. We discuss the applicability to problems in higher dimensions.

Statement of the author: I used a convolutional network to learn the explicit excess free energy functional. The idea was completely new and I have had built it from the ground up. Since I was lack of knowledge of machine learning at the time, the functionals are limited to simple polynomial ansätze and the training process was written purely by `Numpy`, which is incredibly slow comparing to the later work. However, the results are better than we expected and thus prove the point that it is possible to approximate unknown functionals explicitly by machine learning.

Analytical classical density functionals from an equation learning network

Shang-Chun Lin, Georg Martius and Martin Oettel, J. Chem. Phys. 152, 021102 (2020),
DOI: 10.1063/1.5135919

Abstract: We explore the feasibility of using machine learning methods to obtain an analytic form of the classical free energy functional for two model fluids, hard rods and Lennard–Jones, in one dimension . The Equation Learning Network proposed in Ref. [1] is suitably modified to construct free energy densities which are functions of a set of weighted densities and which are built from a small number of basis functions with flexible combination rules. This setup considerably enlarges the functional space used in the machine learning optimization as compared to previous work [2] where the functional is limited to a simple polynomial form. As a result, we find a good approximation for the exact hard–rod functional and its direct correlation function. For the Lennard–Jones fluid, we let the network learn (i) the full excess free energy functional and (ii) the excess free energy functional related to interparticle attractions. Both functionals show a good agreement with simulated density profiles for thermodynamic parameters inside and outside the training region.

Statement of the author: With the previous successful work, Martin and I collaborated with Dr. Georg Martius to extend the feasibility and reliability of the network. The functional can have complex representations with simple basis functions. The training process was written by `Tensorflow` and `Sympy` with GPU (graphics processing unit) accelerated. The results and the speed of the training process are significantly improved comparing to the previous work. Even though there is still a lot of room to improve, I believe it could be the future for approximating unknown functionals.

Abstract

The theoretical studies reported in this thesis are mainly concerned with two topics in classical density functional theory (DFT). First, we investigate the crystal–fluid interface and phase transitions in hard–disk systems. Second, we propose a novel machine learning architecture, the *Functional Equation Learner*, to obtain an explicit free energy functional directly from equilibrium density distributions in the presence of different external potentials.

For this purpose, we briefly introduce DFT and Fundamental Measure Theory (FMT). DFT is an approach for evaluating the free energy based on particle density distributions, and FMT is a particular instance of DFT for hard spheres in three, two and one dimensions, which gives highly accurate (in two and three dimensions) or exact (in one dimension) descriptions of homogeneous and inhomogeneous systems. For two–dimensional hard spheres (hard disks), we use the free energy functional based on FMT proposed by Roth *et al.* [3], which has been previously reported to show accurate thermodynamic properties for a triangular crystalline structure and crystal–fluid coexistence densities compared to Monte–Carlo simulations.

For one–component hard–disk systems, our result for the surface tension of a crystal–liquid interface is in good agreement with experiments, and the melting transition is investigated. As has been confirmed in past years, the melting transition for hard disks proceeds via the formation of a "hexatic" phase. In our numerical experiment, the characteristics of a hexatic phase, i.e. dislocations, are found. Furthermore, we model genuine hard–disk mixtures and mixtures of hard disks with non–additive polymers to obtain phase diagrams and surface tensions. For genuine hard–disk mixtures, the phase diagrams are qualitatively very similar to those of three–dimensional hard spheres, where the sequence of types of phase diagrams spindle $\rightarrow$ azeotropic $\rightarrow$ eutectic is observed upon lowering the small size ratio from 1 to 0.6. For non–additive mixtures, the free energy functional is linearized with respect to the polymer density, which is analogous to a known DFT approach to the three–dimensional Asakura–Oosawa model. In this case, the typical continuous widening of the coexistence gap between fluid and solid is observed upon

the addition of the smaller species. For the surface tension, it shows that the addition of a second component leads in general to a substantial decrease for both genuine and non–additive hard–disk mixtures.

Furthermore, despite that FMT provides highly accurate free energy functionals for hard particles, a FMT like treatment for a non–vanishing interaction outside the hard core is missing. In general, in such a case, the analytical form of the free energy functional is unknown; therefore we adopt the recently introduced equation learning network [1] and propose the *Functional Equation Learner* (FEQL) for this task. With flexible combination rules, composite functions from the FEQL are built from a number of basis functions and a set of weighted densities. The training, i.e. tuning the parameters in functions, is automatically done by minimizing the Euclidean distance between predicted and exact/simulated density distributions. As a result, we find well approximated free energy functionals for the hard–rod fluid (exact functional is known) and the Lennard–Jones fluid (exact functional is unknown). In both cases, the density profiles, equation of states, and the direct correlation functions delivered by the learned functionals are in good agreement with exact/simulated results, even outside the training regions.

Zusammenfassung

Die theoretischen Studien, über die in dieser Arbeit berichtet wird, befassen sich hauptsächlich mit zwei Themen der klassischen Dichtefunktionaltheorie (DFT). Zunächst untersuchen wir die Kristall-Fluid-Grenzfläche und Phasenübergänge in Harte–Scheiben–Systemen. Zweitens, stellen wir eine neuartige maschinelle Lernarchitektur vor, den *Functional Equation Learner*, um explizit Funktionale der freien Energie zu erhalten, welche direkt aus Gleichgewichtsdichteverteilungen unter dem Einfluss verschiedener externer Potentiale berechnet werden.

Zu diesem Zweck stellen wir die DFT und die *Fundamental Measure Theory* (FMT) kurz vor. Die DFT ist ein Ansatz zur Berechnung der freien Energie auf der Grundlage von Partikeldichteverteilungen, und die FMT ist eine besondere Ausprägung der DFT für harte Kugelnn in drei, zwei und einer Dimension(en), die eine hochgenaue (in zwei und drei Dimensionen) oder exakte (in einer Dimension) Beschreibung von homogenen und inhomogenen Systemen liefert. Für zweidimensionale harte Kugeln (harte Scheiben) verwenden wir das von Roth *et al.* [3] vorgeschlagene Funktional der freien Energie auf der Grundlage der FMT, wovon bereits früher berichtet wurde, dass es im Vergleich zu Monte–Carlo–Simulationen genaue thermodynamische Eigenschaften für eine dreieckige kristalline Struktur und Kristall–Fluid–Koexistenzdichten vorhersagt.

Für einkomponentige Harte–Scheiben–Systeme ist unser Ergebnis für die Oberflächenspannung einer Kristall–Flüssigkeits-Grenzfläche in guter Übereinstimmung mit Experimenten, ausserdem wird der Schmelzübergang untersucht. Wie in den vergangenen Jahren bestätigt wurde, verläuft der Schmelzübergang bei Harten–Scheiben über die Bildung einer “hexatischen” Phase. In unserem numerischen Experiment werden die Eigenschaften einer hexatischen Phase, z.B. Dislokationen, gefunden. Darüber hinaus modellieren wir Harte–Scheiben–Mischungen und Mischungen von Harte–Scheiben mit nicht–additiven Polymeren, um Phasendiagramme und Oberflächenspannungen zu erhalten. Für additive Harte–Scheiben–Mischungen sind die Phasendiagramme qualitativ sehr ähnlich denen von dreidimensionalen Harte–Kugeln–

Systemen, wobei die Abfolge von Phasendiagrammen des Types spindelförmig → azeotropen → eutektischen beim Absenken des Größenverhältnisses der kleinen Spezies von 1 auf 0.6 beobachtet wird. Für nicht–additive Mischungen wird das Freie–Energie–Funktional in Bezug auf die Polymerdichte linearisiert, was analog zu einem bekannten DFT–Ansatz des drei–dimensionalen Asakura–Oosawa–Modells geschieht. In diesem Fall wird die typische kontinuierliche Vergrößerung der Koexistenzlücke zwischen Flüssigkeit und Festkörper bei der Zugabe der kleineren Spezies beobachtet. Für die Oberflächenspannung zeigt sich, dass die Zugabe einer zweiten Komponente im Allgemeinen zu einer erheblichen Abnahme sowohl bei additiven als auch bei nicht–additiven Harte–Scheiben–Mischungen führt.

Obwohl die FMT hochpräzise Funktionale der freien Energie für harte Teilchen liefert, fehlt eine FMT–ähnliche Methode für die Wechselwirkung außerhalb des harten Kerns. Im Allgemeinen ist in einem solchen Fall die analytische Form des Freie–Energie–Funktionals unbekannt; daher übernehmen wir das kürzlich eingeführte Gleichungslern–Netzwerk [1] und stellen den *Functional Equation Learner* (FEQL) für diese Aufgabe vor. Mit flexiblen Kombinationsregeln werden zusammengesetzte Funktionen aus dem FEQL aus einer Reihe von Basisfunktionen und einem Satz gewichteter Dichten gebildet. Das Training, d.h. die Abstimmung der Parameter in Funktionen, erfolgt automatisch durch Minimierung des euklidischen Abstands zwischen vorhergesagten und exakten/simulierten Dichteverteilungen. Als Ergebnis finden wir gut approximierte Funktionale der freien Energie für das Harte–Stäbchen–Fluid (das genaue Funktional ist bekannt) und das Lennard-Jones-Fluid (das genaue Funktional ist unbekannt). In beiden Fällen stimmen die Dichteprofile, die Zustandsgleichungen und die direkten Korrelationsfunktionen, die von den gelernten Funktionalen geliefert werden, mit den exakten/simulierten Ergebnissen überein, auch außerhalb der Trainingsregionen.

Contents

Chapter 1

Introduction

God made the bulk; the surface was invented by the devil.
– Wolfgang Pauli

If we would like to make something that runs rapidly over the ground, then we could watch a cheetah running, and we could try to make a machine that runs like a cheetah. But, it's easier to make a machine with wheels.
– Richard Feynman

Surfaces or interfaces are the locations for many phenomena between the material and its environment, where all physical and chemical interactions and exchanges take place. To observe interfaces, colloidal systems serve as important tools and model systems. The length scale of colloidal systems is micrometers; thus, single–particle resolution can be achieved, for example, by confocal microscopy. More importantly, the pairwise interaction between the particles makes it possible to study the system by methods of classical statistical mechanics, e.g. Monte–Carlo simulation or density functional theory (DFT). As a result, the one–to–one comparison between experiments and classical statistical mechanics is possible.

In colloidal systems, the interaction is usually composed of a the short–ranged harsh repulsion and long–ranged smooth attraction. The short–range repulsion plays a crucial role as it determines the main structure of the liquid and crystal phase. Therefore, hard spheres (HS), where the harsh short–range repulsion forbids overlaps, serves as an important reference system. As there is no attraction between HS particles, the crystal–fluid transition is purely induced by entropy.

For a theoretical understanding of HS, density functional theory (DFT) is a very important tool which gives a description of both microsopic and macrosopic (bulk) properties in equilibrium. The challenge of DFT is to

approximate the free energy as precisely as possible. In 1989, Rosenfeld introduced fundamental measure theory (FMT) as a DFT treatment for HS mixtures in three, two and one dimension [4, 5]. During the next two decades, the FMT has been further developed and gives almost exact results in comparison with simulations [3, 6, 7, 8].

Unfortunately, such success is missing with respect to the long–ranged smooth attraction. In DFT, the attractions are usually treated as a perturbation; however, for low enough temperatures, attractions can dominate over repulsions and thus perturbative treatments, such as the mean–field approximation, are able to deliver a qualitative description but usually are quantitatively inaccurate, or require more effort [9]. Recently, with the great improvement of computational hardware, machine learning methods have been developed and used to give computers the ability to analyze patterns within a given data set without programming explicitly. For DFT, this implies the possibility to learn the free energy functionals by inputs, for instance, one–body density distributions and external potentials, without the explicit knowledge of many–body correlations.

In this thesis, after a brief introduction of thermodynamics and statistical physics in Chapter 2, the DFT approaches to the excess free energy relevant to this thesis are introduced in Chapter 3. The main results are split into two parts: fluid–crystal transitions and interfaces of two–dimensional hard–disk mixtures (Chapter 4 and 5), and machine learning functionals of one–dimensional fluids (Chapter 6 and 7).

Two–dimensional hard–disk mixtures

In two–dimensional (2D) systems, the fluid–crystal transition of hard–disk mixtures has been of fundamental interest over the past years. Only recently, it has been established in the one–component system by simulations [10] and experiments [11] that the transition happens via a first–order transition from the fluid to the hexatic phase and a continuous transition from the hexatic to the crystal phase. Although the crystal phase is not strictly periodic (it does not have infinitely long–ranged positional order), in simulations and experiments it has practically the appearance of a conventional, periodic crystal.

By using the density functional from fundamental measure theory proposed in Ref. [3], which gives a very accurate description of fluid structure in one– and two–component systems[12], the phase diagrams and crystal–fluid surface tensions in two–dimensional hard–disk binary mixtures are determined. The minimization of the functionals proceeds without restrictions.

For one–component hard disks, the thermodynamic properties at coex-

istence and crystal–fluid surface tensions are close to simulations [10] and experiments [11]. Also, the anisotropy of surface tensions are determined which, however, is about one magnitude smaller than in experiments [11]. Furthermore, we investigate the hexatic phase by measuring the pair correlation function in large systems, here, the results are not conclusive with regard to a connect DFT description of the hexatic phase.

For mixtures, we consider a simple binary mixture of large (l) and small (s) disks, with diameter σ_l and σ_s, respectively, and $q = \frac{\sigma_\mathrm{s}}{\sigma_\mathrm{l}}$ denoting the size ratio. In the case of an additive system (denoted as HD mixture), one may define an interaction diameter $d_{ij} = \sigma_i/2 + \sigma_j/2$ with $i, j = \{\mathrm{l}, \mathrm{s}\}$. The pair potential $\Phi^{ij}(r)$ between two particles with center-center distance r is ∞ for $r < d_{ij}$ and 0 for $r > d_{ij}$. In addition, we consider a non additive mixture in which the interaction between two small disks is zero, i.e. they behave as an ideal gas and the other interactions (large–large and large–small) remain unchanged. This mixture is the 2D variant [13] of the well–known Asakura–Oosawa (AO) model [14, 15]. For the nonadditive case, a broadening of the fluid–crystal coexistence region is found for small q whereas for higher q a vapor–fluid transition intervenes. In the additive case, we find a sequence of spindle type, azeotropic and eutectic phase diagrams upon lowering q from 1 to 0.6. The transition from azeotropic to eutectic is different from the three–dimensional case. Surface tensions in general are rather small and become smaller (up to a factor 2) upon addition of a second species.

Machine learning functionals

The art of DFT is the construction of free energy functionals. The density distributions are computed by self–consistent equations involving functional derivatives of these free energy functionals, and these equations are solvable with much less numerical effort than obtaining density distributions in simulations. Furthermore, all equilibrium and even some non–equilibrium properties are based on the free energy functionals. Despite the great principle power of the approach, the exact free energy functionals are not known in general, therefore considerable effort has gone into the theoretical development of functionals. As mentioned, the functionals derived from FMT have a high degree of accuracy for hard particles, but for the interactions outside the hard core, a qualitatively new and successful ansatz is missing.

In recent years, some effort has gone into approximating ("learning") functionals by machine learning (ML) techniques. In quantum DFT, e.g., interpolating functionals generated by kernel ridge regression have been tested for model 1D systems [16, 17] and also have been extended to 3D systems [18]. Numerically interpolated functionals do not contain sufficient information

about functional gradients, therefore both the energy–density map and the external potential–density maps had to be learned by interpolation [17]. For the 1D Hubbard model, a convolutional network functional has been learned whose numerical functional derivative appears to be more robust [19]. However, these approaches hide the energy functional inside an "ML black box" which does not permit much insight from a theory perspective. For the classical case, a 1D LJ–like fluid was studied by us with a convolutional network [2], utilizing an established approach from liquid state theory of splitting the excess free energy functional into a "repulsion" part and an "attraction" part $\mathcal{F}^{\text{att}}$ [2]. The convolutional network naturally leads to an approximation of $\mathcal{F}^{\text{att}}$ in terms of weighted densities n_i, which are the essential building blocks in modern classical DFT; however, the free energy density $\mathfrak{f}^{\text{ex}}_{\text{att}}(n_i)$ as a function of n_i had to be prescribed as simple polynomials. An interpretable results obtained in [2] was the accurate splitting of the interaction potential in the Weeks–Chandler–Andersen (WCA) spirit [20].

In this context, the question naturally arises whether ML techniques can be used to learn analytic forms of (free) energy functionals instead of "black boxes" or presumed forms. This question is important also in a more general context: can ML algorithms contribute to theory building in physics? In the ML community, efforts in that direction have utilized genetic algorithms to search a space of simple basis function with multiplication and addition rules [21]. More recent work by us proposes an equation learning network employing gradient-based optimization with simple basis functions and division besides multiplication/addition as combination rules [1, 22]. An empirical principle for the "right" formula (choose the simplest one that still predicts well, i.e. Occam's razor) can be built into the loss function. This principle was also successful in the history of physics in finding analytical models with high predictive power even outside the training/observed regime. For the DFT problem, the extrapolation power to other external potentials is an important aspect, as well as the analytic differentiability of the free energy functional since structural information about the fluid (pair correlations) is obtained via the direct correlation function (two functional derivatives of the excess free energy functional).

These aspects are explored for the model cases of a hard–rod (HR) and a Lennard–Jones (LJ) fluid in 1D. As a result, we find a good approximation for the exact hard–rod functional and its direct correlation function. For the Lennard–Jones fluid, we let the network learn (i) the full excess free energy functional and (ii) the excess free energy functional related to interparticle attractions. Both functionals show a good agreement with simulated density profiles for thermodynamic parameters inside and outside the training region.

Chapter 2

Thermodynamics and statistical physics

In this chapter, only essential ingredients are introduced. We refer to the book *Theory of simple liquids* [23] for readers who have a deeper interest.

A D–dimensional system with N particles has $2 \times D \times N$ coordinates in phase space, i.e. the positions $\mathbf{r}^N = (\mathbf{r}_1, \mathbf{r}_2 ... \mathbf{r}_N)$ and momenta $\mathbf{p}^N = (\mathbf{p}_1, \mathbf{p}_2 ... \mathbf{p}_N)$ with $\mathbf{r}_i$ and $\mathbf{p}_i$ the location and momentum of particle i. Let $\Gamma = (\mathbf{r}_1 ... \mathbf{r}_N, \mathbf{p}_1, ..., \mathbf{p}_N; N)$ denote a point in phase space; more precisely, Γ is called 'microstate' or 'configuration' of the system. The average value $\langle O \rangle$ of an observable $O(\Gamma)$ is defined by

$$\langle O \rangle = \sum_{\Gamma} O(\Gamma) f(\Gamma) \equiv \mathrm{tr}_{\mathrm{cl}} O(\Gamma) f(\Gamma) \tag{2.1}$$

with $f(\Gamma)$ the probability in phase space and $\mathrm{tr}_{\mathrm{cl}}$ the classical trace (the summation over all possible configurations), as defined in Eqs. (2.9) and (2.14) below for different ensembles.

In equilibrium, the explicit expression for the phase space probability f_{eq} can be obtained from the Gibbs principle of maximum (Shannon) entropy S, which is defined as

$$S = \max \left(-k_{\mathrm{B}} \left\langle \ln \left(f_{\mathrm{eq}} \right) \right\rangle \right) = -k_{\mathrm{B}} \mathrm{tr}_{\mathrm{cl}} f_{\mathrm{eq}} \ln(f_{\mathrm{eq}}). \tag{2.2}$$

The Hamiltonian $\mathcal{H}$ of a system is a sum of the kinetic energy $\mathcal{T}$, interparticle potential energy $\mathcal{U}$, and the external potential $\mathcal{V}^{\mathrm{ext}}$; i.e.,

$$\mathcal{H}(\mathbf{r}^N, \mathbf{p}^N) = \mathcal{T}(\mathbf{p}^N) + \mathcal{U}(\mathbf{r}^N) + \mathcal{V}^{\mathrm{ext}}(\mathbf{r}^N), \tag{2.3}$$

where

$$\mathcal{T}(\mathbf{p}^N) = \sum_{i=1}^{N} \frac{\mathbf{p}_i^2}{2m_i}, \tag{2.4}$$

$$\mathcal{U}(\mathbf{r}^N) = \sum_{i<j} \psi(\mathbf{r}_i, \mathbf{r}_j), \tag{2.5}$$

and

$$\mathcal{V}^{\text{ext}}(\mathbf{r}^N) = \sum_i V^{\text{ext}}(\mathbf{r}_i) \tag{2.6}$$

with mass m_i for particle i and $\psi(\mathbf{r}_i, \mathbf{r}_j)$ the particle–particle potential and V^{ext} the external potential. While describing a system with a few particles by the Hamiltonian is possible, it is impractical for a classical system with $N \simeq 10^{23}$. It is necessary and sufficient to introduce macroscopic variables to describe the system. In thermodynamics, the common variables are the entropy S, temperature T, pressure P, volume V, number of particles N, and chemical potential μ. The choice of macroscopic variables depends on the situation of the actual system. In the following sections, two important ensembles are introduced: *canonical* and *grand canonical*.

2.1 Canonical ensemble

The canonical ensemble (c) considers a system exchanging heat with the environment (e.g., a heat reservoir) at constant temperature T, particle number N and external potential V^{ext}. The phase space probability distribution f_c is given by the Boltzmann factor of its Hamiltonian:

$$f_c = \frac{\exp(-\beta\mathcal{H})}{Z(V^{\text{ext}}; N, T)}, \tag{2.7}$$

where $Z(V^{\text{ext}}; N, T)$ is a normalization constant to ensure $\text{tr}_{\text{cl}} f_c = 1$, which reads

$$\begin{aligned} Z(V^{\text{ext}}; N, T) &= \text{tr}_{\text{cl}} \exp(-\beta\mathcal{H}) \\ &= \frac{1}{h^{DN} N!} \int d\mathbf{r}_1 ... \int d\mathbf{r}_N \int d\mathbf{p}_1 ... \int d\mathbf{p}_N \exp(-\beta\mathcal{H}) \\ &= \frac{1}{\lambda^{DN} N!} \int d\mathbf{r}_1 ... \int d\mathbf{r}_N \exp\left[-\beta\left(\mathcal{U}\left(\mathbf{r}^N\right) + \mathcal{V}^{\text{ext}}\left(\mathbf{r}^N\right)\right)\right], \end{aligned} \tag{2.8}$$

and

$$\text{tr}_{\text{cl}} = \frac{1}{h^{DN} N!} \int d\mathbf{r}_1 ... \int d\mathbf{r}_N \int d\mathbf{p}_1 ... \int d\mathbf{p}_N, \tag{2.9}$$

where $\lambda = \frac{h}{\sqrt{2\pi m k_{\text{B}} T}}$ is the thermal wavelength, h is the Planck constant and the kinetic degrees of freedoms have been integrated out in the last line of

Eq. (2.8). To connect Eq. (2.8) and the free energy $\mathcal{F}$, we rewrite Eq. (2.7) as

$$\begin{aligned} -k_{\mathrm{B}}T\ln Z &= -k_{\mathrm{B}}T\ln\left(\frac{\exp(-\beta\mathcal{H})}{f_c}\right) \\ &= \mathcal{H}+k_{\mathrm{B}}T\ln\left(f_c\right), \end{aligned} \tag{2.10}$$

and then take thermal average $\langle\rangle$ on both sides, such as

$$\begin{aligned} -k_{\mathrm{B}}T\ln Z &= \mathrm{tr}_{\mathrm{cl}} f_c\left(\mathcal{H}+k_{\mathrm{B}}T\ln\left(f_c\right)\right) \\ &= \langle\mathcal{H}\rangle - TS \\ &= \mathcal{F} \end{aligned} \tag{2.11}$$

where S is defined in Eq. (2.2), $\langle\mathcal{H}\rangle$ is the internal energy with fluctuations proportional to $\frac{1}{\sqrt{N}}$ and Z is a constant so $\langle\rangle$ has no effect on it. This is the famous relation between macroscopic Helmholtz free energy and the partition function Z.

2.2 Grand canonical ensemble

The grand canonical ensemble (gc) considers a system that exchanges heat and particles with the environment, so the system is at constant temperature T, chemical potential μ and external potential V^{ext}. The phase space probability distribution f_{gc} for finding N particles in a particular microstate Γ is:

$$f_{gc}=\frac{\exp\left(\beta\left(N\mu-\mathcal{H}\right)\right)}{\Xi(V^{\mathrm{ext}};\mu,T)}, \tag{2.12}$$

where Ξ is the grand canonical partition sum , which reads

$$\begin{aligned} \Xi(V^{\mathrm{ext}};\mu,T) &= \mathrm{tr}_{\mathrm{gc,cl}}\exp\left(\beta\left(N\mu-\mathcal{H}\right)\right) \\ &= \sum_{N=0}^{\infty}\frac{\exp\left(\beta\mu N\right)}{\lambda^{DN}N!}\int d\mathbf{r}_1...\int d\mathbf{r}_N\exp\left[-\beta\left(\mathcal{U}\left(\mathbf{r}^N\right)+\mathcal{V}^{\mathrm{ext}}\left(\mathbf{r}^N\right)\right)\right], \\ &= \sum_{N=0}^{\infty}\exp\left(\beta\mu N\right)Z. \end{aligned} \tag{2.13}$$

and

$$\mathrm{tr}_{\mathrm{gc,cl}}=\sum_{N=0}^{\infty}\frac{1}{h^{DN}N!}\int d\mathbf{r}_1...\int d\mathbf{r}_N\int d\mathbf{p}_1...\int d\mathbf{p}_N, \tag{2.14}$$

Similar to Eqs. (2.10) and (2.11), the grand potential Ω and Ξ are linked by

$$\begin{aligned} -k_{\mathrm{B}}T\ln\Xi &= \mathrm{tr}_{\mathrm{gc,cl}} f_c\left(\mathcal{H}-\mu N+k_{\mathrm{B}}T\ln\left(f_c\right)\right) \\ &= \left\langle\mathcal{H}\right\rangle-\mu\left\langle N\right\rangle-TS \\ &= \mathcal{F}-\mu\left\langle N\right\rangle \\ &= \Omega. \end{aligned} \tag{2.15}$$

Note that the fluctuations of $\langle N\rangle$ vanishes as $\frac{1}{\sqrt{N}}$, so the difference between N and $\langle N\rangle$ is usually negligible in macroscopic systems.

2.3 Ideal gas and density distribution functions

Here we consider the one–body density distribution (density profile) $\rho(\mathbf{r})$ in the grand canonical ensemble. The quantity $\rho(\mathbf{r})d\mathbf{r}$ is the probability to find a particle within $d\mathbf{r}$ at $\mathbf{r}$. $\langle N\rangle$ naturally satisfies

$$\left\langle N\right\rangle=\int\rho(\mathbf{r})d\mathbf{r}. \tag{2.16}$$

In the grand canonical ensemble, $\rho(\mathbf{r})$ is defined as

$$\rho(\mathbf{r})=\left\langle\sum_{i=0}^{N}\delta(\mathbf{r}-\mathbf{r}_i)\right\rangle. \tag{2.17}$$

For the non-interacting ideal gas, $\rho_{\mathrm{id}}(\mathbf{r})$ can be calculated explicitly from Eqs. (2.12), (2.13) and (2.17):

$$\begin{aligned} \rho_{\mathrm{id}}(\mathbf{r}) &= \frac{\sum_{N=1}^{\infty}\frac{\exp(\beta\mu N)}{\lambda^{DN}N!}N\exp\left(-\beta V^{\mathrm{ext}}\left(\mathbf{r}\right)\right)\left(\int d\mathbf{r}\,\exp\left(-\beta V^{\mathrm{ext}}\left(\mathbf{r}\right)\right)\right)^{N-1}}{\sum_{N=0}^{\infty}\frac{\exp(\beta\mu)}{\lambda^{DN}N!}\left(\int d\mathbf{r}\,\exp\left(-\beta V^{\mathrm{ext}}\left(\mathbf{r}\right)\right)\right)^{N}} \\ &= \frac{\exp\left(\beta\left(\mu-V^{\mathrm{ext}}\left(\mathbf{r}\right)\right)\right)}{\lambda^{D}}\frac{\sum_{N=1}^{\infty}\frac{\exp(\beta\mu(N-1))}{\lambda^{D(N-1)}(N-1)!}\left(\int d\mathbf{r}\,\exp\left(-\beta V^{\mathrm{ext}}\left(\mathbf{r}\right)\right)\right)^{N-1}}{\sum_{N=0}^{\infty}\frac{\exp(\beta\mu N)}{\lambda^{DN}N!}\left(\int d\mathbf{r}\,\exp\left(-\beta V^{\mathrm{ext}}\left(\mathbf{r}\right)\right)\right)^{N}} \\ &= \frac{\exp\left(\beta(\mu-V^{\mathrm{ext}}(\mathbf{r}))\right)}{\lambda^{D}}. \end{aligned} \tag{2.18}$$

Furthermore, Eq. (2.15) for the ideal gas gives

$$\begin{aligned}
\Xi^{\mathrm{id}}(V^{\mathrm{ext}};\mu,T) &= \sum_{N=0}^{\infty}\frac{\exp(\beta\mu N)}{\lambda^{DN}N!}\int d\mathbf{r}_1 ... \int d\mathbf{r}_N \exp\left(-\beta\mathcal{V}^{\mathrm{ext}}\left(\mathbf{r}^N\right)\right) \\
&= \sum_{N=0}^{\infty}\frac{\exp(\beta\mu N)}{\lambda^{DN}N!}\left(\int \exp\left(-\beta V^{\mathrm{ext}}(\mathbf{r})\right)\right)^N \\
&= \sum_{N=0}^{\infty}\frac{1}{N!}\left(\frac{\exp(\beta\mu)}{\lambda^{D}}\int \exp\left(-\beta V^{\mathrm{ext}}(\mathbf{r})\right)\right)^N \\
&= \exp\left(\frac{\exp(\beta\mu)}{\lambda^{D}}\int \exp\left(-\beta V^{\mathrm{ext}}(\mathbf{r})\right)\right). \qquad (2.19)
\end{aligned}$$

Thus we obtain

$$\Omega^{\mathrm{id}} = -k_{\mathrm{B}}T\ln\Xi^{\mathrm{id}} = -k_{\mathrm{B}}T\frac{\exp(\beta\mu)}{\lambda^{D}}\int \exp\left(-\beta V^{\mathrm{ext}}(\mathbf{r})\right). \qquad (2.20)$$

By comparing Ω^{id} and ρ_{id}, we have

$$\beta\Omega^{\mathrm{id}} = -k_{\mathrm{B}}T\int d\mathbf{r}\rho_{\mathrm{id}}(\mathbf{r}). \qquad (2.21)$$

Finally, the ideal gas free energy in terms of ρ_{id} is:

$$\begin{aligned}
\mathcal{F}^{\mathrm{id}} &= \Omega^{\mathrm{id}} + \mu N \\
&= \int d\mathbf{r}\,(\mu - k_{\mathrm{B}}T)\rho_{\mathrm{id}}(\mathbf{r}) \\
&= k_{\mathrm{B}}T\int d\mathbf{r}\,\rho_{\mathrm{id}}(\mathbf{r})\left(\ln\left(\lambda^{D}\rho_{\mathrm{id}}(\mathbf{r})\right)-1\right) + \int d\mathbf{r}\,V^{\mathrm{ext}}(\mathbf{r})\rho_{\mathrm{id}}(\mathbf{r}), \qquad (2.22)
\end{aligned}$$

with $\mu = k_{\mathrm{B}}T\ln(\lambda^{D}\rho_{\mathrm{id}}) + V^{\mathrm{ext}}$ from Eq. (2.18). The term $\int d\mathbf{r}\,V^{\mathrm{ext}}(\mathbf{r})\rho_{\mathrm{id}}(\mathbf{r})$ is usually absorbed into the external free energy $\mathcal{F}^{\mathrm{ext}}$, and $\rho_{\mathrm{id}}(\mathbf{r})\left(\ln\left(\lambda^{D}\rho_{\mathrm{id}}(\mathbf{r})\right)-1\right)$ is usually referred to the 'intrinsic' free energy density for the ideal gas.

2.4 Classical density functional theory

In Sec. 2.3, Eq. (2.22), the ideal gas free energy is a functional of the density distribution, i.e., $\mathcal{F}^{\mathrm{id}}[\rho_{\mathrm{id}}(\mathbf{r})]$. This property also holds for other systems and is the starting point for density functional theory (DFT). The key strength of DFT is that it accounts for the structure and thermodynamics of an inhomogeneous fluid, such as a fluid subject to an external potential or crystal-fluid

interfaces. Historically, DFT was invented by Hohenberg and Kohn in 1964 for electron gas systems at zero temperature [24], where the internal energy functional was found to depend only on the density of the electron gas. In 1965, Mermin generalized the theory to finite temperatures and proved that there is a unique functional $\Omega[\rho(\mathbf{r})]$ which depends only on the one–body density [25]. In 1979, Evans outlined a reformulation for classical systems and built the theoretical framework for (classical) DFT [26]. Below we follow his arguments.

We consider the intrinsic free energy $\mathcal{F}$ as a functional of the grand canonical probability distribution f_{gc} such that

$$\begin{aligned}\mathcal{F}[f_{gc}] &= \mathrm{tr}_{\mathrm{cl}} f_{gc}[\mathcal{T}(\mathbf{p}^N) + \mathcal{U}(\mathbf{r}^N) + k_{\mathrm{B}}T\ln(f_{gc})] \\ &= \mathrm{tr}_{\mathrm{cl}} f_{gc}[\mathcal{T}(\mathbf{p}^N) + k_{\mathrm{B}}T\ln(f_{gc})] + \mathrm{tr}_{\mathrm{cl}} f_{gc}[\mathcal{U}(\mathbf{r}^N)] \\ &= \mathcal{F}^{\mathrm{id}}[f_{gc}] + \mathcal{F}^{\mathrm{ex}}[f_{gc}], \end{aligned} \tag{2.23}$$

where $\mathcal{F}$ is split into an ideal gas term $\mathcal{F}^{\mathrm{id}}$ and an excess (over ideal gas) term $\mathcal{F}^{\mathrm{ex}}$. The key idea of DFT is that there exists a one–to–one mapping between the probability distribution f_{gc} and $\rho(\mathbf{r})$; thus $\mathcal{F}$ is also a unique functional of $\rho(\mathbf{r})$. Using this idea, we can rewrite Eq. (2.15) in terms of $\rho(\mathbf{r})$:

$$\Omega[\rho] = \mathcal{F}[\rho] - \int d\mathbf{r}\, \rho(\mathbf{r})(\mu - V^{\mathrm{ext}}(\mathbf{r})). \tag{2.24}$$

The equilibrium density $\rho^{\mathrm{eq}}(\mathbf{r})$ minimizes this grand potential functional $\Omega[\rho]$ with $\Omega_0 = \Omega[\rho^{\mathrm{eq}}] = \Omega[f_{gc}]$ being the equilibrium grand free energy of the system. To prove that, we consider a probability distribution f which is not the equilibrium one, $f \neq f_{gc}$:

$$\begin{aligned}\Omega[f \neq f_{gc}] &= \mathrm{tr}_{\mathrm{cl}} f(\mathcal{H} - \mu N + k_{\mathrm{B}}T\ln f) \\ &= \mathrm{tr}_{\mathrm{cl}} f(-k_{\mathrm{B}}T\ln f_{gc} + \Omega[f_{gc}] + k_{\mathrm{B}}T\ln f) \quad \text{(see Eq. (2.12))} \\ &= \Omega[f_{gc}] + k_{\mathrm{B}}T\mathrm{tr}_{\mathrm{cl}} f_{gc}\frac{f}{f_{gc}}\ln\frac{f}{f_{gc}} \\ &= \Omega[f_{gc}] + k_{\mathrm{B}}T\left\langle x\ln x\right\rangle \quad \text{with} \quad x = \frac{f}{f_{gc}} \\ &> \Omega[f_{gc}] + k_{\mathrm{B}}T\left\langle x-1\right\rangle \quad \text{since } x\ln x > x-1 \text{ for } x>0 \\ &> \Omega[f_{gc}] \quad \text{since } \langle x\rangle = \mathrm{tr}_{\mathrm{cl}} f = 1. \end{aligned} \tag{2.25}$$

Therefore, $\Omega[f_{gc}]$ is minimal and this implies that

$$\left.\frac{\delta\Omega[\rho]}{\delta\rho}\right|_{\rho=\rho^{\mathrm{eq}}} = 0. \tag{2.26}$$

By inserting Eq. (2.24) into Eq. (2.26), and decomposing $\mathcal{F}$ into the ideal gas part $\mathcal{F}^{\mathrm{id}}$ (Eq. (2.22)) and the excess free energy $\mathcal{F}^{\mathrm{ex}}$, we obtain the important result:

$$\lambda^D \rho^{\mathrm{eq}} = \exp\left(\beta\mu - \frac{\beta\delta\mathcal{F}^{\mathrm{ex}}}{\delta\rho}\bigg|_{\rho=\rho^{\mathrm{eq}}} - \beta V^{\mathrm{ext}}\right). \tag{2.27}$$

The remaining crucial problem is how to obtain or to approximate $\mathcal{F}^{\mathrm{ex}}$? In Chapter 3, starting from the low density limit, we introduce the Ramakrishnan-Yussouff approximation, the mean–field approximation and the fundamental measure theory. Further, in Chapter 6, a novel machine–learning method is introduced. The new machine–learning architecture, an adoption of the equation learner of Ref. [1], is capable of generating a functional by using density distributions from simulations/experiments.

Chapter 3

Approximating the excess free energy

3.1 Density expansion and direct correlation function

The excess free energy $\mathcal{F}^{\rm ex}$ is a generating functional for a hierarchy of direct correlation functions (dcf):

$$C^{(n)}(\mathbf{r}_1, \mathbf{r}_2, ..., \mathbf{r}_n) = -\beta \frac{\delta^n \mathcal{F}^{\rm ex}[\rho]}{\delta\rho(\mathbf{r}_1)\,\delta\rho(\mathbf{r}_2)...\delta\rho(\mathbf{r}_n)}. \tag{3.1}$$

Usually, the first–order dcf

$$C^{(1)}(\mathbf{r}_1) = -\beta \frac{\delta \mathcal{F}^{\rm ex}[\rho]}{\delta\rho(\mathbf{r}_1)}, \tag{3.2}$$

as already used in Eq. (2.27), and the second–order dcf

$$C^{(2)}(\mathbf{r}_1, \mathbf{r}_2) = \frac{\delta C^{(1)}(\mathbf{r}_1)}{\delta\rho(\mathbf{r}_2)} = -\beta \frac{\delta^2 \mathcal{F}^{\rm ex}[\rho]}{\delta\rho(\mathbf{r}_1)\,\delta\rho(\mathbf{r}_2)} \tag{3.3}$$

are more useful than the other higher order dcf, and thus we refer to $C^{(2)}$ as 'the dcf' for short. The connection between the direct correlation function and the Ornstein–Zernike relation is introduced in the next section. Expanding $\mathcal{F}^{\rm ex}$ around a homogeneous reference state with $\rho(\mathbf{r}) = \rho_0$ gives

$$\begin{aligned} \mathcal{F}^{\rm ex}[\rho] &= \mathcal{F}^{\rm ex}[\rho_0] + \int d\mathbf{r}_1 \left.\frac{\delta \mathcal{F}^{\rm ex}[\rho]}{\delta\rho(\mathbf{r})}\right|_{\rho=\rho_0} \Delta\rho(\mathbf{r}_1) \\ &+ \frac{1}{2}\int\int d\mathbf{r}_1 d\mathbf{r}_2 \left.\frac{\delta^2 \mathcal{F}^{\rm ex}[\rho]}{\delta\rho(\mathbf{r}_1)\,\delta\rho(\mathbf{r}_2)}\right|_{\rho=\rho_0} \Delta\rho(\mathbf{r}_1)\Delta\rho(\mathbf{r}_2) + ... \end{aligned} \tag{3.4}$$

with $\Delta\rho(\mathbf{r}) = \rho(\mathbf{r}) - \rho_0$. Further, since the reference state is homogeneous, $-\frac{1}{\beta}C^{(1)}(\mathbf{r}) = \frac{\delta\mathcal{F}^{\text{ex}}[\rho]}{\delta\rho(\mathbf{r})}\Big|_{\rho=\rho_0}$ is a constant and thus

$$\begin{aligned}\mathcal{F}^{\text{ex}}[\rho] \simeq & \mathcal{F}^{\text{ex}}[\rho_0] - \frac{1}{\beta}C^{(1)}\int d\mathbf{r}\,\Delta\rho(\mathbf{r}) \\ & - \frac{1}{2\beta}\int\int d\mathbf{r}_1 d\mathbf{r}_2\, C^{(2)}(|\mathbf{r}_1 - \mathbf{r}_2|;\rho_0)\Delta\rho(\mathbf{r}_1)\Delta\rho(\mathbf{r}_2). \end{aligned} \tag{3.5}$$

Eq. (3.5) is known as the Ramakrishnan-Yussouff approximation [27] and $C^{(2)}(|\mathbf{r}_1 - \mathbf{r}_2|;\rho_0)$ could be determined through the pair correlation function via the Ornstein–Zernike relation, where the pair correlation function can be determined in simulations or experiments (see the next section or Ref. [23] for details). Furthermore, it can be shown that $\frac{-1}{\beta}C^{(2)}$ behaves asymptotically as the pair potential when $r \to \infty$ [23], if the potential has a long–ranged part. Therefore, by further approximating $C^{(2)}(|\mathbf{r}_1 - \mathbf{r}_2|;\rho_0)$ with the effective pair potential $\psi(|\mathbf{r}_1 - \mathbf{r}_2|)$, Eq. (3.5) gives

$$\mathcal{F}^{\text{ex}}[\rho] \simeq \frac{1}{2}\int\int d\mathbf{r}_1 d\mathbf{r}_2\, \psi(|\mathbf{r}_1 - \mathbf{r}_2|)\rho(\mathbf{r}_1)\rho(\mathbf{r}_2), \tag{3.6}$$

which is the well–known mean–field or random–phase approximation. While Eqs. (3.5) and (3.6) are applicable for low densities and weak interactions, the approximation fails in many interesting cases. To improve that, one can split ψ into a short–ranged part and a tail part: $\psi = \psi_{\text{sr}} + \psi_{\text{tail}}$. The excess free energy related to ψ_{tail} is approximated by Eq. (3.6) and the excess free energy related to ψ_{sr} is a functional $\mathcal{F}^{\text{ex}}_{\text{ref}}[\rho]$ of a new reference system, which requires further investigations.

Since the reference part comes from the short–ranged interaction, in the most case it is a harsh repulsive interaction. The simplest approximation for such interaction is hard–sphere (HS) interaction, where overlap is forbidden, i.e. for HS,

$$\psi_{\text{HR}}(\mathbf{r}) = \begin{cases} \infty & \text{if} \quad |\mathbf{r}| < \sigma \\ 0 & \text{otherwise} \end{cases}$$

with σ the (effective) particle diameter. In Sec 3.3, the most accurate functional for hard spheres, fundamental measure theory (FMT), is briefly introduced.

3.2 Ornstein–Zernike relation

The Ornstein–Zernike (OZ) relation basically describes the relation between the pair correlation function and the dcf. To see this, we first define the

density–density correlation function

$$\begin{aligned} H^{(2)}(\mathbf{r}_1,\mathbf{r}_2) &= \Big\langle [\rho(\mathbf{r}_1)-\langle\rho(\mathbf{r}_1)\rangle][\rho(\mathbf{r}_2)-\langle\rho(\mathbf{r}_2)\rangle]\Big\rangle \\ &= \rho^{(2)}(\mathbf{r}_1,\mathbf{r}_2)+\rho(\mathbf{r}_1)\,\delta(\mathbf{r}_1-\mathbf{r}_2)-\rho(\mathbf{r}_1)\rho(\mathbf{r}_2) \\ &= \rho(\mathbf{r}_1)\rho(\mathbf{r}_2)h^{(2)}(\mathbf{r}_1,\mathbf{r}_2)+\rho(\mathbf{r}_1)\,\delta(\mathbf{r}_1-\mathbf{r}_2)\,, \end{aligned} \tag{3.7}$$

where $\rho^{(2)}(\mathbf{r}_1,\mathbf{r}_2)=\Big\langle\sum_{ij,i\neq j}\delta(\mathbf{r}_i-\mathbf{r}_1)\,\delta(\mathbf{r}_j-\mathbf{r}_2)\Big\rangle$ and $h^{(2)}$ is the total correlation function (the pair correlation $g^{(2)}=h^{(2)}+1$). One can prove [23] that

$$-\beta H^{(2)}(\mathbf{r}_1,\mathbf{r}_2)=\frac{\delta^2\Omega}{\delta\phi(\mathbf{r}_1)\,\delta\phi(\mathbf{r}_2)} \tag{3.8}$$

where $\phi(\mathbf{r})=\mu-V^{\text{ext}}(\mathbf{r})$. From Eq. (3.2), we have

$$\begin{aligned} &\beta\phi(\mathbf{r})=\beta\frac{\delta\mathcal{F}[\rho]}{\delta\rho(\mathbf{r})}=\ln\left(\lambda^D\rho(\mathbf{r})\right)-C^{(1)}(\mathbf{r}),\text{ and} \\ &\beta\frac{\delta\phi(\mathbf{r}_1)}{\delta\rho(\mathbf{r}_2)}=\frac{1}{\rho(\mathbf{r}_1)}\delta(\mathbf{r}_1-\mathbf{r}_2)-C^{(2)}(\mathbf{r}_1,\mathbf{r}_2). \end{aligned} \tag{3.9}$$

Combining Eqs. (2.24) and (3.8) we obtain an algebraic

$$\rho(\mathbf{r})=-\frac{\delta\Omega}{\delta\phi(\mathbf{r})},\text{ and }\quad \beta H^{(2)}(\mathbf{r}_1,\mathbf{r}_2)=\frac{\delta\rho(\mathbf{r}_1)}{\delta\phi(\mathbf{r}_2)}. \tag{3.10}$$

Through the relation:

$$\delta(\mathbf{r}_1-\mathbf{r}_2)=\frac{\delta\rho(\mathbf{r}_1)}{\delta\rho(\mathbf{r}_2)}=\int d\mathbf{r}_3\frac{\delta\rho(\mathbf{r}_1)}{\delta\phi(\mathbf{r}_3)}\frac{\delta\phi(\mathbf{r}_3)}{\delta\rho(\mathbf{r}_2)} \tag{3.11}$$

and substituting $\frac{\delta\rho}{\delta\phi}$ by Eq. (3.7) and $\frac{\delta\phi}{\delta\rho}$ by Eq. (3.10), we obtain the OZ relation:

$$\begin{aligned} h^{(2)}(\mathbf{r}_1,\mathbf{r}_2) &= C^{(2)}(\mathbf{r}_1,\mathbf{r}_2)+\int d\mathbf{r}_3 C^{(2)}(\mathbf{r}_1,\mathbf{r}_3)\rho(\mathbf{r}_3)h^{(2)}(\mathbf{r}_3,\mathbf{r}_2) \\ &= C^{(2)}(\mathbf{r}_1,\mathbf{r}_2)+\int d\mathbf{r}_3 C^{(2)}(\mathbf{r}_1,\mathbf{r}_3)\rho(\mathbf{r}_3)C^{(2)}(\mathbf{r}_3,\mathbf{r}_2) \\ &\quad +\int\int d\mathbf{r}_3 d\mathbf{r}_4 C^{(2)}(\mathbf{r}_1,\mathbf{r}_3)\rho(\mathbf{r}_3)C^{(2)}(\mathbf{r}_3,\mathbf{r}_4)\rho(\mathbf{r}_4)C^{(2)}(\mathbf{r}_4,\mathbf{r}_2)+... \end{aligned} \tag{3.12}$$

Eq (3.12) has a clear physical interpretation: the total correlation $h^{(2)}$ between particles 1 and 2 is due to the direct correlation $C^{(2)}(\mathbf{r}_1,\mathbf{r}_2)$ and the

'indirect' correlation propagated via intermediate particles. For a homogeneous fluid, Eq. (3.12) can be reduced to

$$h^{(2)}(r) = C^{(2)}(r) + \rho \int d\mathbf{r}' C^{(2)}(|\mathbf{r} - \mathbf{r}'|) h^{(2)}(|\mathbf{r}'|) \tag{3.13}$$

where $r = |\mathbf{r}|$. On taking the Fourier transform on both sides, we obtain an algebraic relation between $h^{(2)}$ and $C^{(2)}$:

$$\widetilde{h^{(2)}}(k) = \widetilde{C^{(2)}}(k) + \rho \widetilde{C^{(2)}}(k) \widetilde{h^{(2)}}(k) \Rightarrow \widetilde{h^{(2)}}(k) = \frac{\widetilde{C^{(2)}}(k)}{1 - \rho \widetilde{C^{(2)}}(k)}. \tag{3.14}$$

In experiments or simulations, one could directly determine $h^{(2)}$ or $\widetilde{h^{(2)}}$ [23] and thus calculate $C^{(2)}$ for the homogeneous fluid and insert it into the Ramakrishnan-Yussouff approximation (Eq. (3.5)).

3.3 Fundamental measure theory

Fundamental measure theory is a special DFT treatment for hard–body fluids, using weighted densities. In contrast to approximations by expanding $C^{(2)}$, the free energy density is taken to be a function of several different weighted densities, defined by geometrical characteristics of the particles.

It can be shown [23] that $C^{(2)}(r)$ in a low-density expansion is given by

$$C^{(2)}(r) = f(r) + \rho f(r) \int d\mathbf{r}' f(|\mathbf{r} - \mathbf{r}'|) f(|\mathbf{r}'|) + ..., \tag{3.15}$$

where $f(r) = e^{-\beta\psi(r)} - 1$ is known as the Mayer–f function with ψ the particle–particle interaction. Thus the excess free energy ($\mathcal{F}^{\text{ex}}$) in the low density limit is:

$$\beta \mathcal{F}^{\text{ex}} \simeq -\frac{1}{2} \int \int d\,\mathbf{r}\, d\,\mathbf{r}' \rho(\mathbf{r}) \rho(\mathbf{r}') f(\mathbf{r} - \mathbf{r}'). \tag{3.16}$$

3.3.1 Three–dimensional hard spheres

For hard spheres, $f(|\mathbf{r} - \mathbf{r}'|) = -\Theta(2R - |\mathbf{r} - \mathbf{r}'|)$ with Θ the Heaviside step function and R the (effective) radius. By the ingenious insight from Rosenfeld [5], f_{ij} can be deconvoluted into a set of weight functions ω [1], such as

$$-f(r) = 2\left(\omega_3 \otimes \omega_0 + \omega_2 \otimes \omega_1 + \boldsymbol{\omega}_1 \otimes \boldsymbol{\omega}_2\right), \tag{3.17}$$

[1] For the sake of simplicity, we consider only the one–component case.

where

$$\begin{aligned}
\omega_3(\mathbf{r}) &= \Theta(R - |\mathbf{r}|), \\
\omega_2(\mathbf{r}) &= \delta(R - |\mathbf{r}|), \\
\omega_1(\mathbf{r}) &= \frac{\omega_2(\mathbf{r})}{4\pi R}, \\
\omega_0(\mathbf{r}) &= \frac{\omega_2(\mathbf{r})}{4\pi R^2}, \\
\boldsymbol{\omega}_2(\mathbf{r}) &= \frac{\mathbf{r}}{|\mathbf{r}|}\delta(R - |\mathbf{r}|), \text{ and} \\
\boldsymbol{\omega}_1(\mathbf{r}) &= \frac{\boldsymbol{\omega}_2(\mathbf{r})}{4\pi R},
\end{aligned} \tag{3.18}$$

with δ the Dirac delta function. Integrating over the scalar weight functions gives the 'fundamental geometric measures" of a sphere,

$$\begin{aligned}
\int d\mathbf{r}\, \omega_3(\mathbf{r}) &= \frac{3}{4}\pi R^3 && \text{Volumn} \\
\int d\mathbf{r}\, \omega_2(\mathbf{r}) &= 4\pi R^2 && \text{Surface} \\
\int d\mathbf{r}\, \omega_1(\mathbf{r}) &= R && \text{Mean radius of curvature} \\
\int d\mathbf{r}\, \omega_0(\mathbf{r}) &= 1 && \text{Euler characteristic}
\end{aligned} \tag{3.19}$$

and $\boldsymbol{\omega}_2 = \nabla\omega_3$, hence the name "fundamental measure theory".

Eq. (3.16) in the low density limit becomes

$$\beta\mathcal{F}^{\text{ex}}[\rho] = \int d\mathbf{r}\, \Phi([n_\alpha]) \simeq \int d\mathbf{r}\ (n_1\, n_2 - \mathbf{n}_1 \cdot \mathbf{n}_2 + n_0\, n_3) \tag{3.20}$$

with the weighted densities $n_\alpha(\mathbf{r}) = \rho \otimes \omega_\alpha = \int d\mathbf{r}'\, \rho(\mathbf{r}')\omega_\alpha(\mathbf{r} - \mathbf{r}')$. In the homogeneous limit, $n_0 = \rho$, $n_1 = R\rho$, $n_2 = 4\pi R^2\rho$, $n_3 = \frac{4}{3}\pi R^3\rho$ and $\mathbf{n}_1 = \mathbf{n}_2 = 0$.

To approximate the excess free energy density Φ, one possibility, in the spirit of Eq. (3.20) is to write Φ as a sum of product of weighted densities. One may use a dimensional argument: since $\beta\mathcal{F}^{\text{ex}}$ is dimensionless, Φ must have the dimension of 1/volume, $[\Phi] = \frac{1}{L^3}$. Thus Φ can only be a sum of terms consisting of factors n_0, $n_1 n_2$, $\mathbf{n}_1 \cdot \mathbf{n}_2$, n_2^3 and $n_2(\mathbf{n}_2 \cdot \mathbf{n}_2)$, and each term can be multiplied with a scalar function $f_i(n_3)$. Note $[n_l] = \frac{1}{L^{3-l}}$. Thus Rosenfeld proposed the ansatz:

$$\Phi(n_\alpha) = f_1(n_3)n_0 + f_2(n_3)n_1\, n_2 + f_3(n_3)\mathbf{n}_1 \cdot \mathbf{n}_2 + f_4(n_3)n_2^3 + f_5(n_3)n_2(\mathbf{n}_2 \cdot \mathbf{n}_2). \tag{3.21}$$

Using the definition of the chemical potential $\mu^{\rm ex} = \left.\frac{\delta \mathcal{F}^{\rm ex}}{\delta \rho}\right|_{\rho=\text{const.}}$, we obtain

$$\beta\mu^{\rm ex} = \frac{\partial \Phi}{\partial \rho} = \sum_\alpha \frac{\partial \Phi}{\partial n_\alpha}\frac{\partial n_\alpha}{\partial \rho}. \tag{3.22}$$

We adopt the view of scaled particle (SP) theory, and consider a single solute particle of radius R_ν in a uniform hard–sphere fluid with radius R. It can be shown that [23]

$$\lim_{R_\nu \to \infty} \mu_\nu^{\rm ex} = P_{\rm sp} V_\nu \tag{3.23}$$

with $P_{\rm sp}$ the bulk pressure and V_ν the volume of the solute particle, which leads to

$$P_{\rm sp} = \frac{\partial \Phi}{\partial n_3}. \tag{3.24}$$

On the other hand, we have the thermodynamic (TD) relation,

$$\beta P_{\rm TD} = \frac{-\beta \Omega_{\rm bulk}}{V} = -\Phi - \beta \mathfrak{f}^{\rm id} + \beta\mu\rho \tag{3.25}$$

with $\mathfrak{f}^{\rm id}$ ideal gas free energy density (Eq (2.22)). Thus we obtain

$$\beta P_{\rm TD} = n_0 - \Phi + \sum_\alpha \frac{\partial \Phi}{\partial n_\alpha} n_\alpha. \tag{3.26}$$

By equating $P_{\rm TD}$ and $P_{\rm sp}$ and substituting Eq. (3.21), we obtain

$$\begin{aligned}
f_1' &= 1 + n_3 f_1' \Rightarrow f_1 = -\ln(1-n_3) + C_1, \\
f_2' &= f_2 + n_3 f_2' \Rightarrow f_2 = \frac{C_2}{1-n_3}, \\
f_3 &= \frac{C_3}{1-n_3}, \\
f_4 &= \frac{C_4}{(1-n_3)^2}, \text{ and} \\
f_5 &= \frac{C_5}{(1-n_3)^2}.
\end{aligned} \tag{3.27}$$

In the low density limit, $\Phi = n_1 n_2 - \mathbf{n}_1 \cdot \mathbf{n}_2 + n_0 n_3$ (Eq. (3.20)) and it leads to $C_1 = 0, C_2 = 1, C_3 = -1$. Furthermore, considering the dcf for the one–component HS fluid, Eq (3.3) gives

$$-C^{(2)}(\mathbf{r}_1, \mathbf{r}_2) = \frac{\delta^2 \Phi[n]}{\delta\rho(\mathbf{r}_1)\,\delta\rho(\mathbf{r}_2)} = \sum_{\alpha,\beta} \int d\mathbf{r}\, \frac{\partial^2 \Phi}{\partial n_\alpha \partial n_\beta} w_\alpha(\mathbf{r}-\mathbf{r}_1) w_\beta(\mathbf{r}-\mathbf{r}_2). \tag{3.28}$$

In the low–density and the homogeneous limit ($\mathbf{n}_2 \to 0$),

$$\sum_{\alpha,\beta} \int d\mathbf{r}\, \frac{\partial^2 \Phi}{\partial n_\alpha \partial n_\beta} w_\alpha(\mathbf{r}-\mathbf{r}_1) w_\beta(\mathbf{r}-\mathbf{r}_2) = \sum_{\alpha,\beta} \frac{\partial^2 \Phi}{\partial n_\alpha \partial n_\beta} w_\alpha \oplus w_\beta$$
$$= \Theta(2R-r) + 6C_4 n_2 (w_2 \oplus w_2) + 2C_5 n_2 \left(\boldsymbol{\omega}_2 \oplus \boldsymbol{\omega}_2\right), \tag{3.29}$$

where $\oplus$ denotes the cross–correlation ($w_\alpha \oplus w_\beta = \int d\mathbf{r}\, w_\alpha(\mathbf{r}-\mathbf{r}_1) w_\beta(\mathbf{r}-\mathbf{r}_2)$) and

$$\begin{aligned} 6C_4 n_2 (w_2 \oplus w_2) &+ 2C_5 n_2 (\boldsymbol{\omega}_2 \oplus \boldsymbol{\omega}_2) \\ &= 2n_2 (3C_4 w_2 \oplus w_2 + C_5\, \boldsymbol{\omega}_2 \oplus \boldsymbol{\omega}_2) \\ &= 2n_2 \left(\frac{4\pi^3 \left(-C_5 r^2 - 2\left(-3C_4 - C_5\right) R^2\right)}{r} \right). \end{aligned} \tag{3.30}$$

To eliminate the divergence at $r \to 0$, we choose $C_5 = -3C_4$. To determine the remaining constant C_4, we consider the low–density limit for Φ for a homogeneous fluid,

$$\begin{aligned} \Phi &= \frac{4\pi R^3 \rho^2}{1 - \frac{4}{3}\pi R^3 \rho} + \frac{64 C_4 \pi^3 R^6 \rho^3}{\left(1 + \frac{4}{3}\pi R^3 \rho\right)^2} - \rho \ln\left[1 - \frac{4}{3}\pi R^3 \rho\right] \\ &\simeq \frac{16}{3}\pi R^3 \rho^2 + \left(\frac{56\pi^2 R^6}{9} + 64 C_4 \pi^3 R^6\right) \rho^3 + O[\rho^4], \end{aligned} \tag{3.31}$$

which gives the equation of state

$$\begin{aligned} \frac{\beta P_{\text{TD}}}{\rho} &= \frac{1}{\rho}\left(-\Phi - \beta \mathfrak{f}^{\text{id}} + \frac{\partial(\Phi + \mathfrak{f}^{\text{id}})}{\partial \rho}\rho\right) \\ &\simeq 1 + \frac{16}{3}\pi R^3 \rho + \left(\frac{112\pi^2 R^6}{9} + 128 C_4 \pi^3 R^6\right) \rho^2 + O[\rho^3]. \end{aligned} \tag{3.32}$$

We use the knowledge of the virial expansion with the exactly known first three terms,

$$\frac{\beta P}{\rho} = 1 + 4\eta + 10\eta^2 + O[\eta^3], \tag{3.33}$$

where $\eta = \frac{4}{3}\pi R^3 \rho$ is the packing fraction. Putting Eqs. (3.31) and (3.32) together, we can determine that $C_4 = \frac{1}{24\pi}$. Finally, we obtain Rosenfeld's free energy functional:

$$\Phi = -n_0 \ln(1-n_3) + \frac{n_1\, n_2 - \mathbf{n}_1 \cdot \mathbf{n}_2}{1-n_3} + \frac{n_2^3 - 3n_2(\mathbf{n}_2 \cdot \mathbf{n}_2)}{24\pi(1-n_3)^2}. \tag{3.34}$$

It is worth to note that in the homogeneous limit, Eq. (3.34) gives the Percus–Yevick–Frisch equation of state [28],

$$\frac{\beta P}{\rho} = \frac{1+\eta+\eta^2}{(1-\eta)^3}. \tag{3.35}$$

Furthermore, we consider an external potential such that the system is held between two close walls in the x–y–plane, and the local density profile is given by $\rho(\mathbf{r}) = \rho_{2\mathrm{D}}(x,y)\delta(z)$. In this way a homogeneous density profile in 2D can be treated as highly confined 3D system, and the free energy $\mathcal{F}_{3\mathrm{D}}[\rho(x,y)\delta(z)] = \mathcal{F}_{2\mathrm{D}}[\rho(x,y)]$. Such a narrowing procedure is referred as 'dimensional crossover'. By further confinement of the system along the x–axis and all three axes, the local density profile turns into $\rho(\mathbf{r}) = \rho_{1\mathrm{D}}(x)\delta(y)\delta(z)$ and $\rho(\mathbf{r}) = \rho_{0\mathrm{D}}\delta(x)\delta(y)\delta(z)$. The importance of the cavity–like 0D situation of the latter case is that the crystalline state can be interpreted as a highly confined inhomogeneous system as each particle confined by its nearest neighborhoods, and thus to capture the crystalline phase the functional must have the correct behavior in the 0D limit.

Starting from the exactly known $\mathcal{F}_{1\mathrm{D}}$ and $\mathcal{F}_{0\mathrm{D}}$, Tarazona *et al.* [6, 7] introduced the tensorial weight function:

$$\boldsymbol{\omega}_{\mathrm{T}}(\mathbf{r}) = \left(\frac{\mathbf{r}\cdot\mathbf{r}^t}{|\mathbf{r}|^2} - \frac{\mathbb{I}}{3}\right)\delta(R-|\mathbf{r}|), \tag{3.36}$$

and the tensor functional:

$$\begin{aligned}\Phi =& -n_0\ln(1-n_3) + \frac{n_1 n_2 - \mathbf{n}_1\cdot\mathbf{n}_2}{1-n_3} \\ &+ \frac{n_2^3 - 3n_2\mathbf{n}_2\cdot\mathbf{n}_2 + \frac{9}{2}(\mathbf{n}_2^t\cdot\mathbf{n}_{\mathrm{T}}\cdot\mathbf{n}_2 - \mathrm{Tr}(\mathbf{n}_{\mathrm{T}}^3))}{24\pi(1-n_3)^2},\end{aligned} \tag{3.37}$$

where $\mathbb{I}$ is the unit matrix in $\mathbb{R}^{3\times3}$, superscript t represents the transpose, and $\mathrm{Tr}(\cdot)$ denotes the trace of a matrix. The tensorial modification gives decent descriptions of the hard–sphere crystal. However, due to the underlying Percus–Yevick–Frisch equation of state, the obtained phase coexistence densities are lower than the ones from MC simulation results.

White Bear II

In 2006, Hansen–Goos and Roth [29, 8] improved the FMT by considering a modified Carnahan-Starling (CS) equation of state [30] given by

$$\beta P_{\mathrm{CS}} = \frac{n_0}{1-n_3} + \frac{n_1 n_2\left(1+\frac{n_3^2}{3}\right)}{(1-n_3)^2} + \frac{n_2^3\left(1-\frac{2n_3}{3}+\frac{n_3^2}{3}\right)}{12(1-n_3)^3\pi}. \tag{3.38}$$

In the homogeneous limit for a one–component hard–sphere fluid, Eq. (3.38) is equivalent to the original CS equation of state

$$\frac{\beta P}{\rho} = \frac{1+\eta+\eta^2-\eta^3}{(1-\eta)^3}, \tag{3.39}$$

which is more precise than the Percus–Yevick–Frisch equation of state.

Equating P_{CS} with P_{TD} and proceeding as before (see Eqs. (3.26) and (3.27)), we obtain

$$f_2 + n_3 f_2' = \frac{1+\frac{1}{3}n_3^2}{(1-n_3)^2} \tag{3.40}$$

$$2f_4 + n_3 f_4' = \frac{1-\frac{2}{3}n_3+\frac{1}{3}n_3^2}{12\pi(1-n_3)^3}, \tag{3.41}$$

which gives

$$f_2 = \frac{C_2}{n_3} + \frac{-\frac{4}{-1+n_3}+n_3+2\ln(1-n_3)}{3n_3} \tag{3.42}$$

$$f_4 = \frac{C_4}{n_3^2} - \frac{\frac{1-2n_3}{(-1+n_3)^2}+n_3+\ln(1-n_3)}{36n_3^2\pi}. \tag{3.43}$$

To eliminate the potential divergence in the low–density limit, we choose $C_2 = -\frac{4}{3}$ and $C_4 = \frac{1}{36\pi}$; thus, we obtain the White Bear II free energy functional :

$$\begin{aligned}\Phi_{\text{ex,HS}}^{\text{WBIIT}}(n_\alpha) = &- n_0\ln(1-n_3) + g_2(n_3)\frac{n_1 n_2 - \mathbf{n}_1\cdot\mathbf{n}_2}{1-n_3} \\ &+ g_3(n_3)\frac{n_2^3 - 3n_2\mathbf{n}_2\cdot\mathbf{n}_2}{24\pi(1-n_3)^2}\end{aligned} \tag{3.44}$$

with

$$\begin{aligned}g_2(n_3) &= -\frac{(-5+n_3)n_3+2(-1+n_3)\ln(1-n_3)}{3n_3} \text{ and} \\ g_3(n_3) &= -\frac{2\left(n_3(1+(-3+n_3)n_3)+(-1+n_3)^2\ln(1-n_3)\right)}{3n_3^2}.\end{aligned} \tag{3.45}$$

Furthermore, on combining the tensorial modification (Eqs. (3.37)) and White Bear II functional (Eq. (3.44)), we obtain the White Bear II tensorial functional:

$$\begin{aligned}\Phi_{\text{ex,HS}}^{\text{WBII,tensor}}(n_\alpha) = &-n_0\ln(1-n_3) + g_2(n_3)\frac{n_1 n_2 - \mathbf{n}_1\cdot\mathbf{n}_2}{1-n_3} \\ &+ g_3(n_3)\frac{n_2^3 - 3n_2\mathbf{n}_2\cdot\mathbf{n}_2 + \frac{9}{2}(\mathbf{n}_2^t\cdot\mathbf{n}_{\text{T}}\cdot\mathbf{n}_2 - \text{Tr}(\mathbf{n}_{\text{T}}^3))}{24\pi(1-n_3)^2},\end{aligned} \tag{3.46}$$

which is by far the most accurate functional for HS systems [31, 32].

3.3.2 Two–dimensional hard disks

One may expect that FMT for HS systems is capable of describing two–dimensional (2D) hard–disk (HD) systems by a slab–like confinement; however, such confinement gives $\frac{\beta P}{\rho} \sim (1-\eta)^{-5/2}$ for high packing fractions η, while the scaled particle theory gives $\frac{\beta P}{\rho} \sim (1-\eta)^{-2}$ [33]. Alternatively, one may try to construct $\mathcal{F}^{\text{ex}}$ by a deconvolution, similarly to Sec.3.3.1 for HD systems. Then a difficulty arises: the deconvolution of the Mayer function like Eq. (3.17) requires an infinite number of weight functions. Following Ref. [3], the deconvolution for HD is:

$$-f_{ij}(r) = \omega_2^i \otimes \omega_0^j + \omega_2^j \otimes \omega_0^i + \sum_{m=0}^{\infty} \frac{C_m}{2\pi} \boldsymbol{\omega}_{(m)}^i \otimes \boldsymbol{\omega}_{(m)}^j, \tag{3.47}$$

with weight functions

$$\omega_0^i(\mathbf{r}) = \frac{\delta(R_i - r)}{2\pi R_i},\ \omega_2^i(\mathbf{r}) = \Theta(R_i - r), \tag{3.48}$$

and

$$\boldsymbol{\omega}_{(m)}^i(\mathbf{r}) = \underbrace{\hat{\mathbf{r}}...\hat{\mathbf{r}}}_{m \text{ times}}\, \delta(R_i - r). \tag{3.49}$$

Using similar arguments as in Sec.3.3.1, one can obtain the excess free energy density

$$\Phi^{\text{HD}}(n_\alpha) = -n_0 \ln(1-n_2) + \sum_{m=0}^{\infty} \frac{1}{4\pi(1-n_2)} C_m\, \mathbf{n}_m \cdot \mathbf{n}_m, \tag{3.50}$$

where the first three coefficients are $C_0 = \frac{\pi}{2}$, $C_1 = -1$ and $C_2 = -\frac{\pi}{4}$. The virial expansion of the equation of state for the HD fluid reads $\frac{\beta P}{\rho} = 1 + 2\eta + O[\rho^2]$ with packing fraction $\eta = \pi R^2 \rho$. Unfortunately, the truncation up to C_2 gives $\frac{\beta P}{\rho} = 1 + (1 + C_0 + C_2/2)\eta + O[\rho^2] = 1 + (1 + \frac{3\pi}{8})\eta + O[\rho^2]$ and thus fails to deliver the correct second virial coefficient.
To cure this deficiency, Roth *et al.* [3] reconsidered $C_0..C_2$ as free parameters. The correct second virial coefficient requires $C_0 + C_2/2 = 1$ and the correct free energy in the 0D confinement for sharp density peak requires $C_0 + C_1 + C_2 = 0$ (see Sec.3.3.1). Thus the final form of the free energy functional is:

$$\Phi^{\text{HD}}(n_\alpha) = -n_0 \ln(1-n_2) + \frac{(C_0 \mathbf{n}_0^2 + C_1 \mathbf{n}_1^2 + C_2\, \text{Tr}[\mathbf{n}_2^2])}{4\pi(1-n_2)}\,, \tag{3.51}$$

with

$$C_0 = \frac{a+2}{3},\ C_1 = \frac{a-4}{3} \text{ and } C_2 = \frac{2-2a}{3}. \tag{3.52}$$

For the one–component HD system, a best fit to the Mayer f–bond gives $a = 11/4$ whereas a fit to crystal pressures obtained by simulations gives $a = 3$ [3]. For binary systems in the fluid phase, the functional delivers an excellent description of pair correlation functions when compared to experiments [12].

3.3.3 One–dimensional hard rods

The deconvolution of the Mayer f function for hard rods (HR) in one dimension (1D) reads

$$-f_{ij}(r) = \omega_1^i \otimes \omega_0^j + \omega_1^j \otimes \omega_0^i, \tag{3.53}$$

where $\omega_1(x) = \Theta(\sigma/2 - |x|)$ and $\omega_0(x) = \frac{1}{2}\delta(\sigma/2 - |x|)$. The $\mathcal{F}^{\text{ex}}$ in the low density limit is given by

$$\beta\mathcal{F}^{\text{ex}} = \int n_0 n_1 \, dx. \tag{3.54}$$

With the dimensional argument similar to 3D hard-spheres, the ansatz is $\Phi[n] = n_0 f(n_1)$. Considering the exact HR equation of state $P = \frac{\rho}{1-\rho\sigma}$ and scaled particle theory (Eq. (3.24)), one obtains $f'(n_1) = \frac{1}{1-n_1}$ and thus $f(n_1) = -\ln(1 - n_1)$. The final form of $\mathcal{F}^{\text{HR}}$ is

$$\beta\mathcal{F}^{\text{HR}} = \int \Phi[n] \, dx = \int -n_0 \ln(1 - n_1) \, dx, \tag{3.55}$$

which is equivalent to the exact HR functional derived by Percus with different means in Ref. [34].

Chapter 4

Bulk fluid and crystal phase for one–component hard disks

Here we focus on the one–component two–dimensional (2D) systems of hard disks (HD). The fluid–crystal transition in 2D systems of HD has been of fundamental interest over years. Only recently, it has been established in the one–component system by simulations [10] and experiments [11] that the transition happens via a first–order transition from the fluid to the hexatic phase and a continuous transition from the hexatic to the crystal phase. Although the crystal phase is not strictly periodic (it does not have infinitely long–ranged translational order), in simulations and experiments it has practically the appearance of a conventional, periodic crystal. Therefore, 2D hard disks have a similar status as a model system for crystallization in films and monolayers as 3D hard spheres have for crystallization in the bulk. Besides simulations, classical density functional theory (DFT) for hard particle systems has reached a maturity and accuracy owing to the development of fundamental measure theory (FMT), starting with the work of Rosenfeld [4]. For 2D hard disks, a functional has been proposed in Ref. [3] (see also Sec. 3.3.2), which gives a very accurate description of fluid structure [12], as well as values for the fluid and crystal coexistence densities which are rather close to the ones of the first–order fluid–hexatic transition [3]. In these FMT calculations, strict periodicity of the crystal phase was assumed.

4.1 Bulk phase and coexistence

4.1.1 Bulk phase

In DFT, the bulk fluid phase is characterized by a homogeneous density field and the bulk crystal phase is a fluid with spontaneous symmetry breaking, resulting in a strongly peaked density at lattice sites. To study the bulk crystal phase and coexistence, we assume periodicity and consider a rectangular unit cell with side lengths L and $\sqrt{3}L$ for a triangular lattice (see Fig.4.1). The free parameters in this free energy minimization problem are the density profiles $\rho(\mathbf{r})$ in the unit cell as well as the length L. We parametrize the latter via an effective vacancy concentration n_{vac}:

$$\int_{\text{cell}} d\mathbf{r}\, \rho(\mathbf{r}) =: 2(1 - n_{\text{vac}}) = \bar{\rho}\sqrt{3}\, L^2. \tag{4.1}$$

In the one–component case, an ideal crystal has 2 particles in the unit cell, therefore $n_{\text{vac}} > 0$ indeed corresponds to the vacancy concentration in the equilibrium crystal.

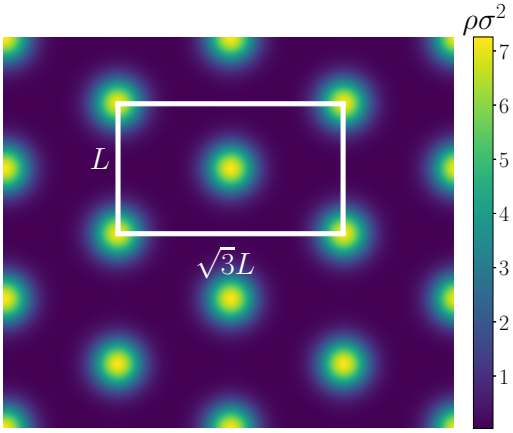

Figure 4.1: Density distribution $\rho(\mathbf{r})$ of a one–component perfect crystal ($\bar{\rho}\sigma^2 = 0.932$, $n_{\text{vac}} = 0.0122$, $a = 11/4$ and σ the hard–disk diameter). The solid white line indicates the computational box (rectangular unit cell of the triangular lattice which contains two particles)

The full minimization of free energy $\mathcal{F}$ for given average densities $\bar{\rho}$ proceeds via

$$\mathcal{F}(\bar{\rho}) = \min_{n_{\text{vac}}} \min_{\{\rho(\mathbf{r})\}} F[n_\alpha], \tag{4.2}$$

i.e. in two steps [31]. The first minimization step is achieved by an iterative solution of the Euler–Lagrange equation (for fixed $n_{\rm vac}, L$)

$$\rho = \exp\left(-\beta\frac{\delta\mathcal{F}^{\rm ex}\left[n_\alpha\right]}{\delta\rho} + \beta\mu\right) = K[\rho], \tag{4.3}$$

where

$$\beta\frac{\delta\mathcal{F}^{\rm ex}\left[n_\alpha\right]}{\delta\rho(\mathbf{r})} = \int d\mathbf{r}' \sum_\alpha \frac{\partial\Phi[n_\alpha]}{\partial n_\alpha}(\mathbf{r}')w_\alpha(\mathbf{r}'-\mathbf{r}) \tag{4.4}$$

with Φ in Eq. (3.51). The chemical potential μ is adapted in each iteration step to keep the average particle density $\bar{\rho}$ constant. Iteration is done by using a combination of Picard steps and discrete inversion in iterative subspace (DIIS) [35, 31] (see also Appendix B for more details). The Picard steps are performed according to

$$\rho^{j+1} = \xi\, K[\rho^j] + (1-\xi)\rho^j, \tag{4.5}$$

where j labels the iteration step and ξ is a Picard mixing parameter which we chose in the range from 10^{-3} to 10^{-2} for bulk crystal and also interface minimizations. The DIIS steps are performed using between 5 and 9 forward profiles. The second minimization step, the minimization with respect to $n_{\rm vac}$ (and thus L), amounts to doing the first minimization for a few values of $n_{\rm vac}$ within an interval of starting width $\sim 10^{-3}$ and subsequently determining the minimum via a quadratic fit. The procedure is iterated with smaller interval widths until we have reached 3 digits of confidence or the interval width is less than 10^{-5} (see Fig. 4.2(a)).

4.1.2 Coexistence

From Table 4.1 we see that coexisting packing fractions and the surface tension are described very well by FMT, even though in FMT the strict periodicity assumption for the crystal differs from the character of the hexatic and crystal phase in experiments/simulations. This good correspondence is in line with the quantitative description of fluid structure found in earlier works [3, 12].

Phase coexistence requires $P_{\rm cr} = P_{\rm fl}$ and $\mu_{\rm cr} = \mu_{\rm fl}$. Fully minimizing F/N with respect to $n_{\rm vac}$ delivers $P_{\rm cr}$ and $\mu_{\rm cr}$. Through $\mu_{\rm cr} = \mu_{\rm fl}$ and the fluid equation of state we can find $P_{\rm fl}$ and $\rho_{\rm fl}$ in the fluid. In general, $P_{\rm fl} \neq P_{\rm cr}$ and thus we change $\rho_{\rm cr}$ iteratively until $\beta\sigma_l^2|P_{\rm cr} - P_{\rm fl}| < 5\times10^{-6}$ (see Fig. 4.2(b)).

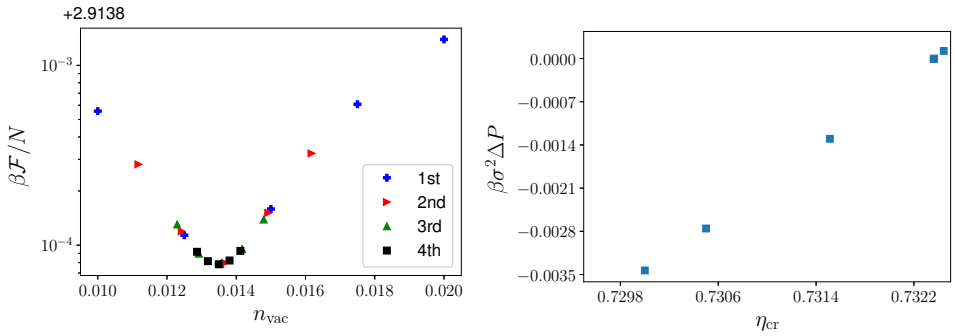

Figure 4.2: (a) Minimization with respect to $n_{\rm vac}$ with $\eta_{\rm cr} = 0.73$ and $a = 11/4$ (see Eq. 3.52). The procedure is iterated four times. (b)Finding coexistence pressure by determining $\Delta P = |P_{\rm cr} - P_{\rm fl}|$ for different $\eta_{\rm cr}$, and the $n_{\rm vac}$ of each $\eta_{\rm cr}$ is determined as in (a).

Table 4.1: Thermodynamic properties of the one–component crystal. σ is the HD diameter, P pressure, μ chemical potential, $\eta = (\pi/4)\sigma^2\rho$ packing fraction, and the subscript (co) denotes coexistence of the crystal (cr) and fluid (fl), respectively. Note that for Exp and MC, two values for $\eta_{\rm cr}$ correspond to the packing fraction of the hexatic phase at fluid-hexatic coexistence and the packing fraction at the hexatic–crystal continuous transition, respectively. The FMT coexistence values differ slightly from those in Ref. [3] which suffer from a small numerical error.

	FMT		Exp[11]*	MC[10]
	$a = 11/4$	$a = 3$		
$\beta\sigma^2 P_{\rm co}$	10.84	9.234		9.185
$\beta\mu_{\rm co}$	14.576	12.778		
$\eta_{\rm cr}$	0.732	0.7165	0.7/0.73	0.716/0.72
$\eta_{\rm fl}$	0.711	0.6913	0.68	0.700
n_{vac}	0.0122	0.0194		0.001

(* see Supplementary Material in Ref. [11])

4.2 Planar interface and surface tension

A surface tension in 2D is a line tension defined as $\frac{\Omega+PA}{L}$, where P is the pressure, A is the area of the system and L is the length of the interface. Here we are interested in the planar surface tension γ. In general, γ depends on the angle θ between the crystal and the interface normal. To determine $\gamma(\theta)$, we need to model a stress–free solid [36], but extension of a rectangular piece of solids subjected to periodic boundary conditions is non-trivial due to lattice symmetry. Here we describe how to determine the stress–free periodic boundary condition for a 2D triangular lattice.

As shown in Fig 4.3a, there are two primitive vectors $\vec{a} = (a, 0)$ and $\vec{b} = (0, \sqrt{3}a)$ in a unit cell, where a is the lattice constant.

These vectors in a rotated unit cell with rotation angle θ are

$$\vec{a'} = a\cos(\theta)\hat{x} + a\sin(\theta)\hat{y}. \tag{4.6}$$

and

$$\vec{b'} = -\sqrt{3}a\sin(\theta)\hat{x} + \sqrt{3}a\cos(\theta)\hat{y}. \tag{4.7}$$

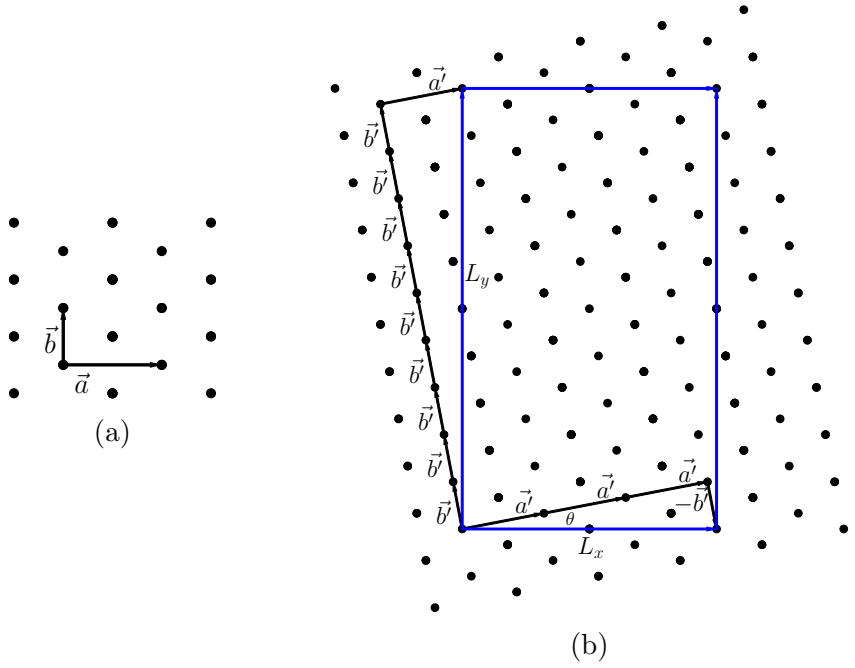

Figure 4.3: (a) Non–rotated lattice, and (b) rotated lattice. The black dots are lattice sites. In (b), the blue rectangle indicates one periodic unit cell for $\theta = \arctan(\frac{1}{3\sqrt{3}})$ with $(M, N) = (3, 1)$, $(I, J) = (1, 9)$.

In order to exactly fit a periodic structure into the numerical box, the dimension of the numerical box must accommodate multiples of these two basis vectors (an example is shown in Fig. 4.3b). Thus we have $M\vec{a'} - N\vec{b'} = L_x\hat{x} + 0\hat{y}$ and $I\vec{a'} + J\vec{b'} = 0\hat{x} + L_y\hat{y}$ where M, N, I and J are integers. From the components of the above vector equations that have a zero on the right–hand side, we obtain two conditions for the θ,

$$\tan(\theta) = \frac{N}{\sqrt{3}M} = \frac{\sqrt{3}I}{J} \tag{4.8}$$

Having four integers fulfilling $\frac{N}{M} = \frac{3I}{J}$, the dimensions of the numerical box and angle of rotations are given,

$$\begin{aligned} L_x &= \left(M\vec{a'} - N\vec{b'}\right) \cdot \hat{x}, \\ L_y &= \left(I\vec{b'} + J\vec{a'}\right) \cdot \hat{y}. \end{aligned} \tag{4.9}$$

In Fig. 4.4, we show the free–energy minimized density profiles of interface with $\theta = 0$ and $\theta = \arctan(\frac{1}{3\sqrt{3}})$.

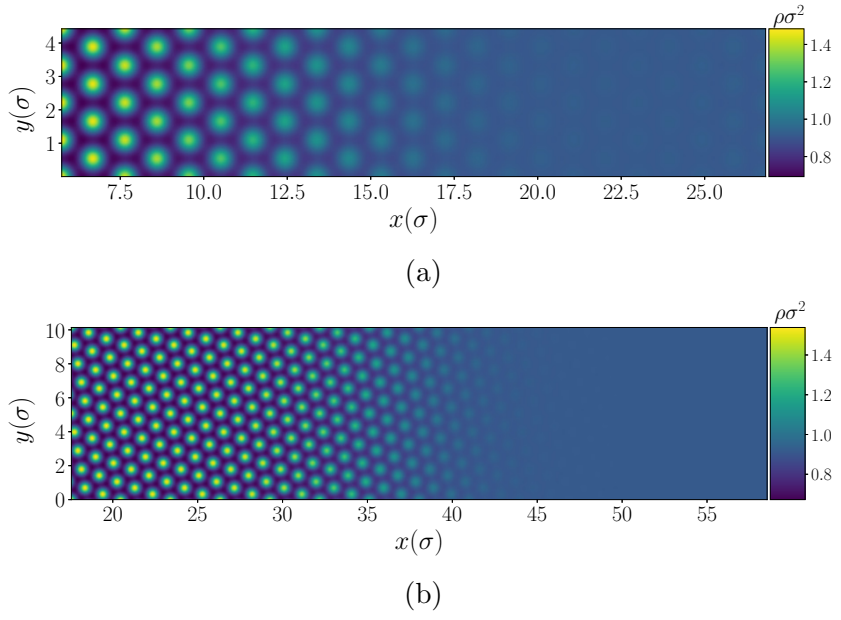

Figure 4.4: Example of (a part of) a planar interface with periodic condition in the y–direction. The full density profiles are periodic in both the x and y directions. (a) $\theta = 0$, and (b) $\theta = \arctan(\frac{1}{3\sqrt{3}})$ $\left(\frac{N}{M} = \frac{1}{3}, \frac{I}{J} = \frac{1}{9}\right)$. In these density profiles, the parameters are $\eta_{\rm cr} = 0.732$, $\eta_{\rm fl} = 0.711$ and lattice constant $a = 1.11\sigma$

4.2.1 Planar surface tension

For a planar interface in a rectangular numerical box (see Fig. 4.4 showing part of it), the free energy $\mathcal{F}$ can be decomposed into the contribution from bulk phases and interfaces:

$$\mathcal{F} = \mathfrak{f}_{\text{liquid}} L_{x,\text{liquid}} L_y + \mathfrak{f}_{\text{crystal}} L_{x,\text{crystal}} L_y + 2\gamma L_y, \tag{4.10}$$

where $L_{x,\text{liquid/crystal}}$ is the length of the liquid/crystal in the direction of the interface normal, L_y is the length of the interface, $\mathfrak{f}$ is the free energy density, and the factor 2 is from the periodic boundary condition.

After dividing both sides of Eq. (4.10) by the area of the simulation box $A = L_x L_y$, the surface tension γ is determined as the slope of the free energy density versus the inverse length of the numerical box in the direction of the interface normal L_x with fixed average particle density [37],i.e.,

$$\frac{\mathcal{F}}{A} = \mathfrak{f}_{\text{liquid}} \frac{L_{x,\text{liquid}}}{L_x} + \mathfrak{f}_{\text{crystal}} \frac{L_{x,\text{crystal}}}{L_x} + 2\gamma \frac{1}{L_x}. \tag{4.11}$$

Since the average particle density is fixed, we assume that $\frac{L_{x,\text{crystal/liquid}}}{L_x}$ is a constant for different L_x. Thus the advantage of Eq. (4.11) over Eq. (4.10) is that the precise coexisting free energy densities are not required and γ is directly determined by varying L_x.

The density profiles are initialized similar to Ref. [35]. In the iterations we chose a Picard mixing parameter constant in space and fix the average densities $\rho = \frac{\rho_{\text{cr}} + \rho_{\text{fl}}}{2}$ by adapting μ in the iterations, where $\rho_{\text{cr/fl}}$ is the bulk average density in the crystal/fluid phase at coexistence, and then finally perform the free minimization.

The result of $\gamma(\theta)$ by FMT is shown in Fig. 4.5. For a small anisotropy ϵ, γ can be fitted by $\gamma(\theta) = \gamma_0(1 + 6\epsilon\cos(\theta))$, and the comparison of the results by FMT and experiments are shown in Table 4.2. While the surface tension γ is in a good agreement with experiments, the anisotropy is 20 times smaller. The deviation most likely stems from long–ranged fluctuations in the interface which are averaged out in the framework of DFT. In the 3D HS systems, anisotropies also differ from simulations [32].

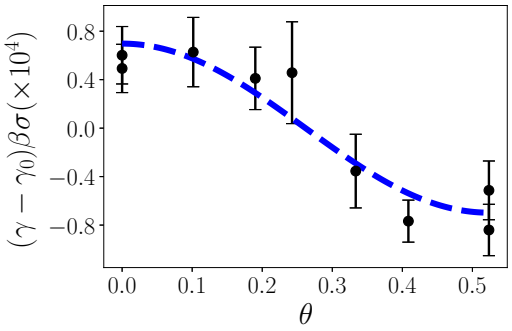

Figure 4.5: $\gamma(\theta)-\gamma_0$ for $a=11/4$. The black dots are FMT results and blue dashed line is $\gamma(\theta)-\gamma_0=\gamma_0(6\epsilon\sin(\theta))$ with $\gamma_0=0.09925$ and $\epsilon=-0.0007$.

Table 4.2: Thermodynamic properties of the one–component crystal–fluid transition. $\gamma(\theta)$ the surface tension, γ_0 denotes the averaged planar surface tension, and ϵ the anisotropy.

	FMT		Exp[11]*
	$a=11/4$	$a=3$	
$\beta\sigma\gamma(0)$	0.09921	0.08143	
$\beta\sigma\gamma(\frac{\pi}{6})$	0.09930	0.08155	
$\beta\sigma\gamma_0$	0.09925	0.08150	0.1
ϵ	-0.0007	-0.0007	-0.015

(* see Supplementary Material in Ref. [11])

4.3 Phase transition and crystal nuclei

In the thermodynamic limit ($N \to \infty$ and $V \to \infty$), the intensive variables, such as the chemical potential μ, must show a horizontal plateau throughout the fluid–crystal coexistence region.

However, for a finite size system, the fluid and solid part of the system arrange such that the interface between the two phases is minimal. This behavior gives rise to topologically different configurations, depending on the average density ρ. In Fig. 4.6, a schematic sketch of $\mu(\rho)$ as a function of ρ is shown.

The following configurations can be distinguished:

- $\rho < \rho_{\mathrm{fl}}$: The stable phase is an undersaturated fluid at these densities.
- $\rho_{\mathrm{fl}} < \rho < \rho_1$: In a finite system, the fluid is stable, up to a density ρ_1, where it becomes metastable. The chemical potential is larger than the coexistence value, $\mu > \mu_{\mathrm{co}}$.
- $\rho_1 < \rho < \rho_2$: A stable nucleus coexists with surrounding fluid. With the density increasing, the chemical potential decreases.
- $\rho_2 < \rho < \rho_3$: With the density increasing, the nucleus grows and eventually connects to itself over the periodic boundary. A slab configuration forms with two planar interfaces.
- $\rho_3 < \rho < \rho_4$: A fluid droplet in a surrounding crystal is formed.
- $\rho_4 < \rho$: For high enough densities, the stable phase is the crystalline phase. In the thermodynamic limit, crystallization starts at a density of ρ_{cr}.

Surface tension of crystal nuclei

The surface tension γ plays a crucial role in the free energy barrier for nucleation in classical nucleation theory. With the crystal nuclei stabilized in the finite numerical boxes, we could determine γ versus the size of nuclei. Since the anisotropy is small (see Tab. 4.2), we approximate a nucleus as a perfect spherical disk with radius R. The difference of grand potential $\Delta\Omega$ between a nucleus and a homogeneous fluid reads

$$\Delta\Omega = -\pi R^2 \Delta P + \gamma(R) 2\pi R. \tag{4.12}$$

Minimizing $\Delta\Omega$ with respect to R gives

$$\gamma(R) = R\Delta P, \tag{4.13}$$

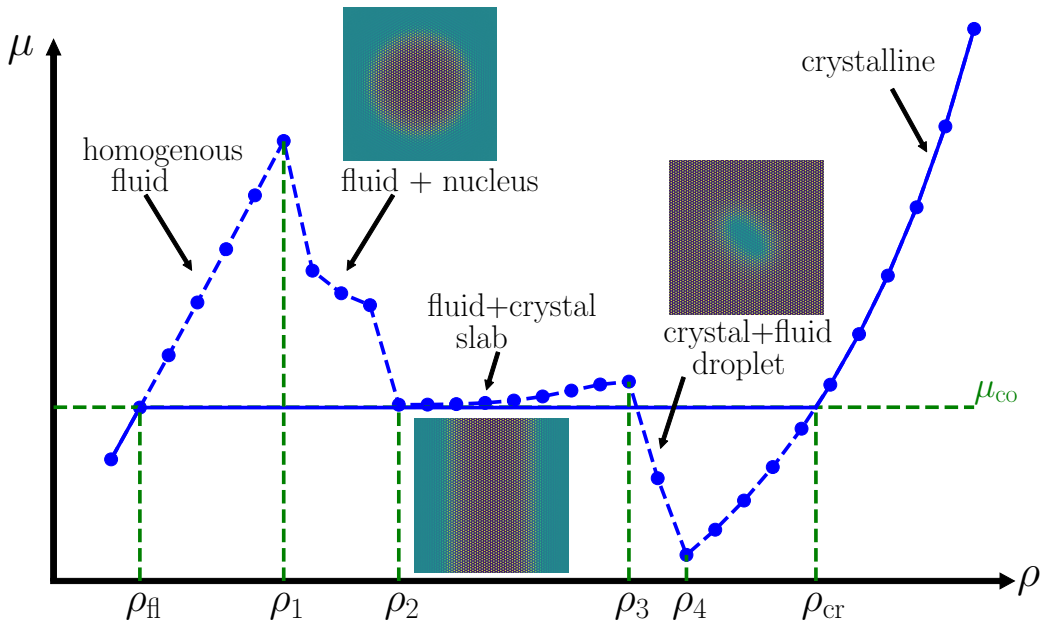

Figure 4.6: A schematic description of the chemical potential $\mu(\rho)$ as a function of ρ. The solid line is a fluid to crystal transition in the thermodynamic limit. The dashed line and dots are results from FMT equilibrium states in a finite but large numerical box ($64\sigma \times 64\sigma$ here). The finite system is initialized with a disk–shaped nucleus in the center, and the average density (fixed during free energy minimization) is tuned by varying the size of initial the nucleus and the density of surrounding fluid. The free energy minimization is performed by using dynamic DFT (see Appendix B for details). The density profiles in the insets are examples of corresponding configurations.

with $\Delta P = P_{\rm cr} - P_{\rm fl}$ and $P_{\rm cr/fl}$ the pressure in the nucleus/fluid far from interface. It is worth to note that Eq. (4.13) is the definition of the Laplace pressure. Thus, the nucleus radius (R) is determined by

$$\Delta\Omega = \pi R^2 \Delta P. \tag{4.14}$$

Numerically, $\Delta\Omega = \Omega_{\rm system} - \Omega_{\rm fl}(\mu_{\rm eq})$, where $\mu_{\rm eq}$ is equilibrium chemical potential (not $\mu_{\rm co}$). $\Omega_{\rm system}$ is directly evaluated by the equilibrium density profile, and $\Omega_{\rm fl}(\mu_{\rm eq})$ and $P_{\rm fl}(\mu_{\rm eq})$ are from the equation of state. $P_{\rm cr}$ is approximated by a unit cell in the middle of the nucleus, since it gives a more consistent result than the equation of state.

Using Eqs. (4.13) and (4.14) with ΔP and $\Delta\Omega$, we determine R and $\gamma(R)$ for a nucleus. Furthermore, by varying size and average density of the system, we obtain nuclei with different radii. In Fig. 4.7, we show both $\frac{\gamma_0}{\gamma} - 1$

as a function of $1/R$ and $\frac{\gamma}{\gamma_0}$ as a function of R, and the standard fit with the Tolman correction [38, 39]:

$$\frac{\gamma(R)}{\gamma_0} \simeq \frac{1}{1-\frac{\delta}{R}} \Rightarrow \frac{\gamma_0}{\gamma(R)} - 1 \simeq -\frac{\delta}{R} \tag{4.15}$$

with δ the Tolman length.

In Fig. 4.7, $\gamma(R)$ first increases and then decreases as R increases, and the fit gives $\delta = 0.9\sigma$. The δ falls in the possible regime ($\pm 1\sigma$) from the 3D hard–sphere DFT studies [40] and the magnitude is close to that determined from the (pseudo) hard–sphere simulations while the sign is different [41, 42]. It is difficult to judge the relevance of δ from this work since the sign and the magnitude have been subjest of a longstanding controversy [43, 44, 45, 46, 47] and studies on 2D systems are rare [48].

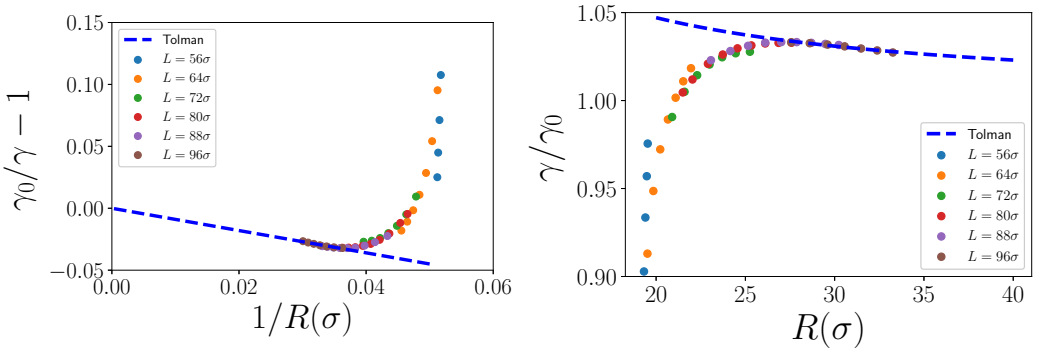

(a) (b)

Figure 4.7: (a) $\gamma_0/\gamma(R) - 1$ versus $1/R$, and (b) $\gamma(R)/\gamma_0$ versus R. Same color dots are same system size (L^2). The blue dashed line is a fitting by using the Tolman correction, which gives $\delta = 0.9$.

4.4 Hexatic phase

The melting transition in 2D, unlike 3D, is proposed to proceed via an additional 'hexatic' phase between the fluid and crystalline phase. The hexatic phase is strongly related to the appearance of topological defects. There are three main types of defect in 2D HD systems: dislocations, dislocation pairs and disclinations. The dislocation is a pair of five– and seven– fold coordinated particles (five and seven nearest neighbors), a dislocation pair is composed by two dislocations, and a disclination is a single five– or seven–fold coordinated particle.

The existence of the hexatic phase is proposed by the KTHNY theory with the name derived from Kosterlitz, Thouless, Halperin, Nelson, and Young [49, 50, 51, 52, 53]; for hard disks, simulations and experiments have proved it in 2011 [10] and 2017 [11] respectively. However, to our knowledge, there is no functional in DFT so far able to capture the hexatic phase.

Here we briefly describe the melting scenario of 2D melting proposed by the KTHNY theory. Rigorously speaking, no true crystal exists in 2D due to long wavelength fluctuations [54], but practically the crystal phase in simulations and experiments has the appearance of a conventional periodic crystal. For high packing fractions, 2D HD form a crystalline phase, where the translational order is quasi–long–ranged and the bond–orientational order is long–ranged, and the only type of defect are dislocation pairs. As packing fraction decreases, dislocation pairs start unbinding and thus destroy the quasi–long–ranged translational order while the long–ranged bond–orientational becomes quasi–long–ranged. This phase is called 'hexatic phase'. As the packing fraction further decreases, dislocations unbind into individual disclinations and both translational order and bond–orientational order are short–ranged and the system becomes fluid. In 3D, the unbinding free energy of dislocation pairs is too high thus there is no hexatic phase.

To determine whether the translational order is long or short–ranged, in simulation the vector pair correlation function $g(\Delta\mathbf{r})$ is used, which is defined as

$$g(\Delta\mathbf{r}) = \frac{V}{N^2}\left\langle \sum_{ij,i\neq j} \delta(\Delta\mathbf{r} - \mathbf{r}_j + \mathbf{r}_i) \right\rangle. \tag{4.16}$$

To connect with DFT, we consider the two particle density introduced in Sec. 3.2,

$$\rho^{(2)}(\mathbf{r},\mathbf{r}') = \left\langle \sum_{ij,i\neq j} \delta(\mathbf{r} - \mathbf{r}_i)\delta(\mathbf{r}' - \mathbf{r}_j) \right\rangle, \tag{4.17}$$

and rewrite with $\mathbf{r}' = \mathbf{r} + \Delta\mathbf{r}$,

$$\begin{aligned} \rho^{(2)}(\mathbf{r},\mathbf{r}+\Delta\mathbf{r}) &= \left\langle \sum_{ij,i\neq j} \delta(\mathbf{r} - \mathbf{r}_i)\delta(\mathbf{r} + \Delta\mathbf{r} - \mathbf{r}_j) \right\rangle \\ &= \rho(\mathbf{r})\rho(\mathbf{r}+\Delta\mathbf{r})g(\mathbf{r},\mathbf{r}+\Delta\mathbf{r}). \end{aligned} \tag{4.18}$$

Further, by using the delta function property

$$\int d\mathbf{r} \left\langle \sum_{ij,i\neq j} \delta(\mathbf{r} - \mathbf{r}_i)\delta(\mathbf{r} + \Delta\mathbf{r} - \mathbf{r}_j) \right\rangle = \left\langle \sum_{ij,i\neq j} \delta\left(\Delta\mathbf{r} - \mathbf{r}_j + \mathbf{r}_i\right) \right\rangle, \tag{4.19}$$

we obtain

$$g(\Delta\mathbf{r}) = \frac{V}{N^2}\int d\mathbf{r}\,\rho^{(2)}(\mathbf{r},\mathbf{r}+\Delta\mathbf{r}) = \frac{V}{N^2}\int d\mathbf{r}\,\rho(\mathbf{r})\rho(\mathbf{r}+\Delta\mathbf{r})g(\mathbf{r},\mathbf{r}+\Delta\mathbf{r}). \tag{4.20}$$

In the homogeneous system, $\rho^{(2)}$ is independent of $\mathbf{r}$ and thus

$$g(\Delta\mathbf{r}) = \frac{V^2}{N^2}\rho^2 g(\Delta r) = g(\Delta r). \tag{4.21}$$

On the other hand, in an inhomogeneous system, $g(\mathbf{r},\mathbf{r}+\Delta\mathbf{r})$ depends on $\mathbf{r}$ and is unknown in general. Therefore, we assume that $g(\mathbf{r},\mathbf{r}+\Delta\mathbf{r}) \simeq 1$ when $|\Delta\mathbf{r}| \gg 1$, and then $g(\Delta\mathbf{r})$ is the autocorrelation of $\rho(\mathbf{r})$, i.e.

$$g(\Delta\mathbf{r}) \simeq \frac{V}{N^2}\int d\mathbf{r}\rho(\mathbf{r})\rho(\mathbf{r}+\Delta\mathbf{r}). \tag{4.22}$$

The KTHNY theory proposes that $g(\Delta\mathbf{r})-1$ decays algebraically in the crystalline phase, i.e. proportional to $|\Delta\mathbf{r}|^{-\xi}$ with $\frac{1}{4} < \xi < \frac{1}{3}$, and exponentially in the hexatic phase. To exam that in FMT, we choose a large numerical box and initialized a homogeneous fluid with random density fluctuation, and then perform dynamic DFT until it reaches the equilibrium state. In the end, we find that dislocations survive as shown in Fig. 4.8. As shown in Fig. 4.9, $g(\Delta\mathbf{r})-1$ decays faster than $|\Delta\mathbf{r}|^{-1/3}$ for a packing fraction $\eta = 0.732$.

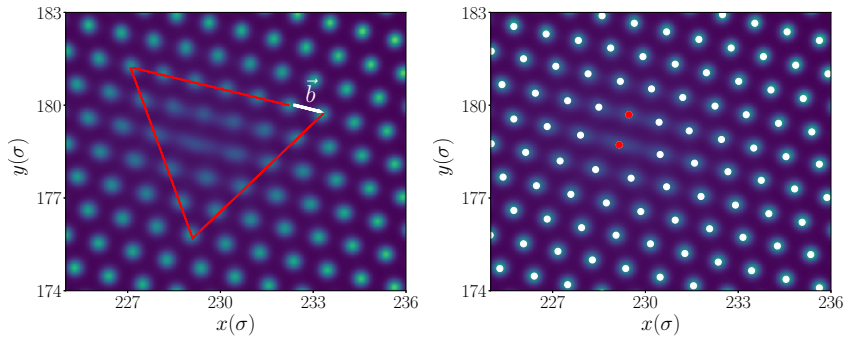

(a) Burger's Vector (b) Dislocation.

Figure 4.8: A dislocation survives in the equilibrium density profile. (a)Burgers vector $\vec{b}$. (b)Red dots are a 5–7 dislocation and white dots are particles with 6 neighbors. The average packing fraction $\bar{\eta} = 0.732$ and the simulation box is $280\sigma \times 280\sigma$.

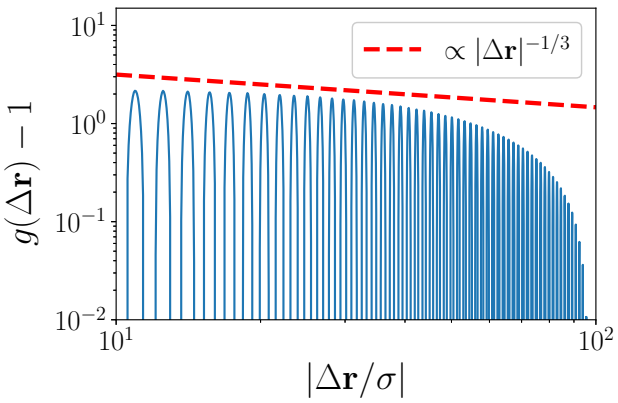

Figure 4.9: Log–log plot for $g(\Delta\mathbf{r}) - 1$ as a function of $|\Delta\mathbf{r}|$. The red dashed line is the stable limit purposed by KTHNY theory. The average packing fraction $\bar{\eta} = 0.732$ and the numerical box is $280\sigma \times 280\sigma$.

However, there are several issues. First, we can not rule out that the dislocations result from mechanical stress. As the numeric box is square in this case ($280\sigma \times 280\sigma$), it can not fit a perfect equilibrium crystal and the stress must result in a distorted crystal or in dislocations, and both cases are possible local minimums. In simulations, the simulation boxes go up to $\sim 1000\sigma \times 1000\sigma$ to eliminate the influence of stress. Second, for higher packing fractions, we are not sure whether $g(\Delta\mathbf{r}) - 1$ decays algebraically and dislocation pairs exist or not. Third, in DFT, a density profile should be an ensemble average and can be viewed as an average of snapshots in simulations/experiments. With dislocations fluctuating (moving around) in simulations, the corresponding density profile should be crystal–like with high vacancy concentration; thus, the 'explicit' dislocation shown in Fig. 4.8 means it is trapped locally, which differs from the simulation picture. Fourth, we are unsure how dislocations contribute to the free energy. That is to say, if dislocations or interaction among dislocations can contribute negative free energy in a large system, a crystal with intrinsic dislocations could be favored over a pure crystalline phase, i.e. $\mathcal{F}_{\text{dislocation}+\text{crystal}} < \mathcal{F}_{\text{stressed crystal}}$.

Last but not least, the existence of the hexatic phase stems from the 'intrinsic' long–ranged fluctuations [54], but in FMT, as pointed out in Ref. [32], the long–ranged fluctuations in the interface are averaged out; thus it is unlikely to have intrinsic long–ranged fluctuations in 2D FMT. However, to resolve the above mentioned issues, we need even bigger systems, more density profiles with higher/lower density and different initial condition to verify the existence of the hexatic phase or whether dislocations can survive in a large system or not; unfortunately this is beyond the limitation of our current

computational resources. Fig. 4.9 took more than one month using a NVIDA K40 GPU.

4.5 Conclusion

In this chapter we have shown the FMT free energy functional for the 2D HD successfully delivers an accurate mean surface tension and thermodynamic properties in comparison with simulations and experiments. However the anisotropy of the surface tension differs up to a factor of 20 comparing to that from experiments. A possible reason is that DFT smears out the long–ranged fluctuations. Furthermore, we investigate the surface tension of disk–shaped nuclei, $\gamma(R)$, with R the nucleus radius. The $\gamma(R)$ first increases then decreases as R increases. The Tolman length by the fitting with the Tolman correction falls in the possible regime ($\pm 1\sigma$) from the 3D hard–sphere DFT studies [40] and the magnitude is close to that determined from the hard–sphere simulations while the sign is different [41, 42]. Finally, we have investigated the existence of the hexatic phase. For $\eta = 0.732$, we find that $g(\Delta\mathbf{r}) - 1$ decays faster than algebraically while the density profile still maintains the crystalline structure with dislocations, which is evidence of the existence of the hexatic phase. However, we are unsure whether the dislocations result from stress, and whether intrinsic long–ranged fluctuations exist in DFT or not. Thus, further investigations are needed.

Chapter 5

Hard–disk binary mixtures

Partial results of this chapter have been published in: Physical Review E 98.1.012608 (2018) with the title "Phase diagrams and crystal–fluid surface tensions in additive and nonadditive two–dimensional binary hard–disk mixtures"[55]

In this chapter, we employ the FMT functional of Ref. [3] (see also Sec. 3.3.2) to study phase diagrams and crystal–fluid surface tensions for additive and nonadditive binary hard–disk mixtures. We consider a mixture of large (l) and small (s) disks, with diameter σ_l and σ_s, respectively, and $q = \frac{\sigma_\mathrm{s}}{\sigma_\mathrm{l}}$ denoting the size ratio. In the case of an additive system (denoted as HD mixture), one may define an interaction diameter $d_{ij} = \sigma_i/2 + \sigma_j/2$ with $i, j = \{\mathrm{l}, \mathrm{s}\}$. The pair potential $\Phi^{ij}(r)$ between two particles with center-center distance r is ∞ for $r < d_{ij}$ and 0 for $r > d_{ij}$.

On the other hand, we consider a mixture in which the interaction between two small disks is zero, i.e. they behave as an ideal gas and the other interactions (large–large and large–small) remain unchanged. This mixture is the 2D variant [13] of the well–known Asakura–Oosawa (AO) model [14, 15], and we denote this kind of mixtures as AO mixture.

As shown in Fig. 5.1, if the distance of two large disks is less than $\sigma_\mathrm{l} + \sigma_\mathrm{s}$, there will be a overlap of excluded area for small disks; i.e. the small disks will act as a depletant and induce an effective two–body attractive potential between the large disks. This effect is an example of an entropic force. In the case of an AO mixture, the effective potential among large disks can be

analytically determined (in the low density limit) [14, 13] as:

$$\beta\Phi^{\mathrm{AO}}(r) = \begin{cases} \infty \text{ if } r < \sigma_{\mathrm{l}} \\ -\eta' \left[\cos^{-1}\left(\frac{r}{\sigma_{\mathrm{l}}(1+q)}\right) - \frac{r}{\sigma_{\mathrm{l}}(1+q)} \sqrt{1 - (\frac{r}{\sigma_{\mathrm{l}}(1+q)})^2} \right] \\ \qquad\qquad \text{if } \sigma_{\mathrm{l}} < r < \sigma_{\mathrm{l}} + \sigma_{\mathrm{s}} \\ 0 \text{ otherwise,} \end{cases} \tag{5.1}$$

where $\eta' = \frac{\sigma_{\mathrm{s}}^2}{2}\rho_{\mathrm{s}} \left(\frac{1+q}{q}\right)^2$ determines the magnitude of the depletion potential (ρ_{s} is the bulk number density of small disks). Furthermore, $\beta = \frac{1}{k_{\mathrm{B}}T}$, with k_{B} denoting Boltzmann's constant, and T temperature. For small size ratios $q = \frac{\sigma_{\mathrm{s}}}{\sigma_{\mathrm{l}}} \leq \frac{2-\sqrt{3}}{\sqrt{3}} \simeq 0.155$, the AO mixture can be mapped exactly onto a single component model with an effective two–body potential given by the depletion potential above. For larger q, the effective potential should include n–body overlaps of excluded area ($n \geq 3$). Furthermore, in the dilute limit of the (additive) HD mixture (with the number density ρ_{l} of large disks being small), the effective potential between large disks is identical to Eq. (5.1) [13].

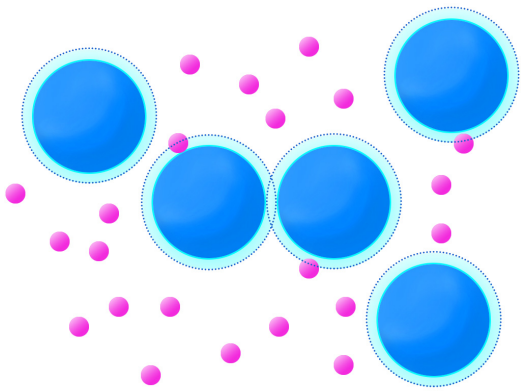

Figure 5.1: A schematic plot of entropic force. A dark blue disk is a large HD with a diameter σ_{l} and a red disk is a small disk with a diameter σ_{s}. The light blue region with dashed circle surrounding every HD is excluded area for the centers of the small disks. When the HD get close enough, as shown in the center of the plot, the excluded area surrounding the HD intersect. The overlap results in a reduced excluded area, which increases the total available area for small disks and thus the entropy.

5.1 Free energy functional

Here we adapt the 2D FMT (see Sec. 3.3.2) for the free energy functional. In the HD case, the only difference is that the weighted densities n_α are sums over convolutions of the HD species density profiles with weight functions,

$$\begin{aligned} n_\alpha(\mathbf{r}) &= \sum_{i=\{\mathrm{s,l}\}} \int d\mathbf{r}'\, \rho_i(\mathbf{r}') w_\alpha^i(\mathbf{r}-\mathbf{r}') \\ &=: n_\alpha^{\mathrm{s}} + n_\alpha^{\mathrm{l}} \end{aligned} \tag{5.2}$$

where α indicates the type of weight function and i the species (l=large and s=small).

The functional for the AO mixture can be obtained by the 'linearization recipe': The direct correlation function between two small particles should vanish in order to be consistent with the small species behaving as an ideal gas, i.e.,

$$C_{\mathrm{ss}}^{(2)}(\mathbf{r},\mathbf{r}') = -\beta \frac{\delta^2 \mathcal{F}^{\mathrm{ex}}}{\delta\rho_{\mathrm{s}}(\mathbf{r})\delta\rho_{\mathrm{s}}(\mathbf{r}')} \stackrel{!}{=} 0. \tag{5.3}$$

In 3D, such a functional (derived from the original Rosenfeld functional [4]) describes structural properties and wetting transitions in the fluid phase very well [56]. According to the linearization recipe, the AO mixture excess free energy density is given by

$$\Phi^{\mathrm{AO}}\left(\left\{n_\alpha^{\mathrm{l}}, n_\alpha^{\mathrm{s}}\right\}\right) = \Phi^{\mathrm{HD}}\left(n_\alpha^{\mathrm{l}}\right) + \sum_\alpha n_\alpha^{\mathrm{s}} \frac{\partial \Phi^{\mathrm{HD}}\left(n_\alpha^{\mathrm{l}}\right)}{\partial n_\alpha^{\mathrm{l}}} \,. \tag{5.4}$$

Furthermore, the small species density profile is computed by the grand–canonical equilibrium condition which can be solved explicitly:

$$\frac{\delta\Omega[\rho_{\mathrm{l}},\rho_{\mathrm{s}}]}{\delta\rho_{\mathrm{s}}} \stackrel{!}{=} 0 \Rightarrow \rho_{\mathrm{s}}(\mathbf{r}) = \exp\left(\beta\mu_{\mathrm{s}} - \int d\mathbf{r}' \sum_\alpha \frac{\partial \Phi_{\mathrm{ex}}^{\mathrm{HD}}\left[n_\alpha^l\right]}{\partial n_\alpha^{\mathrm{l}}} w_\alpha^{\mathrm{s}}(\mathbf{r}'-\mathbf{r})\right), \tag{5.5}$$

and the remaining free energy minimization with respect to $\rho_{\mathrm{l}}(\mathbf{r})$ is similar as in Sec. 4.1.1.

5.2 Crystal density profiles

When the radii of the disks are comparable (large $q \lesssim 1$), we observe a clear substitutional disorder. Density peaks for both species are centered on the triangular lattice points and their magnitude is essentially determined by the composition of the crystal. An example can be seen in the crystal part of the crystal–fluid density profile shown in Fig. 5.8e below.

For small size ratios $q \ll 1$, we observe interstitial disorder, i.e. the small disks almost exclusively occupy the interstitial space between the large disks which in turn occupy the triangular lattice points. An example can be seen in the crystal part of the crystal–fluid density profile shown in Fig. 5.8a. The HD and AO case are very similar, and qualitatively the AO crystal density profiles in 3D show the same behavior [57].

For intermediate q and the HD case, we observe a superposition of substitutional and interstitial disorder, and the interstitial disorder may show a transition to different alloy configurations upon changing the composition. We exemplify this for $q = 0.45$. Large disks density peaks are again centered on the triangular lattice positions (not shown). For low small disk concentrations (see Fig. 5.2a), we observe interstitial disorder superficially compatible with an AB_2 structure. From the large and small disks drawn in Fig. 5.2a one sees however that the small disks are too big for the formation of a true AB_2 phase. For higher small disk concentrations (see Fig. 5.2b) the lattice constant becomes smaller (large spheres on the triangular lattice points almost touch) and the interstitial density peaks of the small spheres are compatible with an AB_3 structure. Here, remarkably, the large disks drawn around the triangular lattice points and the small disks drawn around the interstitial peak positions reveal two packed AB_3 configurations. In the AO case, we only observed small disk density distributions of the type shown in Fig. 5.2a.

Here, we have not investigated whether the minimized crystal structures with disorder are stable or not with respect to phase separation into different alloy phases. This requires more extensive investigations beyond the scope of this work. However, our results illustrate that a free minimization of the FMT functional is capable of generating alloy structures without the need to explicitly parameterize the density profiles (e.g. by suitably chosen Gauss peaks, as it is often done), see for example the AB_3 structure in Fig. 5.2 and the AB_6 structure in Fig. 5.3 with the appropriate size ratio [58].

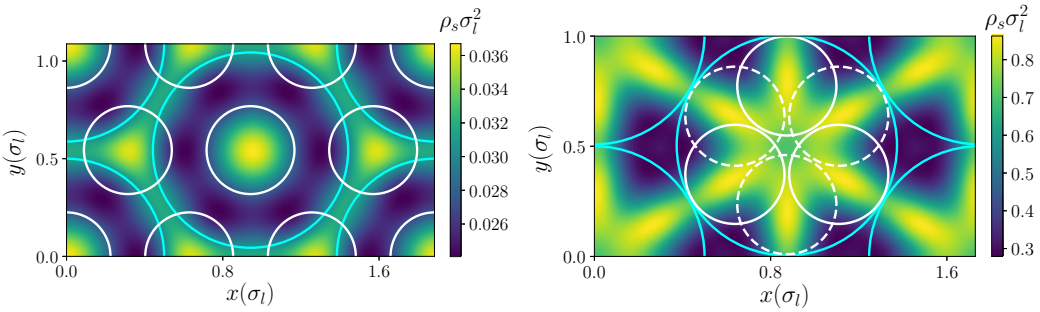

(a) $c_s = 0.03$ (b) $c_s = 0.39$

Figure 5.2: Density profiles for small disks in a HD mixture crystal with $q = 0.45$ at crystal–fluid coexistence for small disk concentration $c_s = 0.03$(a) and $c_s = 0.39$(b), with $c_s = \rho_s/(\rho_s + \rho_l)$. The solid blue circles indicate the extension of large disks, solid and dashed white circles indicate the extension of small disks. In both cases, the density profile is a superposition of substitutional and interstitial disorder. In (b), interstitial disorder dominates and is compatible with an AB_3 alloy structure where one large disk is replaced by three small disks (white solid or dashed circles) .

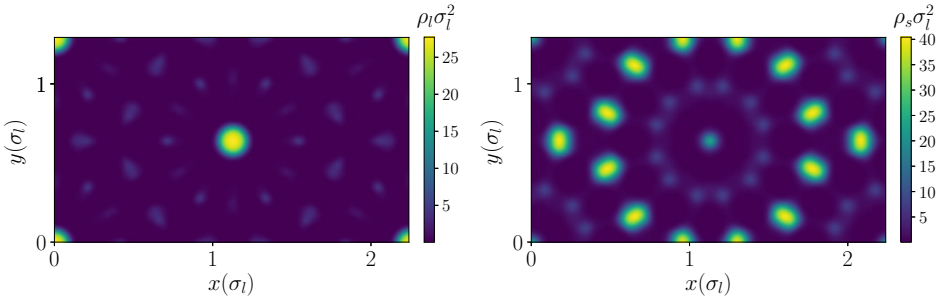

(a) $\rho_l\sigma_l^2$ (b) $\rho_s\sigma_l^2$

Figure 5.3: Density profiles for large and small disks in am AB_6 HD mixture crystal with $q \simeq 0.349$. (a) large disks $\rho_l\sigma_l^2$. (b) small disks $\rho_s\sigma_l^2$.

5.3 Phase diagrams

For two–component systems, equilibrium states are on a surface in a three–dimensional space, spanned by e.g. the packing fractions η_l, η_s and the pressure P. Consequently, binodals are lines in this three–dimensional space and they are often displayed by their two–dimensional projections, e.g. lines in the η_l–P or $c_{\mathrm{s/l}}$–P plane where $c_{\mathrm{s/l}} = \rho_{\mathrm{s/l}}/(\rho_\mathrm{l} + \rho_\mathrm{s})$ is the relative concentration of small/large spheres. In the AO model, customarily the η_l–μ_s plane is chosen but the topology of phase diagrams is very similar to the one in the η_l–P plane.

For a size ratio $q = 0.15$, the phase diagram is shown in Fig. 5.4 in two different projections. For both HD and AO mixtures, the addition of the small species leads to an increased coexistence pressure for the fluid–crystal transition, i.e. the fluid phase is stabilized. The AO mixture shows the typical widening of the coexistence gap ($\eta_{\mathrm{l,cr}} - \eta_{\mathrm{l,fl}}$) with increasing concentration of the small species (see Fig. 5.4a), smoothly leading to a sublimation line. For $\eta_\mathrm{s} \lesssim 0.01$, the HD mixture binodal follows the AO binodal, i.e. also shows an initial widening of the coexistence gap. This could be expected since for these small concentrations the small disks only act as depletants and their mutual interaction is irrelevant. For higher η_s, the binodals separate. The choice of the parameter a in the functional has a significant influence on the location of the binodal. This is similar to the observation in Ref. [57] that also in the 3D case, the binodal differs considerably between the White Bear II (tensorial) and the Rosenfeld (tensorial) functional, although the differences in the one–component case are not that significant.

5.3.1 Small size ratios q

For the size ratios $q = 0.3$ and $q = 0.45$, the phase diagrams are shown in Fig. 5.5 in the η_l–P plane. For the AO mixture, the liquid (rich in large disks)–vapor (poor in large disks) transition has become stable which leads to the appearance of a triple point above which sublimation (the vapor–crystal transition) is stable. The triple point pressure decreases with increasing q. The difference in the location of the liquid–vapor transition between the FMT results for the two different values of a is only a consequence of normalizing the pressure axis by $P_\mathrm{co}^\mathrm{1c}$ (for the two a values, it differs by $\sim 15\%$, see Table 4.1). For the HD mixtures, there is no fluid–fluid transition and there is hardly any widening of the coexistence gap of the fluid–crystal transition visible.

The results for the AO mixture are very similar to the 3D case [57]. Experimentally, it is possible to realize such 2D systems by sedimented monolayers

of colloidal spheres (as in Refs. [12, 11]) to which nonadsorbing polymers can be added. For small size ratios $q \lesssim 0.15$ it would be interesting to study experimentally or by simulations the fate of the established melting scenario for hard disks as the polymer concentration is increased. As we have seen, the coexistence gap continuously widens in this case, and we expect that towards the sublimation regime only the first–order transition survives.

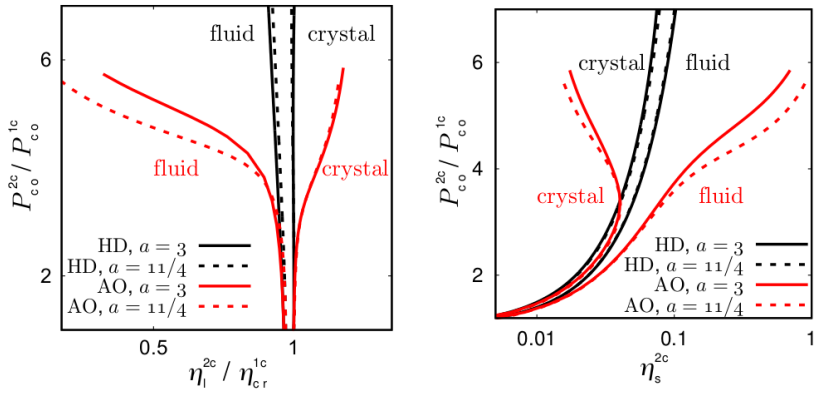

(a) (b)

Figure 5.4: Phase diagram for the size ratio $q = 0.15$ in (a) the η_l–P plane and in (b) the η_s–P plane. In (a), pressure and packing fraction are normalized by the coexistence values of the 1–component HD system P_{co}^{1c} and η_{cr}^{1c}.

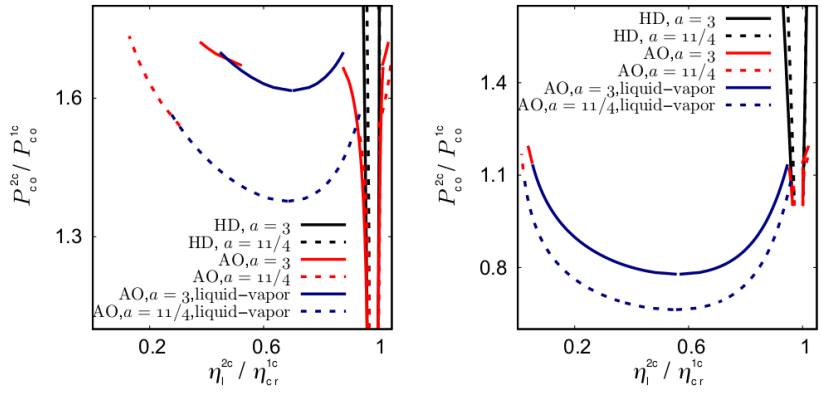

(a) $q = 0.3$ (b) $q = 0.45$

Figure 5.5: Binary mixture phase diagrams for $q = 0.3$ (a) and $q = 0.45$ (b) in the η_l–P plane. Pressure and packing fraction are normalized by the coexistence values of the 1–component HD system P_{co}^{1c} and η_{cr}^{1c}. The triple point pressures are indicated by horizontal dotted lines.

5.3.2 Intermediate size ratios q

Here we will only discuss HD mixtures. The phase diagram for $q = 0.6$ is shown in Fig. 5.6(a) and for $q = 0.7$ in Fig. 5.6(b),(c). For $q = 0.6$, we observe a phase diagram of the eutectic type. It is actually very similar to the phase diagram found in simulations for $q = 1/1.4$ (see Ref. [59] Supplementary Material). The crossover to the azeotropic phase diagram (in which two crystal lines meet, as seen for $q = 0.75$ in Fig. 5.7(c)) is surprising according to the FMT results.

For $q = 0.7$, a three–dimensional phase diagram in η_l–η_s–P space is shown in Fig. 5.6(c). The coexistence surface with a majority of large disks (black surface) is close to the one of small disks (blue surface), but does not cross it. By increasing q, the two surfaces touch and form a phase diagram of an azeotropic type. Back to the η_l–P plane, the branch with a majority of large disks distorts to form an azeotropic point (see the black lines in Fig. 5.6(b)) whereas the branch with a majority of small disks remains approximately unchanged when compared with $q = 0.6$ (blue lines in Fig. 5.6(b)). Thus, above the azeotropic point pressure there is a stable and a metastable coexistence between a crystal with a majority of small disks and a mixed fluid.

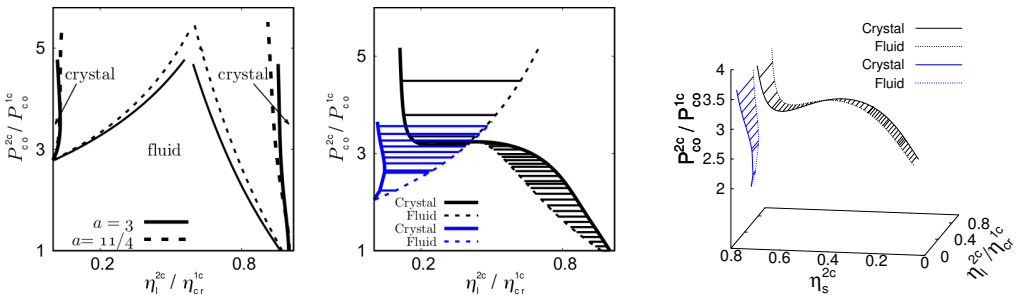

(a) $q = 0.6$ (b) $q = 0.7$ (c) $q = 0.7$ in η_l–η_s–P space

Figure 5.6: Binary mixture phase diagrams for $q = 0.6$ (a) and $q = 0.7$ (b), (c). Only the results for $a = 3$ are shown in (b), (c).

5.3.3 Size ratios q close to 1

For size ratios q in the vicinity of 1, we again only focus on the HD mixture (in the AO mixture, the phase diagram becomes rather uninteresting with regard to crystal phases. There, upon the addition of the smaller, polymeric component the one–component crystal does not change very much: the polymers fill up the vacancies until the triple point is reached and the

fluid–crystal transition becomes unstable with respect to sublimation. This is very similar to the 3D case, and a detailed discussion can be found in Ref. [57]). For HD mixtures, phase diagrams are shown in Fig. 5.7. For q very close to 1, the phase diagram is of a type commonly denoted as spindle type (which would be directly visible in the c_{l}-P plane or in the c_{s}-P plane): The coexistence pressure continuously increasing upon the addition of smaller disks and reaches its maximum for the pure small-disk system (see Fig. 5.7(a)) Upon lowering q, the type of phase diagram crosses over to azeotropic (see Fig. 5.7(b) and (c)): there, a maximum pressure for a stable fluid is found for a certain finite composition, i.e. for a truly mixed system. At this point of maximum pressure, the coexisting fluid and crystal have the same composition (azeotropic point). The precise value for q where this transition happens depends on the parameter a in the functional; it is around 0.91 for $a = 3$ and around 0.93 for $a = 11/4$. The transition from spindle–type to azeotropic phase diagrams has also been observed in simulations of hard–sphere mixtures in 3D [60]. There, the transition happens at around $q = 0.94$. Furthermore, in 3D the azeotropic phase diagram changes to a eutectic phase diagram already at around $q = 0.88$. From our results, this happens in 2D at much lower q (see the discussion in Sec. 5.3.2).

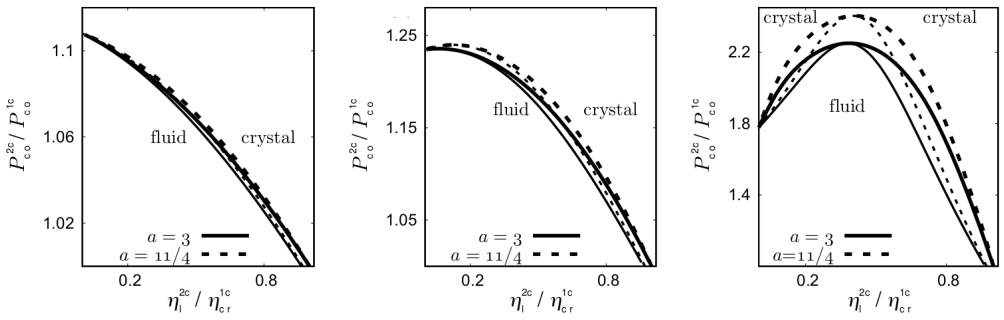

(a) $q = 0.95$ (b) $q = 0.9$ (c) $q = 0.75$

Figure 5.7: Binary mixture phase diagrams for $q = 0.95$ (a), $q = 0.9$ (b) and $q = 0.75$ (c) in the η_{l}–P plane. Pressure and packing fraction are normalized by the coexistence values of the 1–component HD system $P_{\mathrm{co}}^{1\mathrm{c}}$ and $\eta_{\mathrm{cr}}^{1\mathrm{c}}$.

5.4 Interface density profiles

Fiq. 5.8 shows representative density profiles of the crystal–fluid interface for hard–disk mixtures with $q = 0.15, 0.45$ and 0.75. For all size ratios q, the density of large disks is always peaked on the triangular lattice sites (see Fig. 5.8a) while the density of small disks changes from interstitial to substitutional disorder by increasing q (see also the discussion in Sec. 5.2). For the AO mixture, we found similar density profiles for $q < 0.5$, except Fig. 5.8d. From the profiles one infers a rather broad interface.

We analyze the interface structure further by employing the methods of Ref. [61]. Smooth average density and crystallinity modes can be extracted from the Fourier transform of the full density profiles by picking a lateral reciprocal lattice vector ($\mathbf{K}_y$) and cutting out a window around a reciprocal lattice vector $\mathbf{K}_x$ parallel to the interface normal. The average modes are the inverse Fourier transforms of the cut–out window. The average density mode M_0 is obtained by choosing $\mathbf{K}_x = \mathbf{K}_y = 0$ and the leading crystallinity mode M_1 is obtained by choosing $\mathbf{K}_y = 0, \mathbf{K}_x = 4\pi/\left(\sqrt{3}L\right)$ where L is the length of the rectangular unit cell side which is parallel to the interface, see Fig. 5.8. M_1 is complex in general, in figures we show its absolute value only.

In Fig. 5.9 we compare laterally averaged density profiles with the extracted density and crystallinity modes for the four interfaces of Fig. 5.8. Several observations can be made. First, looking at the density and crystallinity mode of large disks (middle column in Fig. 5.9) we note that coming from the fluid side, crystallinity sets in earlier than densification (except for the case $q = 0.45$, $c_\mathrm{s} = 0.39$). This has also been noted before in the 3D case of one–component hard spheres [61]. Second, looking at the density and crystallinity mode of small disks (right column in Fig. 5.9) we observe that for small $q = 0.15$ (interstitial disorder) and large $q = 0.75$ (substitutional disorder) the small disk crystallinity is essentially proportional to the large disk crystallinity. Since the crystal has a smaller concentration of small disks than in the fluid, the density mode increases from left to right but stays monotonic. For the intermediate size ratio $q = 0.45$ we note that the crystallinity of small disks is peaked at the interface, and for $c_\mathrm{s} = 0.39$ this also applies to the density mode. Thus we see an interfacial enrichment of ordered, small spheres. This interfacial enrichment can be also seen in the laterally averaged density profiles (left column in Fig. 5.9) which exhibit an increase in the oscillation amplitude of the small sphere density (red lines) in the interfacial region. However, the quantification of this effect is easier using the crystallinity and density modes.

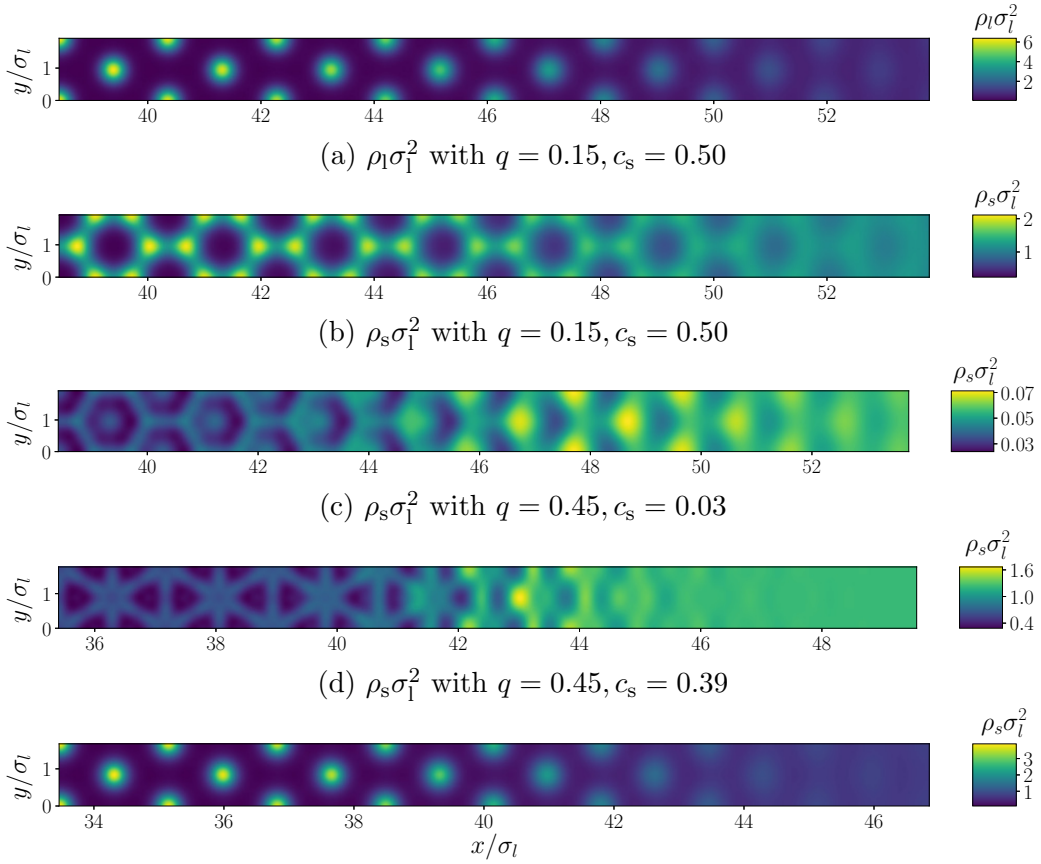

(a) $\rho_{\mathrm{l}}\sigma_{\mathrm{l}}^2$ with $q = 0.15, c_{\mathrm{s}} = 0.50$

(b) $\rho_{\mathrm{s}}\sigma_{\mathrm{l}}^2$ with $q = 0.15, c_{\mathrm{s}} = 0.50$

(c) $\rho_{\mathrm{s}}\sigma_{\mathrm{l}}^2$ with $q = 0.45, c_{\mathrm{s}} = 0.03$

(d) $\rho_{\mathrm{s}}\sigma_{\mathrm{l}}^2$ with $q = 0.45, c_{\mathrm{s}} = 0.39$

(e) $\rho_{\mathrm{s}}\sigma_{\mathrm{l}}^2$ with $q = 0.75, c_{\mathrm{s}} = 0.52$

Figure 5.8: HD mixture density profiles ρ cross crystal(left)-fluid(right) interface for $q = 0.15, 0.45$ and 0.75. Since all large disks density profiles looks similar, here we only show (a) as a representative one.

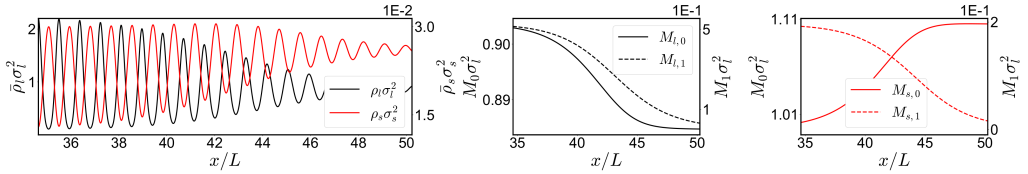

(a) $q = 0.15, c_s = 0.50$

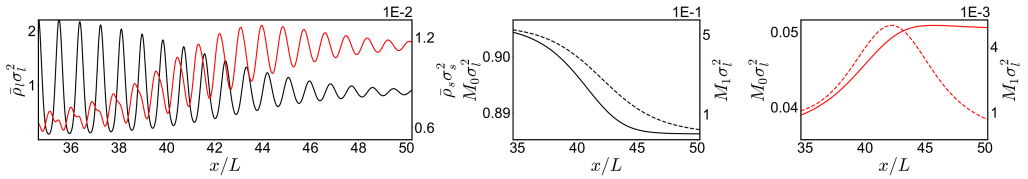

(b) $q = 0.45, c_s = 0.03$

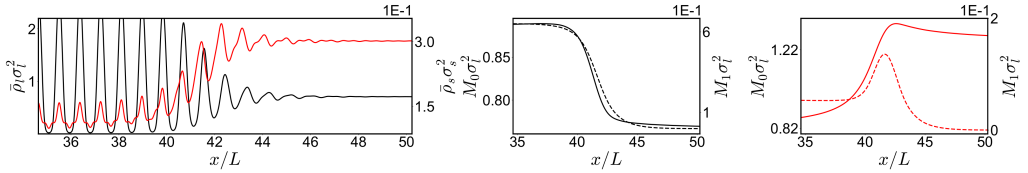

(c) $q = 0.45, c_s = 0.39$

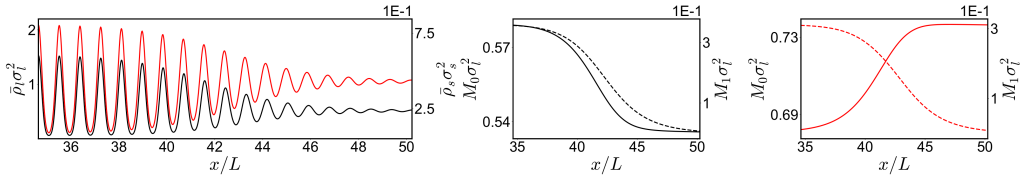

(d) $q = 0.75, c_s = 0.52$

Figure 5.9: Laterally averaged density profiles (left column), density and leading crystallinity modes of large disks (middle column) and small disks (right column) for the four interfaces of Fig. 5.8. Black lines refer to large disks, red lines to small disks. In the middle and right column, full lines are density modes M_0 and dashed lines crystallinity modes M_1.

5.5 Crystal–fluid surface tensions

5.5.1 Size ratio $q \leq 0.6$

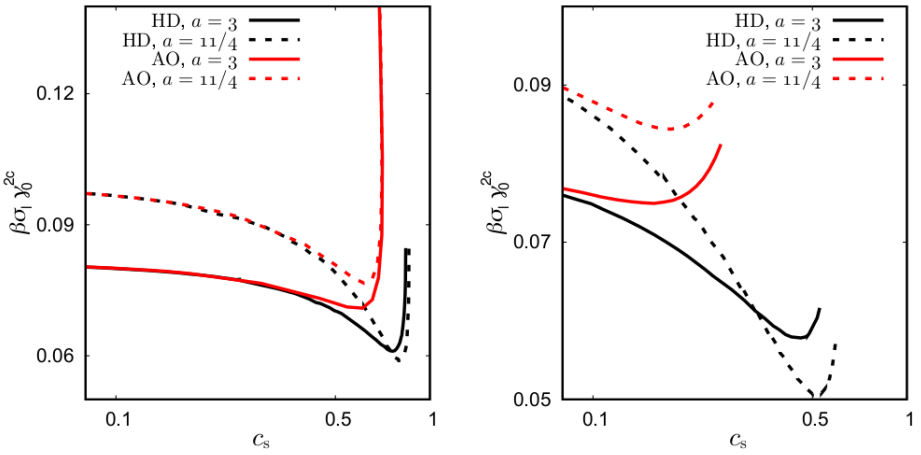

(a) $q = 0.15$ (b) $q = 0.3$

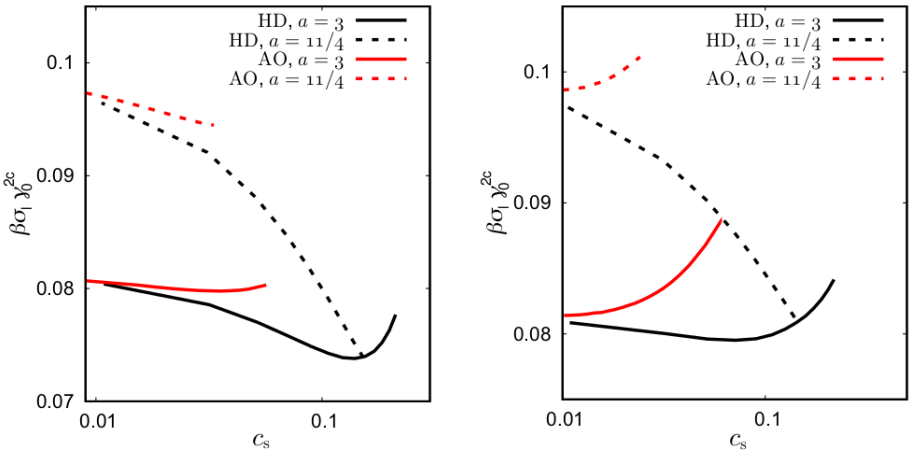

(c) $q = 0.45$ (d) $q = 0.6$

Figure 5.10: The crystal–fluid surface tension γ_0^{2c} for both the AO and the HD case and for two values of a. Note that c_s is in log scale. (a) Size ratio $q = 0.15$, (b) $q = 0.3$, (c) $q = 0.45$ and (d) $q = 0.6$.

For small to moderate size ratios of up to 0.6, we may view the small disks as depletants, at least for small concentrations c_s. In Fig. 5.10, we show the associated crystal-fluid planar surface tension γ_0^{2c} versus c_s for both AO and HD mixtures.

For $q = 0.15$ (Fig. 5.10a), we have computed the surface tension for c_s up to 1. We remind the reader of the associated phase diagrams (Fig. 5.4) which in the AO case shows the typical widening of the coexistence gap. In the HD case, the widening of the coexistence gap follows the AO case only for small c_s. It is a bit surprising that the surface tension *decreases* upon the addition of small disks, with the results for the HD mixture are close to those for the AO mixture until $c_s \sim 0.4$. In the depletion picture, the addition of small disks leads to an increasing attraction between large disks. In mean–field approximation, the increasing attraction together with an increasing coexistence gap should lead to a higher surface tension. Such an increase is seen both for the AO model and the HD case only for rather large c_s, after a minimum has been reached around $c_s \approx 0.6$ (Fig.5.10a). In the HD case, for $c_s \to 1$ we reach the monocomponent case for small disks, thus the surface tension should reach $\gamma_0^{2c}(c_s = 1) = \frac{\sigma_1}{\sigma_s}\gamma_0^{2c}(c_s = 0) = \gamma_0^{1c}/q$.

The peculiar behavior of an initially decreasing surface tension is also seen for $q = 0.3$ (Fig. 5.10b), $q = 0.45$ (Fig. 5.10c) and $q = 0.6$ (Fig. 5.10d), although the decrease becomes smaller with increasing q. With increasing size ratio, also the HD and the AO results differ more and more already for small c_s and we also note that the choice of the parameter a in the FMT functional influences the results considerably. Overall, the surface tensions are rather small on the thermal energy scale. For the monocomponent case this leads to strong interface fluctuations, as observed in Ref. [11]. Owing to the decrease in γ_0^{2c} upon the addition of small disks, we would expect that these fluctuations also become stronger.

5.5.2 Size ratio $q \geq 0.75$: HD mixtures

For $q \geq 0.75$, the phase diagram in the HD mixture is of azeotropic or spindle type (see Fig. 5.7), thus we can determine γ_0^{2c} in the whole range of concentrations from $c_s = 0$ up to 1. In Fig. 5.11, the surface tension γ_0^{2c} versus c_s is shown for four aspect rations $q \geq 0.75$ and the two values of the parameter a. Qualitatively, there is no significant dependence on a for these size ratios. As before (for small q) the initial decrease of γ_0^{2c} for small c_s is present. There is a minimum in the surface tension around $c_s = 0.5$ and it reaches the correct monocomponent value $\gamma_0^{2c}(c_s = 1) = \gamma_0^{1c}/q$.

The surface tensions can actually be well described with the following function involving one fit parameter κ:

$$\gamma_0^{2c}([\eta_{cr}], q) = \frac{\gamma_0^{1c}}{(\eta_{cr}^{1c})^2}\left((\eta_{l,cr})^2 + \frac{(\eta_{s,cr})^2}{q} + \kappa\eta_{l,cr}\,\eta_{s,cr}\right), \qquad (5.6)$$

where γ_0^{1c} and η_{cr}^{1c} on the right hand side of Eq. (5.6) are the monocomponent

surface tension and the coexistence crystal packing fraction (see Table 4.1) and $\eta_{\mathrm{l/s,cr}}$ are the coexistence crystal packing fractions of large/small HD. For the fit parameter κ we note that $\lim_{q\to 1}\kappa(q) = 2$. For $q < 0.75$, Eq. (5.6) is not valid, which may be due to the complicated transition from an azeotropic to an eutectic phase diagram (as discussed before).

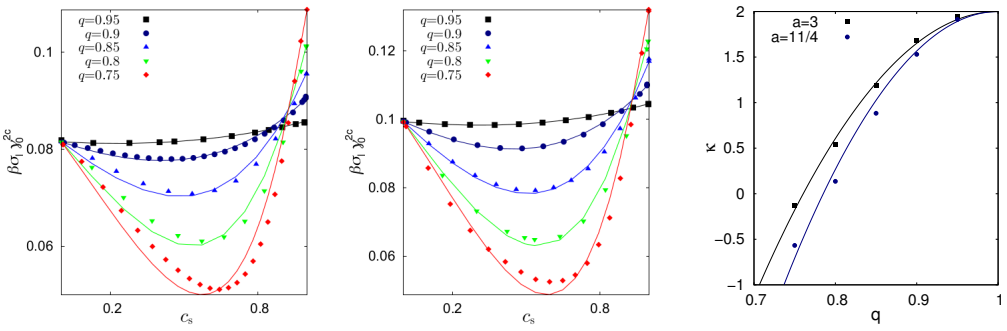

(a) $a = 3$ (b) $a = 11/4$ (c) κ

Figure 5.11: The crystal–fluid surface tension γ_0^{2c} for the HD case and for size ratios $q \geq 0.75$. The value of the parameter in the functional $a = 3$ (a) and $a = 11/4$ (b). Symbols are the numerical results and the lines are best fits to Eq. (5.6). The fit values $\kappa(q)$ are shown in (c), lines are functions $\kappa = \kappa_1(q-1)^2 + 2$ with $\kappa_1 = -34.86$ and -43.32 for $a = 3$ and $11/4$, respectively.

5.6 Liquid–vapor surface tension

For completeness, we present also results for the liquid–vapor surface tension γ_{lv} in the AO model for size ratios $q = 0.3, 0.5, 0.7$, see Fig. 5.12(a). Similar to the crystal–fluid surface tension, the numerical values for γ_{lv} are much smaller than 1 in thermal units $1/(\beta\sigma_1)$, even far away from the critical point. In Fig. 5.12(b) we show the extracted exponent α for the assumed power–law relation $\gamma_{\mathrm{lv}} \propto \Delta\eta_{\mathrm{l}}^{\alpha}$, where $\Delta\eta_{\mathrm{l}} = \eta_{\mathrm{l,liq}} - \eta_{\mathrm{l,vap}}$ is the difference between the coexistence packing fractions of large disks in the liquid and vapor phase. For mean–field models, $\alpha = 3$ close to the critical point, and this behavior is found to hold not only in the immediate vicinity of the critical point. This is similar to results from density functional studies of the 3D AO model [62].

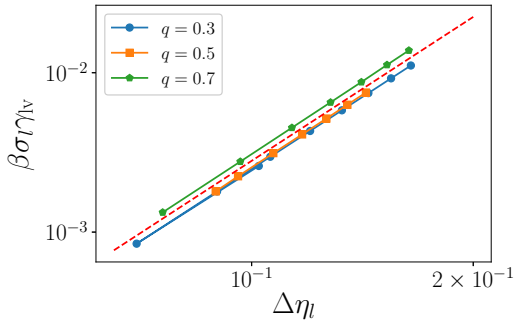

Figure 5.12: Double logarithmic plot of $\gamma_{\rm lv}$ versus $\Delta\eta_{\rm l}$. The dashed red line shows the mean–field proportionality $\gamma_{\rm lv} \propto (\Delta\eta_{\rm l})^3$. The fitting by $\gamma_{\rm lv} = b(\Delta\eta_{\rm l})^\alpha$ gives $\alpha = (3.01, 3.03, 3.05)$ for $q = (0.3, 0.5, 0.7)$.

5.7 Summary and conclusion

Using density functional theory (fundamental measure theory), we have performed an extensive study of the phase diagram and crystal–fluid surface tensions in binary hard–disk systems, both for the additive case and the non–additive (Asakura–Oosawa like) case. Since we assumed a periodic crystal, we find first–order transitions only. These correspond to the first–order fluid–hexatic transition for the one–component case and presumably to first–order fluid–crystal transitions (which become stable upon admixing a second component, see e.g. Ref. [59]). Overall, the phase diagrams are qualitatively very similar to 3D. In the AO case and for small size ratios q, the typical continuous widening of the coexistence gap is observed upon the addition of the smaller species, and for intermediate q a vapor–liquid transition becomes stable. In the additive case, the phase diagrams show the sequence spindle $\rightarrow$ azeotropic $\rightarrow$ eutectic upon lowering q from 1 to 0.6 (similar to 3D). However, the transition from azeotropic to eutectic is different from what is known in 3D hard–sphere systems (see the phase diagram in Fig. 5.6(b),(c) for $q = 0.7$).

The results for the crystal-fluid surface tensions reveal two things. Overall, their values are much smaller than 1 in thermal units $1/(\beta\sigma_1)$. For the one–component case, the resulting large thermal fluctuations of the interface have been observed experimentally [11]. Secondly, the addition of a second component leads in general to a substantial decrease in the surface tension. This holds for the AO case (for $q \lesssim 0.6$) and also for the additive case (here for the whole range of q). Complementary, dedicated simulation or experimental results on this are clearly desirable, also in view of the relevance

of the surface tension for nucleation processes, see Ref. [63] for a review on more qualitative results on 2D crystal and defect formation. The observed decrease in surface tension should lead to a considerable decrease in the time scales of crystal nucleation.

In contrast to phase diagrams, results on crystal–fluid surface tensions in binary 3D systems are scarce. For binary hard spheres with a size ratio of $q = 0.9$, results are reported in Ref. [64]. For that q, the phase diagram is azeotropic. The surface tension is found to increase monotonically with the addition of small spheres. These findings are similar to those for a 3D binary Lennard–Jones system with zero size mismatch, but a ratio of interaction strengths of 0.75 (leading to a spindle–type phase diagram) [65], but they are different from the non-monotonic behavior found here in the 2D system (see Fig. 5.11(a),(b)).

The full minimization of the FMT functionals show interesting effects for the density distributions in the crystal unit cells and of the crystal–fluid interfaces. For intermediate size ratios (examples shown for $q = 0.45$) superpositions of substitutional and alloy structures are found, and enhanced crystallinity and density of small disks is observed right at interface between crystal and fluid. Clearly, an extension of the present studies to the global stability of alloy phases and their interfaces is desirable but requires considerable more efforts.

Chapter 6

Machine learning functional

Partial results of this chapter have been published in: SciPost Phys. 6, 025 (2019) with the title "A classical density functional from machine learning and a convolutional neural network" [2]

With the steep increase of available computing power over the past years, methods of machine learning (ML) have come into the focus of research also in physics. ML is designed for finding patterns in high–dimensional data. Algorithms of ML still rely on insight and intuition how to represent and process data, but a detailed model–building (specific for the problem at hand) is not required. The optimization of data representation/processing can be viewed as a numerically intensive data fitting task which is very familiar to physicists. Therefore it appears also natural to apply ML to the problem of functional construction in DFT. In the past years, such ideas have been driven by the quantum DFT community. Refs. [16, 17] address the construction of a ML functional for the kinetic energy functional $T[n]$ in one dimension (1D). Although successful in obtaining energy values, certain limitations when going to three dimensions (3D) have led the authors of Ref. [18] to apply ML directly to the functional map between the external potential and the electron density. Although the approach appears to be quite promising in terms of possible accuracy, it amounts to hiding the energy functional in a "ML black box", which might appear less appealing to theorists.

Certainly, in the case of a "ML black box" functional one must be careful in choosing training data sets in relation to the applications one has in mind. For classical DFT, training data sets would be created most naturally by Monte Carlo (MC) or Molecular Dynamics (MD) simulations. To keep numerical efforts down, training sets should be created using small sets of parameters (chemical potential, temperature, external potentials) with good

statistics. For a classical "ML black box" functional, the highly nonlinear packing effects would probably necessitate to train the ML functional with densities at least as high as in the application cases. On the other hand, packing is well described by the existing hard–body functionals and one may doubt whether the currently existing ML schemes can improve those. Therefore, for a fluid with repulsive cores it makes sense to maintain the splitting of the excess free energy functional into a hard–core part and a part describing the soft parts of the potential.

In this chapter, we consider a Lennard–Jones (–like) (LJ) pair potential in one dimension:

$$U_{\mathrm{LJ}}(x) = \begin{cases} \infty & \text{if} \quad x < \sigma \\ 4\epsilon \left[\left(\frac{\sigma}{x}\right)^{12} - \left(\frac{\sigma}{x}\right)^{6} \right] & \text{if} \quad \sigma < x < 16\sigma \\ 0 & \text{otherwise} \end{cases}$$

with x the distance between particle centers, σ the diameter of the particles and ϵ the strength of interaction. In the following we set $\sigma = 1$.

The exact functional of LJ model in 1D is unknown [66]. Therefore, training data sets have to be obtained by simulations (similar to desired extensions to 3D). The ML functional will be constructed using weighted densities which are convolutions of the density with weight functions to be determined by ML fitting. Our ML fitting is similar to a basic generative convolutional neural network which is used in image processing.

6.1 Basic ideas and improved mean–field functionals

Here we consider a simple mean–field based machine learning functional and apply it on the LJ fluid. In the following we set $\beta = \lambda = 1$ for simplicity. In equilibrium, as described in Sec.2.4, the density profile satisfies

$$\rho^{\mathrm{eq}} = \exp\left(\mu - \left. \frac{\delta \mathcal{F}^{\mathrm{ex}}}{\delta \rho} \right|_{\rho=\rho^{\mathrm{eq}}} - V^{\mathrm{ext}} \right). \tag{6.1}$$

To justify the quality of a certain $\mathcal{F}^{\mathrm{ex}}$, we solve Eq. (6.1) by different sets of μ, V^{ext} and ϵ (inverse temperature), and then compare ρ^{eq} with ρ^{MC} (grand canonical simulation data for the the density profile).

However, as one may ask, is it possible to directly learn $\mathcal{F}^{\mathrm{ex}}$ by ρ^{MC}? To

facilitate such an idea, we define a ML output density as

$$\rho^{\mathrm{ML}}(x) = \exp\left(\mu - \left.\frac{\delta\mathcal{F}^{\mathrm{ex,ML}}}{\delta\rho}\right|_{\rho=\rho^{\mathrm{MC}}} - V^{\mathrm{ext}}\right), \tag{6.2}$$

with ρ^{MC} the simulation result of equilibrium density profiles. To measure the difference between ρ^{MC} and ρ^{ML}, we define the loss function

$$L = \sum_{k}^{M} \int \left(\rho_k^{\mathrm{MC}}(x) - \rho_k^{\mathrm{ML}}(x)\right)^2 dx, \tag{6.3}$$

where ρ_k^{MC} is the k–th training sample (density distribution from simulation), ρ_k^{ML} is the corresponding ML output by Eq.(6.2), and M is number of training sample. If we could give $\mathcal{F}^{\mathrm{ex,ML}}$ a certain ansatz, we should be able to find an approximation of $\mathcal{F}^{\mathrm{ex,ML}}$ by minimizing L. The idea is actually very similar to a generative network, such as an autoencoder [67]. The $\rho^{\mathrm{MC}}/\rho^{\mathrm{ML}}$ is the input/output, $\mathcal{F}^{\mathrm{ex,ML}}$ is an encoder, and Eq. (6.1) is a decoder.

But what form of $\mathcal{F}^{\mathrm{ex,ML}}$ should be used? In most cases, the excess free energy functional $\mathcal{F}^{\mathrm{ex}}$ of LJ is split into $\mathcal{F}^{\mathrm{HR}}$ and $\mathcal{F}^{\mathrm{att}}$, such as $\mathcal{F}^{\mathrm{ex}} = \mathcal{F}^{\mathrm{HR}} + \mathcal{F}^{\mathrm{att}}$ with $\mathcal{F}^{\mathrm{HR}}/\mathcal{F}^{\mathrm{att}}$ denoting excess free energy functional from HR/attractive potential, where $\mathcal{F}^{\mathrm{att}}$ is approximated by the mean–field (MF) approximation,

$$\mathcal{F}^{\mathrm{MF}} = \frac{1}{2}\int dx\, \rho(x) \int dx'\, \rho(x') U_{\mathrm{att}}(|x - x'|). \tag{6.4}$$

with

$$U_{\mathrm{att}}(x) = \begin{cases} 0 & \text{if} \quad x < \sigma \\ U_{\mathrm{LJ}}(x) & \text{otherwise.} \end{cases}$$

Analogously, we consider $\mathcal{F}^{\mathrm{ex,ML}}[\rho] = \mathcal{F}^{\mathrm{HR}} + \mathcal{F}^{\mathrm{ex,ML}}_{\mathrm{att}}$ with

$$\mathcal{F}^{\mathrm{ex,ML}}_{\mathrm{att}}[\rho] = \epsilon \int dx\, \rho(x) n(x), \tag{6.5}$$

and the weighted density $n(x) = \int dx'\, \rho(x')\omega(x - x')$. The ω is the convolution kernel/weight function that needs to be trained. This is the weighted–density form of the RPA mean–field approximation in Eq. (6.4). Thus, the kernel ω should somehow correspond to $U_{\mathrm{att}}/(2\epsilon)$. To minimize L, we use the gradient decent [68], where ω is updated by [1]

$$\omega^{\mathrm{new}}(x) = \omega^{\mathrm{old}}(x) - \alpha \left.\frac{\partial L}{\partial \omega}\right|_{\omega=\omega^{\mathrm{old}}} \tag{6.6}$$

[1] rigorously speaking, since L is a functional of ω, it should be $\frac{\delta L}{\delta \omega}$.

with α the learning rate. The gradient descent is based on Taylor expansion as $L(\omega+\epsilon) \simeq L(\omega) + \epsilon \frac{\partial L}{\partial \omega}$ for small ϵ. If one sets $\epsilon = -\alpha \frac{\partial L}{\partial \omega}$, then $L(\omega+\epsilon) \simeq L(\omega) - \alpha \left(\frac{\partial L}{\partial \omega}\right)^2 < L(\omega)$ for a small and positive α. As one can see, the gradient descent stops when $\frac{\partial L}{\partial \omega} = 0$, so it will find a local minimum. Furthermore, the term $\frac{\partial L}{\partial \omega}$ with the symmetry assumption $\omega(x) = \omega(-x)$ can be written as

$$\frac{\partial L}{\partial \omega\left(x'\right)} = -4 \left\{ \sum_k \int dx \, \left(\rho_k^{\mathrm{MC}}\left(x\right) - \rho_k^{\mathrm{ML}}\left(x\right)\right) \rho_k^{\mathrm{ML}}\left(x\right) \epsilon_k \rho_k^{\mathrm{MC}}\left(x + x'\right) \right\}. \quad (6.7)$$

For a more complex ansatz (see next section), this term will be too cumbersome to determine by hand. Fortunately in the modern ML programming tools, such as `Tensorflow`[69] and `PyTorch`[70], it is automatically handled by back–propagation. For the details of machine learning, we refer to Ref [68] as an overview, for interested readers.

6.2 Result and conclusion

To train ω, we prepare 1115 density profiles by grand canonical simulation. The V^{ext} is a hard–wall slit of width 32 σ with 3 additional Gaussian potentials of random strength/width and location inside the slit (see Fig. 6.1a); ϵ and μ are randomly in the range of 0.5...1.5 and $\ln 0.5 ... \ln 2.0$.

In Fig. 6.1, we shows the final result of the kernel ω after training and the loss functional (Eq. (6.3)) versus iterations. The tail of ω is close to $U_{\mathrm{att}}/(2\epsilon)$ as expected, and it extends somewhat into the hard–core region. Furthermore we show the pressure versus the bulk density (equation of state, eos), and the density profile on a hard wall in Fig. 6.2.

As shown in Fig. 6.2, the results by $\mathcal{F}^{\mathrm{ex,ML}}$ is better then the naive mean–field approximation. The contribution to $\mathcal{F}^{\mathrm{ex}}[\rho]$ from attractive interactions outside the hard core is treated by mean–field concepts in various guises [27, 71, 72, 73, 74]. With the $\mathcal{F}^{\mathrm{ex,ML}}$ introduced in this section, we obtain ω and thus $\mathcal{F}^{\mathrm{ex}}$ directly from ρ^{MC}. However, even with the improvement, it is still a mean–field type functional. Due to the simple *ansatz*, the improvement is unsatisfactory; moreover, not all particle–particle potentials may allow for the splitting into a well–understood reference part and a remainder to be learned by ML, such as $\mathcal{F}^{\mathrm{HR}}$ in this case. In the next chapter, we introduce a more flexible ML architecture, which is capable of giving $\mathcal{F}^{\mathrm{ex,ML}}$ beyond mean–field type functional and even forego $\mathcal{F}^{\mathrm{HR}}$.

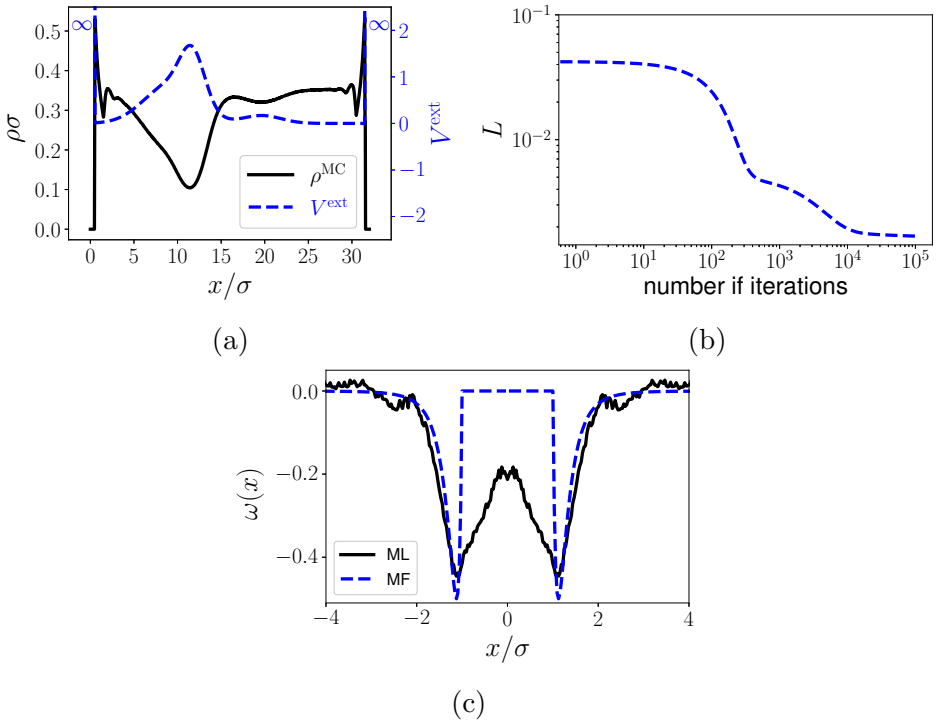

(a) (b)

(c)

Figure 6.1: (a) An example of V^{ext} and ρ^{MC} with $\mu = \ln(1.40)$ and $\epsilon = 1.24$, (b) loss versus iterations, and (c) RPA–like mean–field approximation. In (a), the black solid line is ρ^{MC} corresponding to the left y–axis and blue dashed line is V^{ext} corresponding to the right y–axis. In (c), the black solid line is the ML–optimized $\omega(x)$, and for comparison $U_{\mathrm{att}}(x)/(2\epsilon)$ is shown by the blue dashed line.

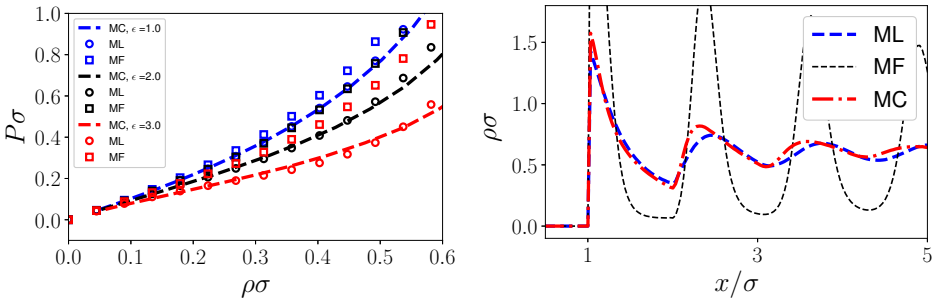

(a) (b)

Figure 6.2: (a) equation of sate, and (b) $\rho(x)$ on a hard–wall potential for $\epsilon = 1.5$ and $\mu = \ln 1.5$. The ML and MF density profiles are obtained by iteratively solving Eq. (6.1) with the density profiles initialized by a constant value.

Chapter 7

Functional equation learner

Partial results of this chapter have been published in: J. Chem. Phys. 152, 021102 (2020) with the title "Analytical classical density functionals from an equation learning network"[75]

In Chapter 6, we introduce a mean–field–like machine learning (ML) functional. Despite the improvement comparing to the naive mean–field approximation, the form of the functional is limited.

From a thoery point of view, the excess functionals derived from Fundamental Measure Theory (FMT) [8] have a high degree of accuracy [3, 8, 34] for hard spheres and hard anisotropic particles [76, 77, 78]. However, the contribution to $\mathcal{F}^{\mathrm{ex}}[\rho]$ from attractive interactions outside the hard core is treated by mean–field concepts in various guises (random phase approximation (RPA) [71], functional expansions [27, 72], Wertheim theory for patchy attractions [73, 74] etc.) but a qualitatively new and successful *ansatz*, such as FMT hard–body–treatment, is missing.

Thus, to extend the flexibility of the ML functional and success of FMT, the network we propose, *Functional Equation Learner* (FEQL), is an L–layered feed–forward network with computational units specifically designed for constructing the free energy functional (see Fig. 7.1).

The first layer consists of convolution kernels which compute the weighted densities n_i with the convolution kernel ω_i ($i = 1...n_{\mathrm{w}}$) by

$$n_i(x) = \rho \otimes \omega_i = \int dx' \, \rho(x')\omega_i(x - x') \, , \tag{7.1}$$

and some of the weighted densities are multiplied by ϵ in the case of the LJ fluid. Using weighted densities instead of the particle density is inspired by the exact HR functional [34] and fundamental measure theory [4, 8]. The

layer 2 is a linear, all–to–all mapping of the vector (of functions) $n = \{n_i(x)\}$ to the vector

$$z^{(l=1)} = W^{(1)} n \tag{7.2}$$

at level $l = 1$. The layers $3...L-4$ are a sequence of nonlinear and linear transformations.

The non-linear transformation at level l contains u unary units f_I and v binary units g_J and maps $z^{(l)}(x)$ ($u + 2v$–dimensional) to the layer output $y^{(l)}$ ($u + v$–dimensional) as:

$$\begin{aligned} y^{(l)} := \quad & \left(f_1\left(z_1^{(l)}\right), f_2\left(z_2^{(l)}\right) ... f_u\left(z_u^{(l)}\right),\right. \\ & \left. g_1\left(z_{u+1}^{(l)}, z_{u+2}^{(l)}\right) ... g_v\left(z_{u+2v-1}^{(l)}, z_{u+2v}^{(l)}\right)\right). \end{aligned} \tag{7.3}$$

The unary units, $f_1, ..., f_u$ receive the respective component, $z_1, ..., z_u$ as inputs, and each unit is one of the following base functions indexed by $I \in 0, 1, 2$:

$$f_I(z_i) := \begin{cases} z_i & \text{if} \quad I = 0 \\ \exp(z_i) - 1 & \text{if} \quad I = 1 \\ \ln(z_i + 1) & \text{if} \quad I = 2 \end{cases}$$

The binary units, $g_1, ..., g_v$ receive the remaining component, $z_{u+1}, ..., z_{u+2v}$, as input in pairs of two, and each unit may be multiplication or division indexed by $J \in 0, 1$:

$$g_J(z_i, z_{i+1}) := \begin{cases} z_i \times z_{i+1} & \text{if} \quad J = 0 \\ z_i \div (z_{i+1} + 1) & \text{if} \quad J = 1 \end{cases}$$

Note that $f_I(0) = g_J(0, z) = 0$. One may worry about divergences in division and logarithm when $z \to -1$. In the beginning of the training procedure, all parameters and convolution kernel are initialized by small numbers and thus z, f_I and g_J are close to zero. If z is too close to -1, the loss will change drastically; thus the network will intrinsically handle this issue. As mentioned in Ref. [22], one could use modified division and logarithm functions and add extra penalties. However, it turns out not to be required here.

The linear transformation from level l to $l+1$ maps the $(u+v)$–dimensional input $y^{(l)}$ to the $(u+2v)$–dimensional intermediate representation $z^{(l+1)}$ given by

$$z^{(l+1)} = W^{(l+1)} y^{(l)}. \tag{7.4}$$

Thus, the n_{w} convolution kernels $\omega(x)$ in the first layer and the matrices $W^{(l)}$ are free parameters that are learned during training.

The machine-learned free energy density $\mathfrak{f}^{\mathrm{ex,ML}}$ is a summation of the output of layer $L-4$ (see layer 5 in Fig. 7.1), the functional derivative $\frac{\delta\mathcal{F}^{\mathrm{ex,ML}}}{\delta\rho} = \sum_i \frac{\partial\mathfrak{f}^{\mathrm{ex,ML}}}{\partial n_i} \oplus \omega_i$ (with $\mathcal{F}^{\mathrm{ex,ML}} = \int dx\, \mathfrak{f}^{\mathrm{ex,ML}}(n)$ and $\oplus$ denoting cross–correlation) is used in the final, generative step:

$$\rho_i^{\mathrm{ML}}(x) = \exp\left(\mu_i^{\mathrm{ML}} - \left.\frac{\delta\mathcal{F}^{\mathrm{ex,ML}}}{\delta\rho}\right|_{\rho=\rho_i^{\mathrm{eq}}} - V_i^{\mathrm{ext}}\right), \tag{7.5}$$

where μ_i^{ML} is to facilitate convergence (see Sec. 7.3.4 for more details), subscript i is i–th input data, and we set $\beta = \lambda = 1$ for simplicity (see Eq.(2.27)). Be aware of the difference between convolution and cross-correlation in the FEQL (see Appendix B for details).

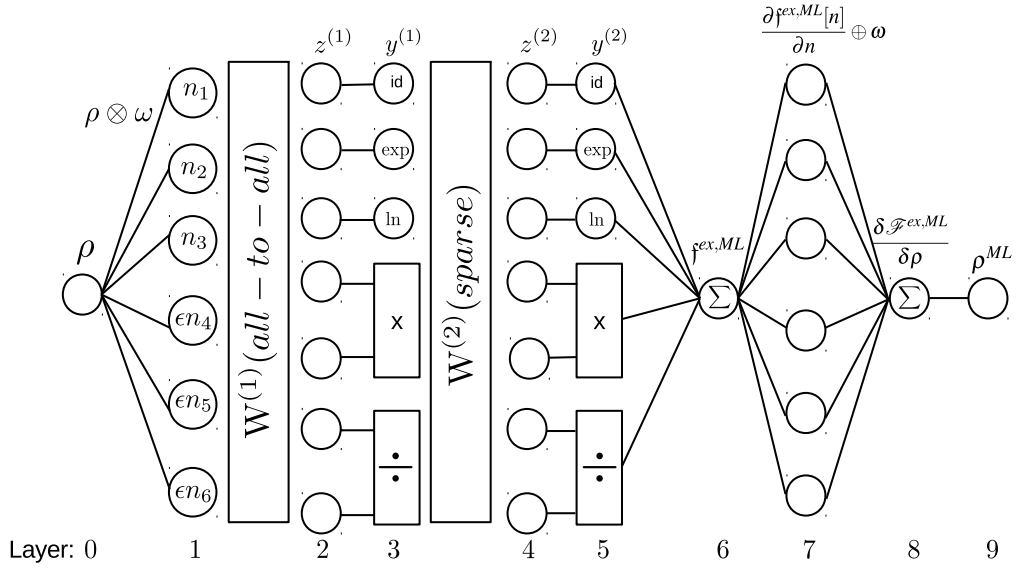

Figure 7.1: Network architecture of the proposed FEQL for 10 layers ($L = 9$) and one neuron per type ($u = 3$, $v = 2$) and 6 convolution (weighting) kernels ($n_{\mathrm{w}} = 6$). ϵ is the coupling strength (equivalent to inverse temperature) in the LJ potential.

7.1 Physical constraints

Since $\mathcal{F}^{\mathrm{ex,ML}}$ approximates $\mathcal{F}^{\mathrm{ex}}$, we must consider two physical constraints: (i) $\mathcal{F}^{\mathrm{ex,ML}}(\rho = 0) = 0$ and (ii) $\frac{\delta \mathcal{F}^{\mathrm{ex,ML}}}{\delta \rho}\Big|_{\rho=0} = 0$. To enforce (i), we choose the linear mapping without bias and $f(0) = g(0, z) = 0$ in the non–linear mapping. Condition (ii) can be enforced by setting appropriate parameters in the matrix $W^{(l)}$ of the final level to zero. This requires to determine the analytic form of $\frac{\partial \mathfrak{f}^{\mathrm{ex,ML}}}{\partial n_i}\Big|_{\rho=0}$ to identity those parameters. For example, for a FEQL with $n_{\mathrm{w}} = 2$, 2 levels and (1,0,0,1,0) node for (identity, exponential, logarithm, multiplication and division),

$$\begin{aligned}\mathfrak{f}^{\mathrm{ex,ML}} =& a_2L_0(a_1L_0n_0 + a_1L_1n_1) + a_2L_1(a_1L_2n_0 + a_1L_3n_1)(a_1L_4n_0 + a_1L_5n_1)+ \\ & (a_2L_2(a_1L_0n_0 + a_1L_1n_1) + a_2L_3(a_1L_2n_0 + a_1L_3n_1)(a_1L_4n_0 + a_1L_5n_1)) \\ & (a_2L_4(a_1L_0n_0 + a_1L_1n_1) + a_2L_5(a_1L_2n_0 + a_1L_3n_1)(a_1L_4n_0 + a_1L_5n_1))\end{aligned} \tag{7.6}$$

with a_xL_y the y–th parameter in $W^{(x)}$. Then we calculate $\frac{\partial \mathfrak{f}^{\mathrm{ex,ML}}}{\partial n_i}\Big|_{\rho=0}$, such as $\frac{\partial \mathfrak{f}^{\mathrm{ex,ML}}}{\partial n_0}\Big|_{\rho=0} = a_1L_0\, a_2L_0$, and $\frac{\partial \mathfrak{f}^{\mathrm{ex,ML}}}{\partial n_1}\Big|_{\rho=0} = a_1L_1\, a_2L_0$. Thus we set $a_2L_0 = 0$ in order to keep $\frac{\delta \mathcal{F}^{\mathrm{ex,ML}}}{\delta \rho}\Big|_{\rho=0} = 0$; this is the reason in Fig. 7.1 the $W^{(2)}$ is labeled as sparse.

7.2 Network training

To obtain training data for ρ^{eq}, grand canonical simulations are used in the case of LJ fluid; for the HR fluid, Eq. (2.27) is directly solved, since the exact functional is known.

FEQL is fully differentiable in its free parameters $\theta = [W, \omega]$ and can thus be trained using back–propagation. We adopt the following loss function

$$\begin{aligned}L &= \frac{1}{N}\sum_{i=1}^{N}\left(\alpha_1 \int |\rho_i^{\mathrm{eq}} - \rho_i^{\mathrm{ML}}|\, d\,x + \alpha_2 |\mu_i^{\mathrm{eq}} - \mu_i^{\mathrm{ML}}|\right) \\ &\quad + \lambda_1 \sum_i \int dx\, |\omega_i| + \lambda_2 \sum_{l,\beta\gamma} |W^{(l)}_{\beta\gamma}|,\end{aligned} \tag{7.7}$$

with $\alpha_1 = 0.9$ and $\alpha_2 = 0.1$. These values have been determined empirically and the exact choice is not critical. For training we choose Adam [79] with

mini-batches:

$$\theta_{t+1} = \theta_t + \text{Adam}\left(\frac{\partial L\left(D\left(t\right)\right)}{\partial \theta}, \alpha\right) \tag{7.8}$$

with α the stepsize parameter (learning rate) and $D(t)$ the data in the current mini-batch. The choice of Adam is not critical and standard stochastic gradient descent also accomplished the task.

Following Sahoo *et al.* [22], we adopt a three–step training procedure. At the beginning, we use no regularization ($\lambda_1 = \lambda_2 = 0$), such that parameters can vary freely and reach reasonable starting points. In step 2, we switch on the regularization by setting λ_1 and λ_2 to positive finite values to sparsify the network for obtaining a simpler functional. In step 3, we clamp small parameters with $|W^{(l)}_{\beta\gamma}| < w_{\text{th}}$ to zero. In this way we keep the sparsity introduced by the lasso [80] training in step 2, but make sure unbiased parameter values are attained. In this paper we choose $\alpha = 10^{-2}$ or 10^{-3}, $\lambda_1 = 10^{-7}$ and $w_{\text{th}} = 0.05$.

7.3 Results

To exam the ability of FEQL, we investigate the HR pair potential:

$$U_{\text{HR}}(x) = \begin{cases} \infty & \text{if} \quad x < \sigma \\ 0 & \text{otherwise} \end{cases}$$

as well as the LJ(–like) potential:

$$U_{\text{LJ}}(x) = \begin{cases} \infty & \text{if} \quad x < \sigma \\ 4\epsilon\left[\left(\frac{\sigma}{x}\right)^{12} - \left(\frac{\sigma}{x}\right)^{6}\right] & \text{if} \quad \sigma < x < 16\sigma \\ 0 & \text{otherwise} \end{cases}$$

in one dimension with x the distance between particle centers, σ the diameter of the particles and ϵ the strength of interaction. In the following we set $\sigma = 1$.

7.3.1 Hard rods

The hard–rod (HR) fluid is one of a few systems that $\mathcal{F}^{\text{ex}}$ is exactly known. The exact equation of state (eos) is given by the pressure $P(\rho) = \frac{\rho}{1-\rho}$ and the exact analytic form of $\mathcal{F}^{\text{HR}}$ (Percus functional) is described in Sec. 3.3.3.

The parameter of $\mathcal{F}^{\text{ex,ML}}$ are trained using 1024 density profiles in a hard wall slit of width 32 σ with 3 additional Gaussian potentials of random

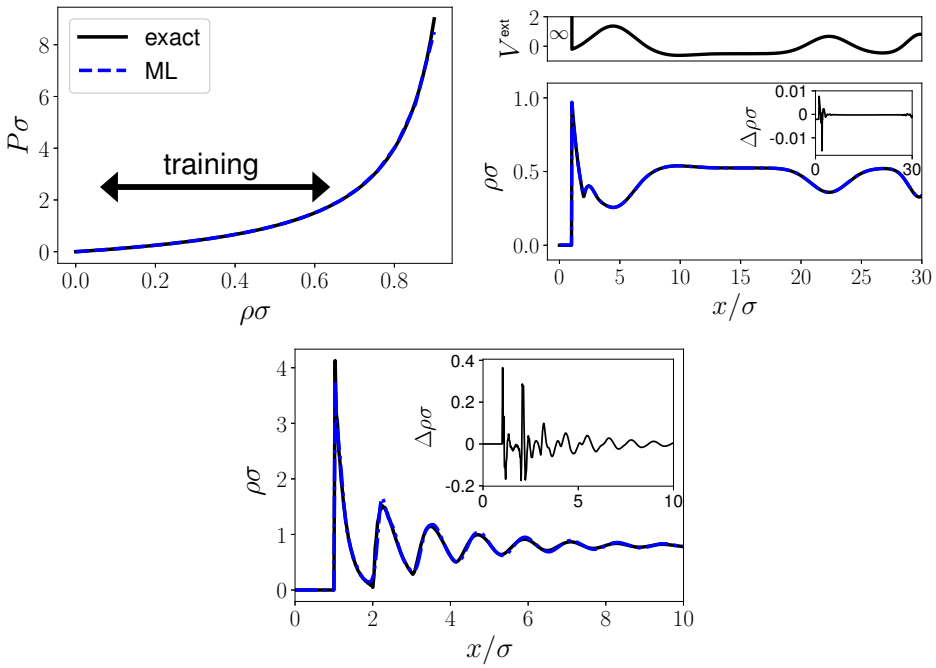

Figure 7.2: FEQL results for hard rods. Dark solid lines are exact solutions from $\mathcal{F}^{\rm HR}$ and blue dashed lines are ML results. (a) $P(\rho)$. (b) density profile for $\rho_0 = 0.49$ inside the training region but $V^{\rm ext}$ not in the training data. (c) density profile at hard wall for $\rho_0 = 0.80$ outside the training region. Insets in (b) and (c) show $\Delta\rho = \rho^{\rm exact} - \rho^{\rm ML}$.

strength/width (see Fig. 6.1a for an example) and location inside the slit and with a range of training reservoir densities $\rho_0 = 0.2...0.55$. We choose $n_{\rm w} = 3$ and (1,1,1,3,1) nodes for (identity, exponential, logarithm, multiplication and division) with $L = 9$ (10 layers, see Fig. 7.1) and $\lambda_2 = 8 \cdot 10^{-5}$ in Eq. (7.7) (results for different λ_2 and arguments for an optimal choice are discussed below). The explicit functional and kernels are shown in Sec. 7.3.3 below.

$\mathcal{F}^{\rm ex,ML}$ is not of the form of the Percus functional, since the convolution kernels of the latter are Dirac delta and Heaviside step functions, which are are hard to be captured by our network.

In Fig.7.2, we show the eos, a density profile inside the thermodynamic training region but not in the training data ($\rho_0 = 0.49$) and a density profile outside the training region ($\rho_0 = 0.80$). The FEQL recovers the almost exact result inside the training region and also performs quite well even outside the training region. The ML density profiles are initialized by $\rho = 0.5$ and then iteratively solved using Eq. (2.27) with $\mathcal{F}^{\rm ex} = \mathcal{F}^{\rm ex,ML}$.

The virial expansion

$$P^{\mathrm{ML}}(\rho) \simeq \rho + 1.03\rho^2 + 0.71\rho^3 + O\left(\rho^4\right) \tag{7.9}$$

of the ML eos shows moderate deviations compared to the exact one ($\frac{\rho}{1-\rho} = \rho + \rho^2 + \rho^3 ...$).

One sees that inaccuracies in these coefficients do not necessarily lead to a poor eos. Despite inaccurate coefficients, the higher order terms in the learned eos combine appropriately to give a good representation of the exact eos. This is understandable since no explicit information about virial coefficients is incorporated into the loss function, thus the learning procedure has little incentive to find the correct coefficients.

Optimization for hard rod

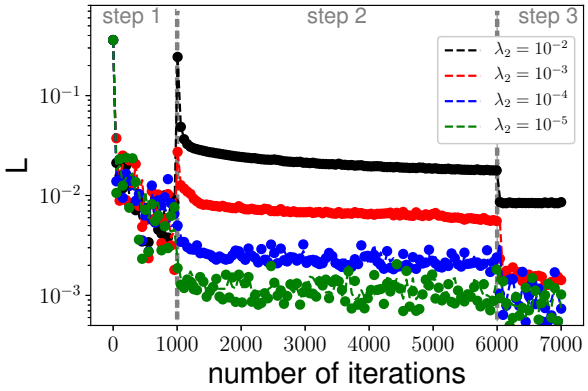

Figure 7.3: Loss as a function of number of iterations for 4 different values of λ_2. Dashed lines are validation loss and solid circles are training loss.

In Eq. (7.7), the third term with coefficient λ_2 is used as a substitute for the number of nonzero entries in the matrices $W^{(l)}$, which is not differentiable directly. Nevertheless, minimizing the absolute norm tends to produce sparse solutions, see also Lasso regression [80], and thus favors simpler functionals. Before training, we prepared 1024 density profiles with a range of reservoir densities $\rho_0 = 0.2...0.55$, and randomly divided them into 921 density profiles as the training set and 103 as the validating set. The training procedure only uses the training set for updating trainable parameters and evaluates the value of the loss on the training set and on the validating set (called training loss and validation loss) at the end of each iteration [68]. Additionally, we also

prepare 256 density profiles with a range of reservoir densities $\rho_0 = 0.6...0.8$, outside the training region, as a measurement for extrapolative capabilities.

Then, as described in before (Sec. 7.2), we have used a three–step training procedure. In Fig. 7.3 we show the evolution of the training and validation loss throughout the training for 4 different values of λ_2. For the higher values of λ_2 (10^{-2} and 10^{-3}) there is a marked increase of L at the beginning of step 2. For $\lambda = 10^{-4}$ the beginning of step 2 is not marked with an increase of L and then L further decreases.

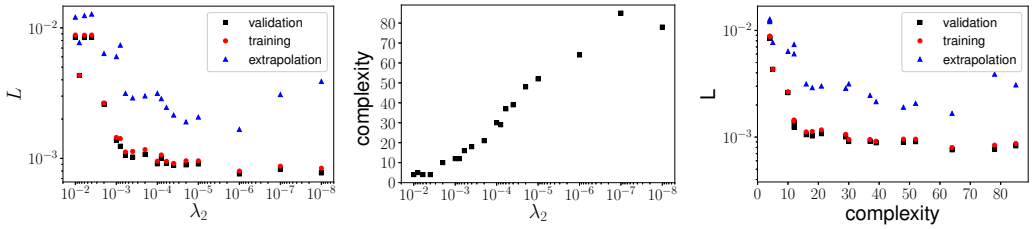

(a) Final loss versus λ_2. (b) complexity versus λ_2. (c) complexity versus loss.

Figure 7.4: The interdependence of loss, complexity and λ_2.

This is further confirmed in Fig. 7.4a, which shows the final value of L from the training, validating, and extrapolating set as a function of λ_2. The loss shows underfitting for $\lambda_2 > 10^{-3}$ and overfitting for $\lambda_2 < 10^{-7}$. Near–optimal choices are $10^{-6} < \lambda_2 < 10^{-4}$. The complexities (the number of nonzero entries in W) increase with decreasing of λ_2 (Fig. 7.4b). For a broad range of complexities, the loss is almost constant (Fig. 7.4c).

7.3.2 Lennard–Jones

Here, 1115 training distributions are generated with random ϵ and μ in the range of $0.5...1.5$ and $\ln 0.5... \ln 2$, respectively, with V^{ext} prescribed as in the hard–rod case (see Fig. 6.1a for an example). The training data are obtained by grand canonical Monte Carlo (GCMC) simulation.

Splitting between repulsions and attractions

Following liquid state theory [2] and similar in spirit to Chap. 6, we split $\mathcal{F}^{\text{ex}}$ into a contribution from repulsions and one from attractions as follows:

$$\mathcal{F}^{\text{ex,ML}}([\rho];\epsilon) = \mathcal{F}^{\text{HR}}([\rho]) + \epsilon\mathcal{F}^{\text{ex,ML}}_{\text{att}}([\rho];\epsilon), \tag{7.10}$$

where the factor ϵ in front of the $\mathcal{F}^{\text{ex,ML}}_{\text{att}}$ makes sure $\mathcal{F}^{\text{ex,ML}}(\epsilon \to 0) = \mathcal{F}^{\text{HR}}$, and $\mathcal{F}^{\text{ex,ML}}_{\text{att}}$ is to be learned by the network. In Fig. 7.1, the output from the layer

6 is $\mathcal{F}^{\mathrm{ex,ML}}_{\mathrm{att}}$; we multiply the output from the layer 8 by ϵ, add contribution from $\mathcal{F}^{\mathrm{HR}}$, and then feed it to layer 9. In the first layer, we choose $n_{\mathrm{w}} = 4$, 1 kernel multiplied by ϵ and another 3 without this factor (see Fig. 7.1), and (1,1,1,2,1) nodes for (identity, exponential, logarithm, multiplication and division). The training parameter $\lambda_2 = 5 \cdot 10^{-5}$ in Eq. (7.7). Results are shown below in Fig. 7.5. The explicit functional and kernels are shown in Sec. 7.3.3. The findings are similar to the HR case with a very good match to simulation data for the eos and test distributions inside and outside the thermodynamic training region. For a 1D system with hard–core repulsive and finite–ranged attractive pair potential, the pressure must be monotonically increasing for arbitrary low temperature (high ϵ), and thus there is no gas–liquid transition [81]. The corresponding ML pressure shows no van der Waals (vdW) loop for attractions strengths up to $\epsilon = 4.1$.

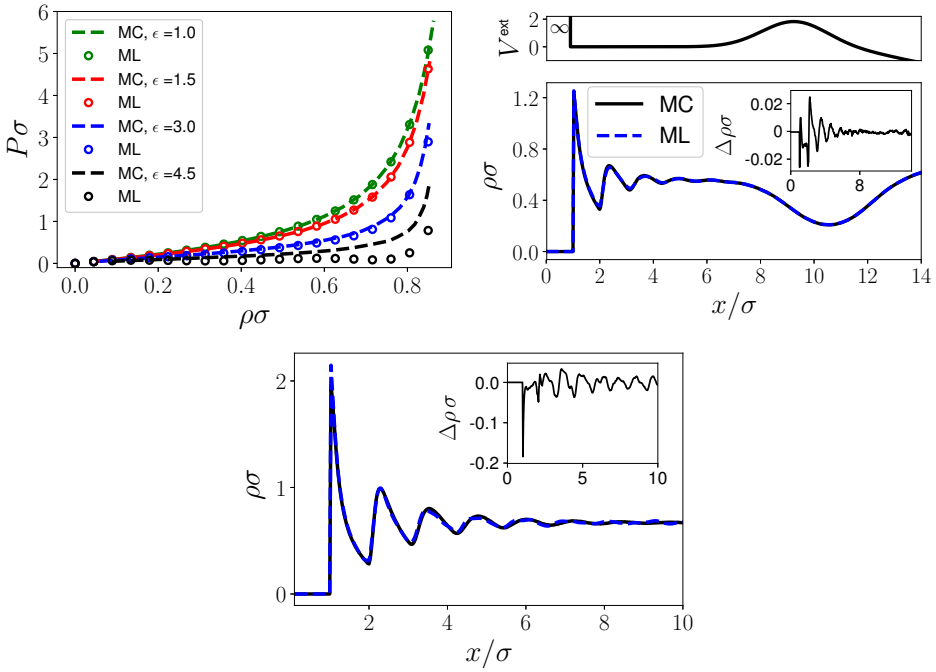

Figure 7.5: FEQL results for LJ fluid with functional splitting. (a) eos $P(\rho)$. (b) density profile for $\epsilon = 1.30$, $\mu = \ln(1.27)$ inside the training region but V^{ext} not in the training data. (c) density profile at a hard wall for $\epsilon = 1.7$, $\mu = \ln(1.7)$, outside the training region. Dark solid lines are simulation profiles and blue dashed lines are ML results. Insets in (b) and (c) show $\Delta\rho = \rho^{\mathrm{MC}} - \rho^{\mathrm{ML}}$.

No splitting

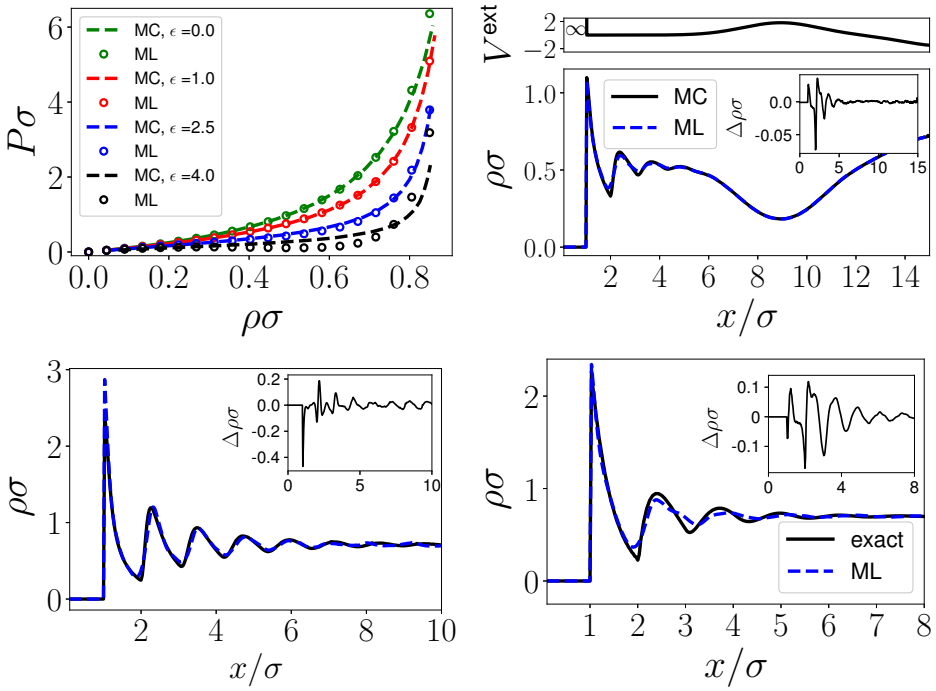

Figure 7.6: FEQL results for LJ fluid (no splitting). (a) eos $P(\rho)$. (b) density profile for $\epsilon = 1.25$, $\mu = \ln(1.15)$ inside the training region but V^{ext} not in the training data. (c,d) density profile at a hard wall for $\epsilon = 1.9$, $\mu = \ln(1.9)$ (c) and $\epsilon = 0$, $\rho_0 = 0.7$ (HR limit, (d)). Dark solid lines are simulation profiles and blue dashed lines are ML results. Insets in (b) and (c) show $\Delta\rho = \rho^{\text{MC}} - \rho^{\text{ML}}$ and in (d) $\Delta\rho = \rho^{\text{exact}} - \rho^{\text{ML}}$.

As a further test of the capability of FEQL, we forego the splitting of the functional such that $\mathcal{F}^{\text{ex}} = \mathcal{F}^{\text{ex,ML}}$. In the first layer, we choose $n_{\text{w}} = 6$, 3 kernels multiplied with ϵ and another 3 without this factor (see Fig. 7.1), and (1,1,1,3,1) nodes for (identity, exponential, logarithm, multiplication and division). The training parameter λ_2 is set to $5{\cdot}10^{-5}$ in Eq. (7.7). The explicit functional and kernels are shown in Sec. 7.3.3. For the training data we also include density profiles from the HR case. In Fig. 7.6, we show the results. Test distributions match well to simulation data both in the HR limit and the regime of higher attractions. The eos shows an unphysical van der Waals loop for attractions strengths $\epsilon > 3.7$, much higher than the upper limit of the training data.

7.3.3 Explicit functional and convolution kernels

Here we show the full functional of $\mathcal{F}^{\rm ex,ML}[n]$, with

$$n_i(x) = \int dx'\, \rho(x')\omega_i(x-x'). \tag{7.11}$$

The coefficients in $\mathcal{F}^{\rm ex,ML}$ are single precision; for displaying purposes, all coefficients are rounded to the one decimal place and then rationalized.

$\mathcal{F}^{\rm ex,ML}$ for hard rod

The FEQL result for hard rod in Sec. 7.3.1 is

$$\mathcal{F}^{\rm ex,ML} = \int dx\, \frac{\frac{n_0^2}{5}+\frac{n_0}{10}y_0-\frac{n_2^2}{10}}{-\frac{n_0^2}{5}-\frac{n_0}{5}y_0-\frac{n_0}{10}+\frac{e^{y_1}}{5}+\frac{4}{5}} + y_2\left(-\frac{n_0^2}{5}-\frac{n_0}{10}y_0-\frac{3}{10}e^{y_1}+\frac{3}{10}\right)+e^{y_3}-1 \tag{7.12}$$

with $y_0=\frac{2n_0}{5}+\frac{n_2}{5}$, $y_1=\frac{3n_1}{5}$, $y_2=\frac{2n_0}{5}-\frac{n_1}{5}+\frac{n_2^2}{10}-\frac{n_2}{10}$, $y_3=\frac{n_0^2}{10}$ and convolution kernels ω_i shown in Fig.7.7a.

$\mathcal{F}^{\rm ex,ML}$ for LJ with splitting

In Sec. 7.3.2 with splitting, $\mathcal{F}^{\rm ex}=\mathcal{F}^{\rm HR}+\epsilon\mathcal{F}^{\rm ex,ML}_{\rm att}$, where

$$\begin{aligned}\mathcal{F}^{\rm ex,ML}_{\rm att} = \int dx\, &\frac{3}{5}y_0y_1\left(-\frac{\epsilon n_3}{2}-\frac{n_0}{10}-\frac{n_1}{10}-\frac{n_2}{2}+\frac{y_0y_1}{5}-\frac{y_2y_3}{5}-\frac{2y_4}{5y_5}\right)-\frac{y_0y_1}{10}-\frac{y_2y_3}{5}\\
&-\frac{y_2y_3}{10\left(\frac{\epsilon n_3}{5}+\frac{n_2}{5}-\frac{7y_0y_1}{10}+\frac{3y_2y_3}{5}-\frac{2\ln y_6}{5}+1-\frac{-\epsilon n_3-\frac{n_0}{2}-\frac{n_1}{10}-\frac{11n_2}{10}}{10y_5}\right)}\\
&+\left(\frac{3\epsilon n_3}{10}+\frac{n_0}{10}+\frac{3n_2}{10}-\frac{y_0y_1}{2}+\frac{9y_2y_3}{10}+\frac{\ln y_6}{10}+\frac{-\epsilon n_3-\frac{n_0}{2}-\frac{n_1}{10}-\frac{11n_2}{10}}{10y_5}\right)\\
&\left(-\frac{3\epsilon n_3}{10}-\frac{n_0}{10}-\frac{n_1}{10}-\frac{2n_2}{5}+\frac{3y_0y_1}{10}-\frac{3y_2y_3}{10}+\frac{e^{y_7}}{5}-\frac{1}{5}-\frac{9y_4}{10y_5}\right)+e^{-\frac{2y_0y_1}{5}-\frac{y_2y_3}{5}}+\ln\left(-\frac{y_2y_3}{5}+1\right)-1\end{aligned} \tag{7.13}$$

with

$$y_0=\frac{n_0}{5}-\frac{2n_1}{5}+\frac{n_2}{10},\ y_1=\frac{\epsilon n_3}{2}-\frac{3n_0}{10}-\frac{2n_1}{5}+\frac{3n_2}{10},\ y_2=\frac{\epsilon n_3}{10}+\frac{n_0}{5}-\frac{3n_1}{10}-\frac{2n_2}{5},\ y_3=\frac{\epsilon n_3}{10}+\frac{n_0}{5}+\frac{n_1}{5}-\frac{3n_2}{10},$$
$$y_4=-\epsilon n_3-\frac{n_0}{2}-\frac{n_1}{10}-\frac{11n_2}{10},\ y_5=-\frac{2\epsilon n_3}{5}-\frac{6n_1}{5}+1,\ y_6=-\frac{3\epsilon n_3}{10}+\frac{n_2}{10}+1,\ y_7=-\frac{\epsilon n_3}{5}+\frac{2n_0}{5}$$

and convolution kernels ω_i shown in Fig.7.7b

$\mathcal{F}^{\text{ex,ML}}$ for LJ without splitting

The result of $\mathcal{F}^{\text{ex}}$ given by FEQL in Sec. 7.3.2 without splitting is

$$\begin{aligned}\mathcal{F}^{\text{ex,ML}} = \int dx\, & \frac{y_0 \ln y_1}{10} + \frac{y_2 y_3}{10} + \frac{-\frac{y_4 y_5}{2} + \frac{3y_2 y_3}{10} - \frac{y_6 y_7}{2}}{\frac{3y_4 y_5}{10} + \frac{3\ln y_1}{10} + 1} + \left(-\frac{y_4 y_5}{5} + \frac{17e^{y_8}}{10} + \frac{4\ln y_1}{5} - \frac{17}{10}\right) \\ & \left(-\frac{3\epsilon n_3}{5} - \frac{n_0}{10} + \frac{n_2}{5} + \frac{y_2 y_3}{2} - \frac{9\ln y_1}{5}\right) + \left(-\frac{\epsilon n_3}{5} + \frac{n_2}{10} + \frac{3y_4 y_5}{10} + \frac{-\frac{n_0}{10} - \frac{n_1}{5} + \frac{n_2}{10}}{5y_9} + \frac{y_6 y_7}{5}\right) \\ & \left(-\frac{\epsilon n_3}{5} + \frac{n_2}{10} + \frac{2y_4 y_5}{5} + \frac{-\frac{n_0}{10} - \frac{n_1}{5} + \frac{n_2}{10}}{5y_9} + \frac{y_6 y_7}{5} + \frac{e^{y_8}}{10} - \frac{1}{10}\right) \\ & + e^{\frac{y_2 y_3}{5} - \frac{3y_6 y_7}{10}} + \ln\left(\frac{y_2 y_3}{10} + 1\right) - 1 \end{aligned} \tag{7.14}$$

with

$$y_0 = -\frac{\epsilon n_3}{5} + \frac{n_2}{10},\ y_1 = -\frac{7n_1}{10} - \frac{7n_2}{10} + 1,\ y_2 = \frac{3\epsilon n_5}{10} - \frac{2n_0}{5} + \frac{n_2}{10},\ y_3 = \frac{2\epsilon n_4}{5} - \frac{2\epsilon n_5}{5} - \frac{n_1}{10} - \frac{n_2}{10},$$
$$y_4 = -\frac{3n_0}{10} - \frac{n_1}{2} + \frac{3n_2}{10},\ y_5 = \frac{2n_0}{5} + \frac{2n_1}{5} - \frac{3n_2}{10},\ y_6 = -\frac{\epsilon n_5}{5} - \frac{3n_0}{10} - \frac{2n_1}{5} + \frac{3n_2}{10},$$
$$y_7 = \frac{\epsilon n_5}{2} + \frac{n_0}{10} + \frac{2n_1}{5} - \frac{n_2}{5},\ y_8 = \frac{n_0}{10} - \frac{3n_1}{10} - \frac{3n_2}{5},\ y_9 = -\frac{3n_0}{10} - \frac{n_1}{2} + \frac{n_2}{10} + 1$$

and convolution kernels ω_i shown in Fig.7.7c

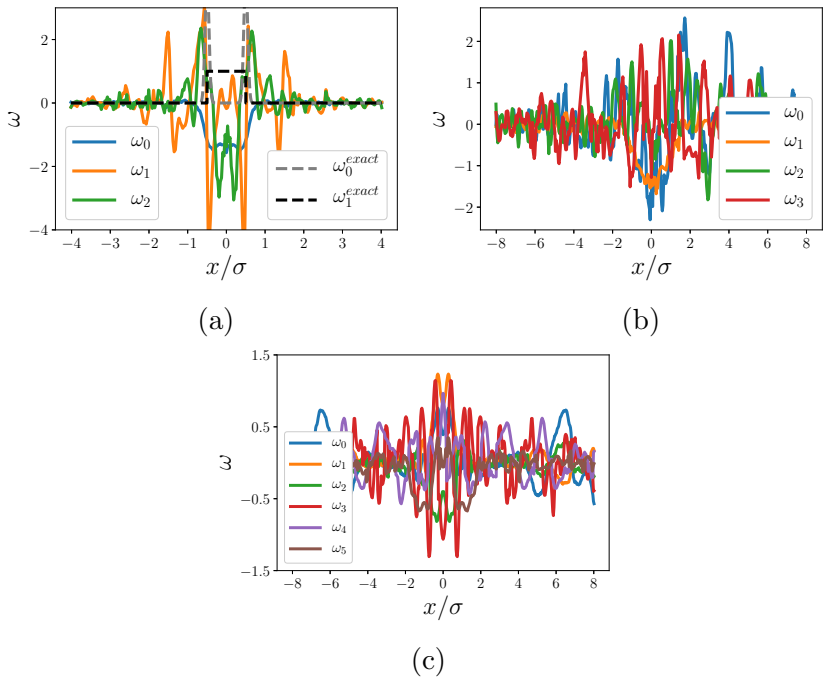

Figure 7.7: ω for all cases. (a)HR. The ω_i^{exact} are the exact weight kernels in Eqs. (3.55). (b)LJ, splitting (c)LJ, no splitting. The maximum allowed range for the kernels is $[-4\sigma, 4\sigma]$ in the HR case and $[-8\sigma, 8\sigma]$ in the LJ case.

7.3.4 Consistency of μ

In Eq. (7.5), μ_i^{ML} is determined by demanding that $\int(\rho_i^{\mathrm{ML}} - \rho_i^{\mathrm{eq}})^2$ is minimal, which entails that μ_i^{ML} varies during the iterations. This choice of μ_i^{ML} stabilizes the training process, and μ_i^{ML} is directly determined by

$$\frac{\partial}{\partial \mu_i^{\mathrm{ML}}} \int (\rho_i^{\mathrm{ML}} - \rho_i^{\mathrm{eq}})^2 = 0 \Rightarrow \mu_i^{\mathrm{ML}} = \ln\left(\frac{\int \rho_i^{\mathrm{eq}} \rho_i'^{\mathrm{ML}}}{\int (\rho_i'^{\mathrm{ML}})^2}\right), \tag{7.15}$$

where $\rho_i'^{\mathrm{ML}} = \exp\left(-\frac{\delta \mathcal{F}^{\mathrm{ex,ML}}}{\delta \rho}\Big|_{\rho=\rho_i^{\mathrm{eq}}} - V_i^{\mathrm{ext}}\right)$. If the training converges, μ^{ML} will converge to μ^{eq}. In Fig.7.8 we show $\Delta\mu = \mu^{\mathrm{eq}} - \mu^{\mathrm{ML}}$ versus μ^{eq} at the end of training for the three cases in Sec. 7.3.1 and 7.3.2. μ^{ML} is indeed close to μ^{eq}.

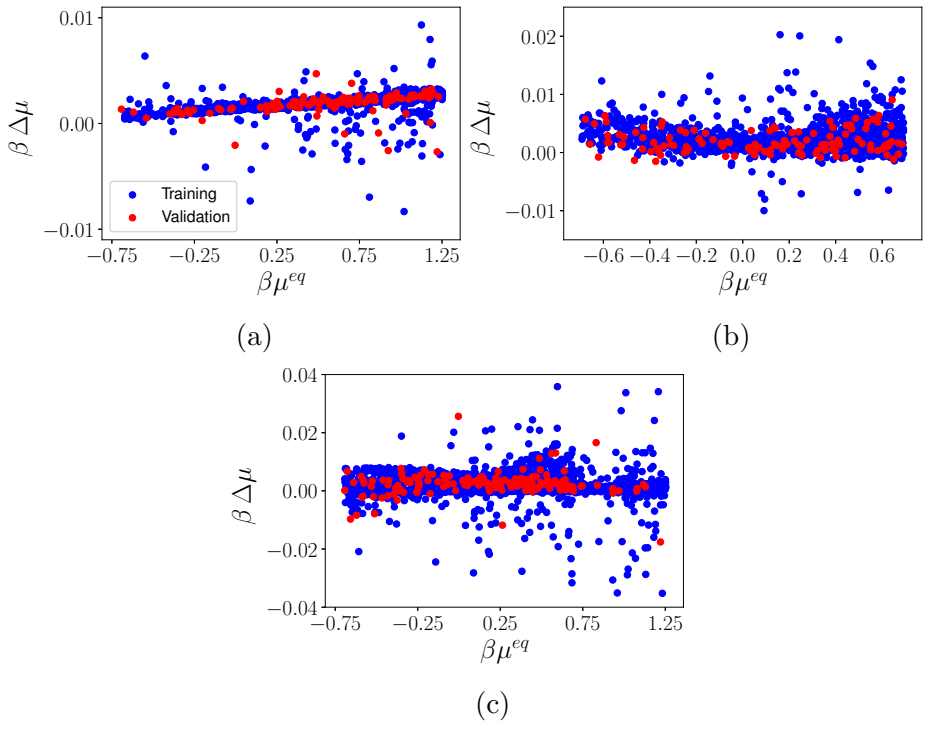

Figure 7.8: $\Delta\mu = \mu^{\mathrm{eq}} - \mu^{\mathrm{ML}}$ versus μ^{eq}. (a) HR (b) LJ with splitting (c) LJ, no splitting.

Furthermore, we also check $\mu(\rho) = \frac{\partial \mathrm{f}}{\partial \rho}$ (i.e. from the equation of state), where ρ here refers to the density of the bulk fluid. In Fig. 7.9 we show $\mu(\rho)$ from the exact functional, ML, and MC simulations for the three cases as in the Sec. 7.3.1 and 7.3.2. Deviations only occur for the LJ case well outside the training region.

In principle, one could also fix $\mu_i^{\mathrm{ML}} = \mu_i^{\mathrm{eq}}$ (the chemical potential of the data set) and then choose $\alpha_1 = 1$ and $\alpha_2 = 0$ in Eq. (7.7), but this requires smaller learning rates and results in much longer training processes. For example, the HR case with parameters as in the main paper can be done with learning rate $= 10^{-3}$ and the number of training iterations doubled.

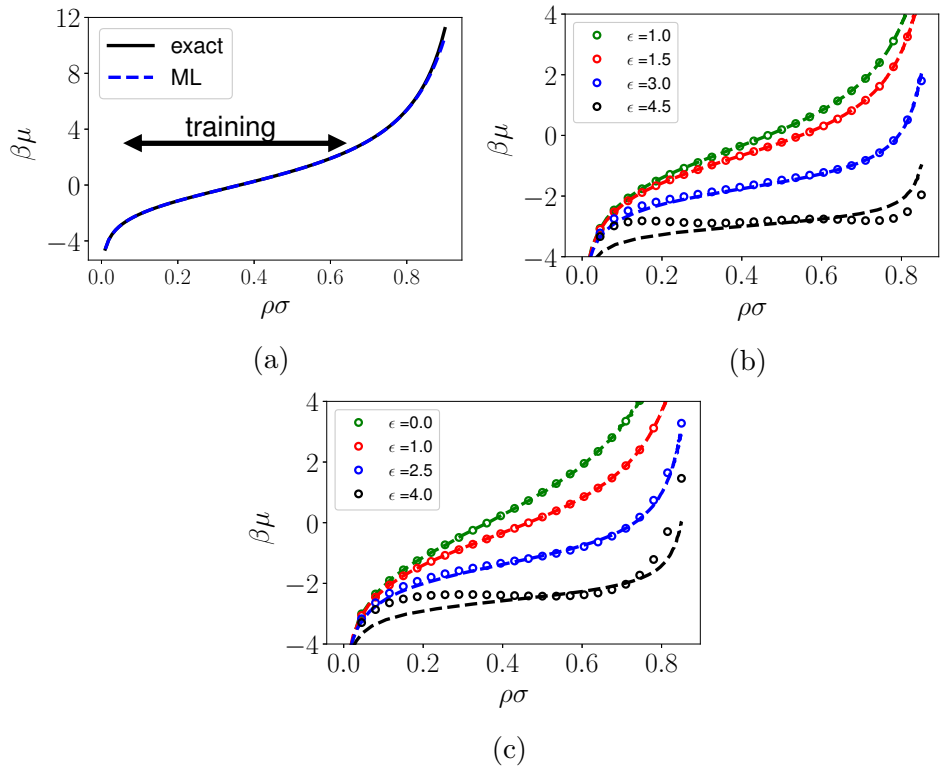

Figure 7.9: $\mu(\rho)$ versus ρ. (a) HR (b) LJ with splitting (c) LJ, no splitting. In (b) and (c), the circles are ML and dashed lines are MC simulations.

7.3.5 Direct correlation function

The direct correlation function (dcf) is a central object in DFT which through iterations yields the pair corelation function (Ornstein–Zernike relation, see Chapter 3 and also Ref. [23]). It is given by the second functional derivative of $\mathcal{F}^{\text{ex}}$:

$$C^{(2)}(x_1, x_2; \rho_0) = -\frac{\beta\delta^2\mathcal{F}^{\text{ex}}}{\delta\rho(x_1)\delta\rho(x_2)}, \tag{7.16}$$

and it depends only on $x = |x_1 - x_2|$ in the case of a homogeneous fluid with density ρ_0.

As the network is only trained on the level of the first functional derivative (see Eq. 6.2), it is a challenge for FEQL to capture the dcf. In Fig. 7.10, we show exemplary dcf's at moderate to high density for the exact HR functional, LJ from simulation and the corresponding ML results. The direct correlations inside the hard core are captured very well by ML in the HR and LJ cases. Outside the hard core, in the HR case, the $C^{(2)}$ from the ML shows insignificant correlation. In the case of LJ, the contribution to $C^{(2)}$ from attraction is semi–quantitatively correct, with a better result in the splitting case.

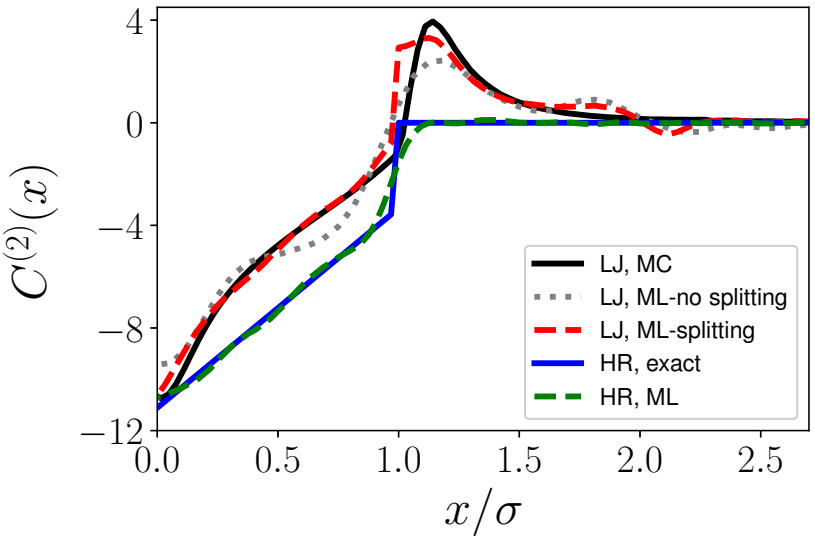

Figure 7.10: $C^{(2)}(x, \rho_0)$ with $\rho_0 = 0.7$ (HR) and 0.703 (LJ, $\epsilon = 1.85$ and $\mu = \ln(1.85)$).

7.3.6 Learning the exact HR functional

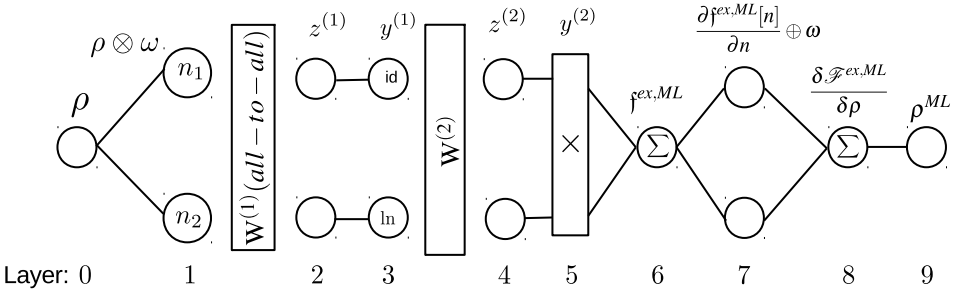

Figure 7.11: Simplified FEQL for hard–rod functional

As shown in Sec. 7.3.1, even though the learned functional for hard–rod fluids behaves well inside and outside the training region, it is not in the form of the Percus functional (Eq. (3.55)). This is understandable, since the convolution kernels of the latter are Dirac delta and Heaviside step functions, which are hard to be captured by our network. Also, the possible configuration of trained functionals, i.e, local minima, are too many such that the chance for FEQL to find the global minimum (the Percus functional) is scarce. To show that the FEQL is capable of delivering the "correct" functional, we limit $n_{\mathrm{w}} = 2$ and keep only the necessary nodes as shown in Fig. 7.11; thus the the untrained functional is

$$\mathcal{F}^{\mathrm{ex,ML}} = \int dx \; \left(a_2 L_0 \left(a_1 L_0 n_0 + a_1 L_1 n_1\right) + a_2 L_1 \ln\left(a_1 L_2 n_0 + a_1 L_3 n_1 + 1\right)\right) \times \left(a_2 L_3 \left(a_1 L_0 n_0 + a_1 L_1 n_1\right) + a_2 L_4 \ln\left(a_1 L_2 n_0 + a_1 L_3 n_1 + 1\right)\right) \tag{7.17}$$

with $a_x L_y$ the y–th trainable parameter in $W^{(x)}$.

We use 2048 density profiles as mentioned in Sec. 7.3.1 with a range of training reservoir densities $\rho_0 = 0.2...0.8$ for training, and add an extra penalty term

$$\sum_i \int_0^L \left| \left(\tanh\left(\frac{x-d}{w}\right) - \tanh\left(\frac{x-L+d}{w}\right) \right) \omega_i(x) \right| dx \tag{7.18}$$

with $d = 1\sigma$, $w = 0.1\sigma$ and L system size (32σ), into the cost function (Eq. (7.7)). Fig. 7.12 shows the tanh term in Eq. (7.18); this extra regularization strongly localizes ω's within $\pm 1\sigma$ (with periodic boundary condition).

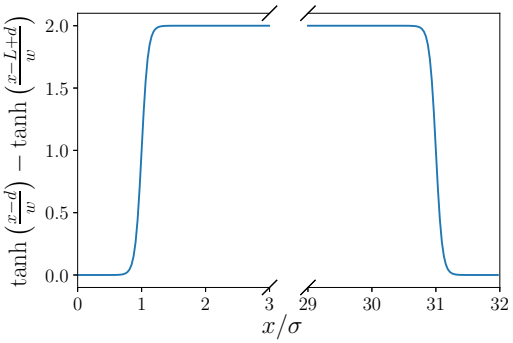

Figure 7.12: The tanh term in Eq. (7.18) with $d = 1\sigma$, $w = 0.1\sigma$ and $L = 32\sigma$ (system size).

The training procedure follows the three–steps method as mentioned in Sec. 7.2 and ω's are trained in Fourier space, since Dirac delta and Heaviside step functions are smooth functions in Fourier space (see Fig. 7.13 and Appendix A for details). After training with 50 different random seeds, we obtain only one result with the exact form of the Percus functional:

$$\mathcal{F}^{\mathrm{ex,ML}} = \int dx \, \left(-1.0003 n_0 \ln\left(1 - 1.0002 n_1\right)\right), \tag{7.19}$$

and almost exact weight functions as shown in Fig. 7.13 with ω's normalized by $\int dx\, \omega_i = 1$.

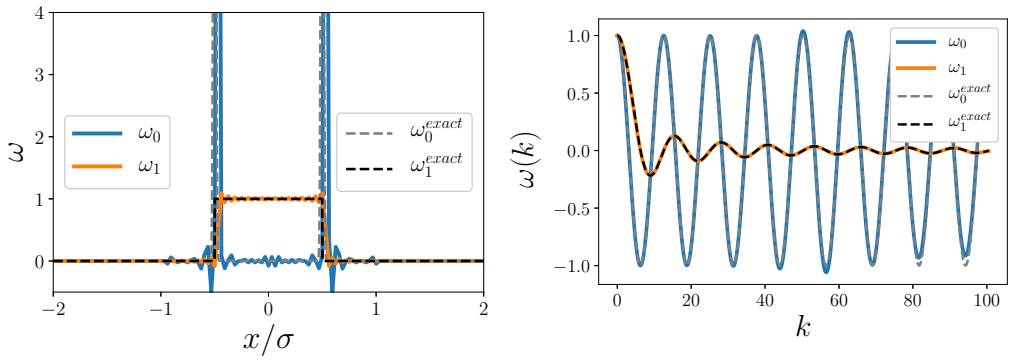

(a) (b)

Figure 7.13: The weight functions in Eq. (7.19) and the Percus functional (exact) in (a) real space and (b) Fourier space.

In short, FEQL in principle is able to deliver the exact functional in this case. However, it requires a much smaller network compared to Sec. 7.3.1

and an extra regularization. Also the result is sensitive to the initial guesses of $a_x L_y$'s in Eq. (7.17), which is probably due the size of the network. Its restricted form is in contradiction to having a "flexible" network as used in the previous sections. Nevertheless, here we only attempt to demonstrate that it is possible to obtain the exact functional from FEQL.

7.4 Conclusion

The adaptation of EQL [22] to the classical DFT problem of finding $\mathcal{F}^{\text{ex}}$ has shown satisfactory results for the exemplary cases of the 1D HR and LJ fluid. The new network FEQL is very flexible and goes significantly beyond the polynomial *ansatz* used in Ref. [2]. The analytic form allows for more easily transferable output and further calculations to obtain, e.g., direct correlation functions. Also, for the HR case, it is possible to deliver the exact functional while it requires a limited network with an extra regularization based on the prior knowledge of the exact HR functional.

An application to more realistic systems in 3D and perhaps also complex fluids, such as water, appears to be promising [82, 83, 84]. From the results of this work we conclude that the incorporation of results from liquid state theory is not essential here; however, it increases the reliability and trainability of the ML functional. Future work should include information on virial or high density expansions as well as correlation functions (via test particles) and should develop more quantitative measures for extrapolative capabilities of ML functionals.

Appendices

Appendix A

Convolution and Fourier transformation

A.1 Convolution

In order to obtain the excess free energy density of the density profile $\rho(\mathbf{r})$ in FMT or machine learning, one needs to calculate the weighted densities n_i, which are the convolution of the weight functions ω^i with $\rho(\mathbf{r})$:

$$n_i(\mathbf{r}) = \rho \otimes \omega^i = \int d\mathbf{r}'\, \rho(\mathbf{r}')\omega^i(\mathbf{r} - \mathbf{r}'). \tag{A.1}$$

In FMT, it is more convenient to use the convolution theorem. For two arbitrary well–defined functions f and g, the convolution theorem states that the Fourier transform of their convolution $f \otimes g$ is equal to the product of their Fourier transforms. Defining the forward and backward Fourier transform of the function f as

$$\mathrm{FT}[f(\mathbf{r})] = \widetilde{f}(\mathbf{k}) = \int d\mathbf{r}\, e^{-i\mathbf{k}\cdot\mathbf{r}} f(\mathbf{r}) \tag{A.2}$$

$$\mathrm{FT}^{-1}[\widetilde{f}(\mathbf{k})] = f(\mathbf{r}) = \frac{1}{(2\pi)^D} \int d\mathbf{k}\, e^{i\mathbf{k}\cdot\mathbf{r}} \widetilde{f}(\mathbf{k}) \tag{A.3}$$

with D the dimension. The short proof of convolution theorem is as follows.

$$\begin{aligned}
\mathrm{FT}[f \otimes g] &= \int\int d\mathbf{r}d\mathbf{r}' e^{-i\mathbf{k}\cdot\mathbf{r}} f(\mathbf{r}')g(\mathbf{r}-\mathbf{r}') \\
&= \int\int d\mathbf{r}d\mathbf{r}' e^{-i\mathbf{k}\cdot\mathbf{r}'} f(\mathbf{r}')e^{-i\mathbf{k}\cdot(\mathbf{r}-\mathbf{r}')}g(\mathbf{r}-\mathbf{r}') \\
&= \int\int d\left(\mathbf{r}-\mathbf{r}'\right) d\mathbf{r}' e^{-i\mathbf{k}\cdot\mathbf{r}'} f(\mathbf{r}')e^{-i\mathbf{k}\cdot(\mathbf{r}-\mathbf{r}')}g(\mathbf{r}-\mathbf{r}') \\
&= \widetilde{f}(\mathbf{k})\widetilde{g}(\mathbf{k}). \qquad \text{(A.4)}
\end{aligned}$$

A.2 Fourier transformation in FMT

A.2.1 3D

In 3D FMT, the weight functions in real space are:

$$\begin{aligned}
&\omega_3(\mathbf{r}) = \Theta(R-|\mathbf{r}|), \\
&\omega_2(\mathbf{r}) = \delta(R-|\mathbf{r}|), \\
&\omega_1(\mathbf{r}) = \frac{\omega_2^i(\mathbf{r})}{4\pi R}, \\
&\omega_0(\mathbf{r}) = \frac{\omega_2^i(\mathbf{r})}{4\pi R^2}, \\
&\boldsymbol{\omega}_2(\mathbf{r}) = \frac{\mathbf{r}}{|\mathbf{r}|}\delta(R-|\mathbf{r}|), \\
&\boldsymbol{\omega}_1(\mathbf{r}) = \frac{\boldsymbol{\omega}_2(\mathbf{r})}{4\pi R}, \text{and} \\
&\boldsymbol{\omega}_{\mathrm{T}}(\mathbf{r}) = \left(\frac{\mathbf{r}\cdot\mathbf{r}^t}{|\mathbf{r}|^2} - \frac{\mathbb{I}}{3}\right)\delta(R-|\mathbf{r}|). \qquad \text{(A.5)}
\end{aligned}$$

where $\mathbb{I}$ is the unit matrix in $\mathbb{R}^{3\times3}$, superscript t represents the transpose, and R is the radius of hard spheres. The necessary Fourier transformation of the weight functions are:

$$\begin{aligned}
&\widetilde{\omega}_3(\mathbf{k}) = \frac{4\pi}{|\mathbf{k}|^3}\left(\sin\left(|\mathbf{k}|R\right) - |\mathbf{k}|R\cos\left(|\mathbf{k}|R\right)\right), \\
&\widetilde{\omega}_2(\mathbf{k}) = \frac{4\pi}{|\mathbf{k}|}R\sin(|\mathbf{k}|R), \\
&\widetilde{\boldsymbol{\omega}}_2(\mathbf{k}) = -i\mathbf{k}\widetilde{\omega}_3(\mathbf{k}), \text{and} \\
&\widetilde{\boldsymbol{\omega}}_{\mathrm{T}}(\mathbf{k}) = \left(\widetilde{\omega}_2(\mathbf{k}) - \frac{3}{R}\widetilde{\omega}_3(\mathbf{k})\right)\left(\frac{\mathbf{k}\cdot\mathbf{k}^t}{|\mathbf{k}|^2} - \frac{\mathbb{I}}{3}\right) \qquad \text{(A.6)}
\end{aligned}$$

where $\mathbf{k}$ is the reciprocal lattice vector, and $\mathbf{k}^t$ denotes the transpose of $\mathbf{k}$. The explicit calculations of Fourier transformations of weight functions can be found in Ref. [85, 86]. In the limit $|\mathbf{k}| \to 0$,

$$\begin{aligned}
\lim_{|\mathbf{k}|\to 0} \widetilde{\omega}_3(\mathbf{k}) &= \frac{4\pi}{3}R^3, \\
\lim_{|\mathbf{k}|\to 0} \widetilde{\omega}_2(\mathbf{k}) &= 4\pi R^2, \\
\lim_{|\mathbf{k}|\to 0} \widetilde{\boldsymbol{\omega}}_2(\mathbf{k}) &= 0, \text{and} \\
\lim_{|\mathbf{k}|\to 0} \widetilde{\boldsymbol{\omega}}_{\mathrm{T}}(\mathbf{k}) &= 0.
\end{aligned} \tag{A.7}$$

A.2.2 2D

In 2D FMT, the weight functions appearing in Eq. (3.51) in real space are:

$$\begin{aligned}
\omega_0(\mathbf{r}) &= \frac{\delta(R-|\mathbf{r}|)}{2\pi R}, \\
\omega_2(\mathbf{r}) &= \Theta(R-|\mathbf{r}|), \\
\boldsymbol{\omega}_0(\mathbf{r}) &= \delta(R-|\mathbf{r}|), \\
\boldsymbol{\omega}_1(\mathbf{r}) &= \frac{\mathbf{r}}{|\mathbf{r}|}\delta(R-|\mathbf{r}|), \text{and} \\
\boldsymbol{\omega}_2(\mathbf{r}) &= \frac{\mathbf{r}\cdot\mathbf{r}^t}{|\mathbf{r}|^2}\delta(R-|\mathbf{r}|).
\end{aligned} \tag{A.8}$$

The necessary Fourier transformation of the weight functions are:

$$\begin{aligned}
\widetilde{\omega}_2(\mathbf{k}) &= 2\pi R\frac{J_1(|\mathbf{k}|R)}{|\mathbf{k}|}, \\
\widetilde{\boldsymbol{\omega}}_0(\mathbf{k}) &= 2\pi R J_0(|\mathbf{k}|R), \\
\widetilde{\boldsymbol{\omega}}_1(\mathbf{k}) &= -i\mathbf{k}\widetilde{\omega}_2(\mathbf{k}), \text{and} \\
(\widetilde{\boldsymbol{\omega}}_2(\mathbf{k}))_{ij} &= -\frac{2\pi}{R}\frac{\partial}{\partial k_i}\frac{\partial}{\partial k_j}J_0(\sqrt{k_x^2+k_y^2}R).
\end{aligned} \tag{A.9}$$

with J_i the i–th order of the Bessel function of the first kind.

In the limit $|\mathbf{k}| \to 0$,

$$\begin{aligned}
\lim_{|\mathbf{k}|\to 0} \widetilde{\omega}_2(\mathbf{k}) &= \pi R^2, \\
\lim_{|\mathbf{k}|\to 0} \widetilde{\boldsymbol{\omega}}_0(\mathbf{k}) &= 2\pi R, \\
\lim_{|\mathbf{k}|\to 0} \widetilde{\boldsymbol{\omega}}_1(\mathbf{k}) &= 0, \text{and} \\
\lim_{|\mathbf{k}|\to 0} \widetilde{\boldsymbol{\omega}}_2(\mathbf{k}) &= \pi R\,\mathbb{I}.
\end{aligned} \tag{A.10}$$

Explicit Fourier transformations

In order to obtain the Fourier transformation of the weight functions, we assume that the wave vector $\mathbf{k}$ is parallel to the x component of the real–space coordinate system. Therefore, in terms of the 2D polar coordinates (r, θ) in Eq. (A.2) reads: $\mathbf{k} \cdot \mathbf{r} = kr\cos\theta$ with $k = |\mathbf{k}|$.
Thus, the Fourier transformation of ω_2 is given by

$$\begin{aligned}\widetilde{\omega}_2(\mathbf{k}) &= \int_0^{2\pi}\int_0^{\infty} \Theta(R-|\mathbf{r}|)e^{-ikr\cos\theta} r dr d\theta \\ &= \int_0^{2\pi}\int_0^{R} e^{-ikr\cos\theta} r dr d\theta \\ &= \frac{2\pi R J_1(kR)}{k}. \end{aligned} \tag{A.11}$$

The Fourier transformation of $\boldsymbol{\omega}_0$ is given by

$$\begin{aligned}\widetilde{\boldsymbol{\omega}}_0(\mathbf{k}) &= \int_0^{2\pi}\int_0^{\infty} \delta(R-|\mathbf{r}|)e^{-ikr\cos\theta} r dr d\theta \\ &= \int_0^{2\pi} e^{-ikR\cos\theta} R d\theta \\ &= 2\pi R J_0(kR). \end{aligned} \tag{A.12}$$

The Fourier transformation of $\boldsymbol{\omega}_1$ is given by

$$\begin{aligned}\widetilde{\boldsymbol{\omega}}_1(\mathbf{k}) &= \int_0^{2\pi}\int_0^{\infty} \delta(R-|\mathbf{r}|)e^{-ikr\cos\theta} \begin{pmatrix}\cos\theta \\ \sin\theta\end{pmatrix} r dr d\theta \\ &= \begin{pmatrix}-2\pi i R J_1(kR) \\ 0\end{pmatrix}. \end{aligned} \tag{A.13}$$

This implies that the resulting Fourier transformation is in the direction of x–axis in the real space, which is equivalent to the unit vector in reciprocal space $\mathbf{k}/k$. As a result,

$$\widetilde{\boldsymbol{\omega}}_1(\mathbf{k}) = -2\pi i R J_1(kR)\frac{\mathbf{k}}{k} = -i\mathbf{k}\widetilde{\omega}_2(\mathbf{k}). \tag{A.14}$$

Similarly, the Fourier transformation of the tensor weight $\boldsymbol{\omega}_2$ is given by

$$\begin{aligned}\widetilde{\boldsymbol{\omega}}_2(\mathbf{k}) &= \int_0^{2\pi}\int_0^{\infty} \delta(R-|\mathbf{r}|)e^{-ikr\cos\theta} \begin{bmatrix}\cos^2\theta & \cos\theta\sin\theta \\ \cos\theta\sin\theta & \sin^2\theta\end{bmatrix} r dr d\theta \\ &= \begin{bmatrix}\frac{2\pi(J_1(kR)-kRJ_2(kR))}{k} & 0 \\ 0 & \frac{2\pi J_1(kR)}{k}\end{bmatrix} \\ &= \frac{2\pi J_1(kR)}{k}\mathbb{I} - 2\pi R J_2(kR)\begin{bmatrix}1 & 0 \\ 0 & 0\end{bmatrix}. \end{aligned} \tag{A.15}$$

With the similar argument of $\widetilde{\boldsymbol{\omega}}_1(\mathbf{k})$, we obtain

$$\widetilde{\boldsymbol{\omega}}_2(\mathbf{k}) = \frac{2\pi J_1(kR)}{k}\mathbb{I} - 2\pi R J_2(kR)\begin{bmatrix} k_x^2 & k_xk_y \\ k_xk_y & k_y^2 \end{bmatrix}, \tag{A.16}$$

which is equivalent to the representation in Eq. (A.9).

A.2.3 1D

In 1D FMT, the weight functions in real space are:

$$\begin{aligned} \omega_1(x) &= \Theta(R-|x|), \text{and} \\ \omega_0(x) &= \frac{1}{2}\delta(R-|x|). \end{aligned} \tag{A.17}$$

The Fourier transformation of the weight functions are:

$$\begin{aligned} \widetilde{\omega}_1(\mathbf{k}) &= 2\frac{\sin(|\mathbf{k}|R)}{|\mathbf{k}|}, \text{and} \\ \widetilde{\omega}_0(\mathbf{k}) &= \cos(|\mathbf{k}|R). \end{aligned} \tag{A.18}$$

In the limit $|\mathbf{k}| \to 0$,

$$\begin{aligned} \lim_{|\mathbf{k}|\to 0} \widetilde{\omega}_1(\mathbf{k}) &= 2R, \text{and} \\ \lim_{|\mathbf{k}|\to 0} \widetilde{\omega}_0(\mathbf{k}) &= 1. \end{aligned} \tag{A.19}$$

A.3 Numerics

In order to determine the convolution and cross-correlation in Eqs.(5.2), (A.1) and (B.3), the Fourier transforms of the density profile are computed using the fast Fourier library, which performs discrete Fourier transform of a given complex array. To provide an example, in 2D the components of the wave vector $\mathbf{k} = (k_x, k_y)$ are determined by

$$\begin{aligned} k_x[n_x] &= n_x\, 2\pi/l_x \quad \text{if} \quad 0 \le n < N_x/2 \\ k_x[n_x] &= (n_x - N_x)\, 2\pi/l_x \quad \text{if} \quad N_x/2 \le n < N_x \\ k_y[n_y] &= n_y\, 2\pi/l_y \quad \text{if} \quad 0 \le n_y \le N_y/2. \end{aligned} \tag{A.20}$$

with $n_{x/y}$ the n–th point in the array, $l_{x/y}$ the length and $N_{x/y}$ grid points in the x/y direction and n_y only runs from 0 to $N_y/2$. For details please check the section "What FFTW Really Computes" in the manuel of *Fastest Fourier Transform in the West* [87].

Since the FMT kernels ω_i are unchanged throughout the code, it is reasonable to calculate FT[ω] first and store them to be used for the numerical implementations. The convolution for example in python by the library `Numpy` is simply as `n=numpy.fft.irfft2(numpy.fft.rfft2(rho)*wk)` with `rho` the density distribution and `wk` the analytic expression of FT[ω]. For a GPU implementation, we refer Ref. [88] for reads who have a deeper interest.

Furthermore, one should set `(numpy.fft.rfft2(rho)*wk)[ni][nj]` to zero if `ni==Nx/2` or `nj==Ny/2` before performing the back Fourier transform [87, 89].

Appendix B

Free energy minimization

To obtain the equilibrium density profiles, for example crystal and crystal–fluid interfaces in Chap. 4 and 5, and inhomogeneous fluids under external potentials in Chap. 6 and 7, one need to minimize the free energy, which is to solve (Eq. (2.27))

$$\rho^{\mathrm{eq}} = \exp\left(\mu - \left.\frac{\delta\mathcal{F}^{\mathrm{ex}}}{\delta\rho}\right|_{\rho=\rho^{\mathrm{eq}}} - V^{\mathrm{ext}}\right), \tag{B.1}$$

where

$$\frac{\delta F_{\mathrm{ex}}[n_\alpha]}{\delta\rho(\mathbf{r})} = \int d\mathbf{r}' \sum_\alpha \frac{\partial\Phi[n_\alpha]}{\partial n_\alpha}(\mathbf{r}')\omega_\alpha(\mathbf{r}'-\mathbf{r}) \tag{B.2}$$

is a cross–correlation and weighted density $n_\alpha(x) = \int dx'\,\rho(x')\omega_\alpha(x-x')$ is convolution. The reason for the appearance of cross–correlations lies in the definition of the weighted density (n) and its functional derivative:

$$\begin{aligned}\frac{\delta n_i(x)}{\delta\rho(y)} &= \int dx'\,\frac{\delta\rho(x')}{\delta\rho(y)}\omega_i(x-x') \\ &= \int dx'\,\delta(x'-y)\omega_i(x-x') \\ &= \omega_i(x-y). \end{aligned} \tag{B.3}$$

Thus, the functional derivative of the free energy,

$$\begin{aligned}\frac{\delta\mathcal{F}[\rho]}{\delta\rho(x)} &= \sum_i \int \frac{\partial\Phi}{\partial n_i}(x')\,\frac{\delta n_i(x')}{\delta\rho(x)}dx' \\ &= \sum_i \int \frac{\partial\Phi}{\partial n_i}(x')\,\omega_i(x'-x)dx' \end{aligned} \tag{B.4}$$

$$\tag{B.5}$$

Similar to the convolution theorem, the cross–correlation theorem is

$$\begin{aligned}
\mathrm{FT}[f \oplus g] &= \int\int d\mathbf{r}d\mathbf{r}' e^{-i\mathbf{k}\cdot\mathbf{r}} f(\mathbf{r}')g(\mathbf{r}'-\mathbf{r}) \\
&= \int\int d\mathbf{r}d\mathbf{r}' e^{-i\mathbf{k}\cdot\mathbf{r}'} f(\mathbf{r}')e^{i\mathbf{k}\cdot(\mathbf{r}'-\mathbf{r})} g(\mathbf{r}'-\mathbf{r}) \\
&= \int\int d\left(\mathbf{r}'-\mathbf{r}\right) d\mathbf{r}' e^{-i\mathbf{k}\cdot\mathbf{r}'} f(\mathbf{r}')e^{i\mathbf{k}\cdot(\mathbf{r}'-\mathbf{r})} g(\mathbf{r}'-\mathbf{r}) \\
&= \widetilde{f}(\mathbf{k})\widetilde{g}(-\mathbf{k}), \qquad \text{(B.6)}
\end{aligned}$$

where $\oplus$ is cross–correlation. Here we provide three methods to solve Eq. (2.27) in the following sections.

B.1 Picard method

The Picard iteration schema is named after Charles Émile Picard (1856-1941). With a given density profile ρ, the j–th step iteration is

$$\exp\left(-\beta\frac{\delta F_{\mathrm{ex}}\left[n_\alpha\right]}{\delta\rho}\bigg|_{\rho=\rho^j} + \beta\mu\right) = K[\rho^j]. \qquad \text{(B.7)}$$

The chemical potential μ is constant or adapted in each iteration step to keep $\bar{\rho}$ constant. Picard steps are performed according to

$$\rho^{j+1} = \xi\, K[\rho^j] + (1-\xi)\rho^j, \qquad \text{(B.8)}$$

where ξ is a Picard mixing parameter. For 2D crystal–fluid interfaces, $\xi = 10^{-2}$ for one–component and 10^{-3} for the binary systems. For 3D crystal around the crystal–fluid coexistence, $\xi = 10^{-5} \sim 10^{-6}$.

B.2 Direct inversion in iterative subspace

In this section, only crucial ingredients for the calculation are mentioned, and for details we refer readers to Ref [90]. The direct inversion in iterative subspace (DIIS) is a numerical method which speeds up the convergence [91]. DIIS approximates the final solution by a linear combination of a finite number n of (Picard) iteration outputs, i.e.

$$\rho^{\mathrm{DIIS}} = \sum_{i=1}^{n} c_i \rho^i, \qquad \text{(B.9)}$$

with $\sum c_i = 1$ (particle number conservation). To minimize the norm of the residual vector $d = \rho^{\text{DIIS}} - \rho^{\text{eq}}$ with constrain $\sum c_i = 1$, we define a Lagrangian

$$L = \langle d|d\rangle - 2\lambda \left(\sum_i c_i - 1 \right) \tag{B.10}$$

where λ is a Lagrange multiplier and $\langle d|d\rangle$ is inner product of d. By substituting $d = \sum c_i d_i = \sum c_i(\rho_i - \rho^{\text{eq}})$ into L, we obtain

$$L = \sum_{ij} c_i c_j \langle d_i|d_j\rangle - 2\lambda \left(\sum_i c_i - 1 \right). \tag{B.11}$$

With $\frac{\partial L}{\partial c_i} = 0$ and $\frac{\partial L}{\partial \lambda} = 0$, we obtain a matrix equation

$$\begin{pmatrix} \langle d_1|d_1\rangle & \langle d_1|d_2\rangle & \cdots & \langle d_1|d_n\rangle & -1 \\ \langle d_2|d_1\rangle & \langle d_2|d_2\rangle & \cdots & \langle d_2|d_n\rangle & -1 \\ \vdots & \vdots & \ddots & \vdots & \vdots \\ \langle d_n|d_1\rangle & \langle d_n|d_2\rangle & \cdots & \langle d_n|d_n\rangle & -1 \\ -1 & -1 & \cdots & -1 & 0 \end{pmatrix} \begin{pmatrix} c_1 \\ c_2 \\ \vdots \\ c_n \\ \lambda \end{pmatrix} = \begin{pmatrix} 0 \\ 0 \\ \vdots \\ 0 \\ -1 \end{pmatrix},$$

where $\langle d_i|d_j\rangle$ is inner product of d_i and d_j.

In practice, since ρ^{eq} is unknown, we approximate d_i by $d_i \simeq \rho_i - K[\rho_i]$, where $K[\rho_i]$ is defined in Eq. (B.7), and we perform m times Picard iterations, and use the output of the final n steps ($n < m$) to determine the residuum vector d_i and matrix and thus determine ρ^{DIIS}. Empirically, $n = 5 \sim 15$ is a reasonable choose. It is worth to note that DIIS may result in divergence (packing fraction larger than 1 or negative ρ), and thus one should check whether $\mathcal{F}^{\text{ex}}[\rho^{\text{DIIS}}]$ is finite or not, before taking ρ^{DIIS}.

B.3 Dynamic density functional theory

Starting from overdamped dynamics, a particle current $\mathbf{j}(r,t)$ due to the spatial gradient of the chemical potential μ is assumed as

$$\mathbf{j}(\mathbf{r},t) = -\rho(\mathbf{r},t)\nabla\Gamma\mu(\mathbf{r},t) \tag{B.12}$$

with Γ mobility. In a combination with the continuity equation $\frac{\partial\rho}{\partial t} = -\nabla\cdot\mathbf{j}$, $\mu = \frac{\delta F}{\delta\rho}$, and ideal gas limit, this yields the basis of dynamic density functional theory (DDFT):

$$\frac{\partial\rho(\mathbf{r},t)}{\partial t} = \beta D_0 \nabla\cdot\left(\frac{1}{\beta}\nabla\rho(\mathbf{r},t) + \rho(\mathbf{r},t)\nabla\frac{\delta\mathcal{F}^{\text{ex}}[\rho(\mathbf{r},t)]}{\delta\rho(\mathbf{r},t)} + \rho(\mathbf{r},t)\nabla V_{\text{ext}}(\mathbf{r}) \right) \tag{B.13}$$

where $\mathcal{F}^{\text{ex}}$ is the excess free energy and D_0 is ideal gas diffusion constant ($D(\mathbf{r}) = k_{\text{B}}T\Gamma(\mathbf{r})$, and in ideal gas approximation, $D(\mathbf{r}) = D_0$). Eq. (B.13) can be written as

$$\frac{\partial \rho}{\partial \tau} = \nabla^2 \rho + \nabla \cdot \mathbf{G} \tag{B.14}$$

with $\tau = D_0\, t$ and $\mathbf{G} = \beta \left(\rho \nabla \left(\frac{\delta \mathcal{F}^{\text{ex}}}{\delta \rho} + V_{ext} \right) \right)$. While it is possible to perform Eq. (B.14) in real space, it is more convenient in Fourier space. With the Fourier transform on the both sides of Eq. (B.14), it becomes

$$\frac{\partial \widetilde{\rho}}{\partial \tau} = -k^2 \widetilde{\rho} - i\mathbf{k} \cdot \widetilde{\mathbf{G}}. \tag{B.15}$$

An efficient way for Eq. (B.15) is the pseudo spectrum method [92]. In this case, we rewrite Eq. (B.15) as

$$\frac{\partial}{\partial \tau} \widetilde{\rho} e^{k^2 \tau} = \widetilde{f} e^{k^2 \tau} \tag{B.16}$$

where $\widetilde{f} = -i\mathbf{k} \cdot \widetilde{\mathbf{G}}$. Integrating on the both sides,

$$\int_{\tau}^{\tau+\Delta\tau} d\tau' \, \frac{\partial}{\partial \tau'} \widetilde{\rho}(\tau') \exp(k^2 \tau') = \int_{\tau}^{\tau+\Delta\tau} d\tau' \, \widetilde{f}(\tau') \exp\left(k^2 \tau'\right), \tag{B.17}$$

gives

$$\begin{aligned} \widetilde{\rho}(\tau + \Delta\tau) =& \widetilde{\rho}(\tau) \exp(-k^2 \Delta\tau) \\ &+ \exp\left(-k^2 \left(\tau + \Delta\tau\right)\right) \int_{\tau}^{\tau+\Delta\tau} d\tau' \, \widetilde{f}(\tau') \exp\left(k^2 \tau'\right) \end{aligned} \tag{B.18}$$

and approximating

$$\widetilde{f}(\tau') \simeq \widetilde{f}(\tau) + \frac{\widetilde{f}(\tau) - \widetilde{f}(\tau - \Delta\tau)}{\Delta\tau} (\tau' - \tau) \tag{B.19}$$

gives

$$\widetilde{\rho}(\tau + \Delta\tau) = \widetilde{\rho}(\tau) \exp(-k^2 \Delta\tau) + I_1 + I_2, \tag{B.20}$$

where

$$I_1 = -\frac{\widetilde{f}}{k^2} \left(\exp\left(-k^2 \Delta\tau\right) - 1 \right) \tag{B.21}$$

and

$$I_2 = \frac{\widetilde{f}(\tau) - \widetilde{f}(\tau - \Delta\tau)}{\Delta\tau} \left(\frac{\Delta\tau}{k^2} - \frac{1}{k^4} \left(1 - \exp\left(-k^2 \Delta\tau\right) \right) \right). \tag{B.22}$$

Note that $\widetilde{\rho}(\mathbf{k} = 0)$ is unchanged through iterations due to the particle number conservation.

Even though this algorithm is more memory intensive and complex than the Euler scheme, the overall performance is superior. For example, $\Delta\tau$ can be set $\sim 10^{-3}$ for HD crystal–fluid systems in 2D with this method, while $\sim 10^{-5}$ with the Euler scheme. However, even with setting $\Delta\tau < 10^{-6}$, it is still is not enough for stabilizing the crystal–fluid interface in 3D HS systems. Empirically, for 2D HD systems, DDFT is more efficient than Picard–DIIS if the system is far from the equilibrium state. Thus for crystal–fluid interface, it may be worth to perform some (thousands) DDFT steps and then switch to the Picard–DIIS method.

B.4 Convergence

To check convergence, one can calculate the residuum $\epsilon = \frac{1}{V}\int(\rho - K[\rho])^2$ with K in Eq. (B.7) and V the size of the simulation box. If ϵ is smaller than a certain threshold, then the iteration stops. Empirically, the threshold is chosen as 10^{-9} for determining coexistence properties and 10^{-7} for crystal-fluid interface. It is worth to note that one should also check the maximum of $(\rho - K[\rho])^2$ for interface problems, since the main contribution of residuum localizes around interfaces.

Appendix C

Direct correlation function by FMT

In Chapter 3, we introduced the direct correlation function $C^{(2)}$. In density functional theory (DFT) with the weighted density approaches,

$$C^{(2)}(\mathbf{r}_1, \mathbf{r}_2) = -\beta \frac{\delta^2 \mathcal{F}^{\text{ex}}[n(\rho)]}{\delta\rho(\mathbf{r}_1)\delta\rho(\mathbf{r}_2)} = -\beta \int \sum_{ij} \Phi_{ij}(\mathbf{r}')\omega_i(\mathbf{r}' - \mathbf{r}_1)\omega_j(\mathbf{r}' - \mathbf{r}_2) d\,\mathbf{r}' \tag{C.1}$$

with Φ the free energy density , $\Phi_{ij} = \frac{\partial^2}{\partial n_i \partial n_j}\Phi$, n the set of weighted densities, ω the weight functions and $\beta = \frac{1}{k_{\text{B}}T}$. We set $\beta = 1$ for simplicity. In the following we choose the FMT free energy functional (Chapter 3, 3D : Eq. (3.46), 2D : Eq. (3.51) and 1D : Eq. (3.55)). Solving Eq. (C.1) in real space is difficult due to ω being either the Dirac delta function or Heaviside step function, but they have analytic forms in Fourier space; thus, we perform Fourier transform on both sides of Eq. (C.1):

$$\begin{aligned}
&\widetilde{C}^{(2)}(\mathbf{k}_1, \mathbf{k}_2) \\
&= -\int\int\int \sum_{ij} \Phi_{ij}(\mathbf{r}')\omega_i(\mathbf{r}' - \mathbf{r}_1)\omega_j(\mathbf{r}' - \mathbf{r}_2) \exp(-i\mathbf{k}_1\mathbf{r}_1) \exp(-i\mathbf{k}_2 \cdot \mathbf{r}_2) d\,\mathbf{r}' d\,\mathbf{r}_1 d\,\mathbf{r}_2 \\
&= -\int\int\int \sum_{ij} \Phi_{ij}(\mathbf{r}') \exp(-i(\mathbf{k}_1 + \mathbf{k}_2)\mathbf{r}')\omega_i(\mathbf{r}' - \mathbf{r}_1) \exp(i\mathbf{k}_1(\mathbf{r}' - \mathbf{r}_1)) \times \\
&\qquad\qquad \omega_j(\mathbf{r}' - \mathbf{r}_2) \exp(i\mathbf{k}_2(\mathbf{r}' - \mathbf{r}_2)) d\,\mathbf{r}' d\,\mathbf{r}_1 d\,\mathbf{r}_2 \\
&= -\sum_{ij} \widetilde{\Phi}_{ij}(\mathbf{k}_1 + \mathbf{k}_2)\widetilde{\omega_i}(-\mathbf{k}_1)\widetilde{\omega_j}(-\mathbf{k}_2).
\end{aligned} \tag{C.2}$$

The inverse transform is given by

$$C^{(2)}(\mathbf{r}_1,\mathbf{r}_2) = -\int\int \sum_{ij} \widetilde{\Phi}_{ij}(\mathbf{k}_1+\mathbf{k}_2)\widetilde{\omega_i}(-\mathbf{k}_1)\hat{\omega_j}(-\mathbf{k}_2)\exp(i\mathbf{k}_1\mathbf{r}_1)\exp(i\mathbf{k}_2\cdot\mathbf{r}_2)d\,\mathbf{k}_1 d\,\mathbf{k}_2 \tag{C.3}$$

C.1 Homogeneous cases

In the homogeneous fluid, $\widetilde{\Phi}_{ij}(\mathbf{k}_1+\mathbf{k}_2)$ in Eq. (C.3) is zero unless $\mathbf{k}_1+\mathbf{k}_2=0$ and $C^{(2)}(\mathbf{r}_1,\mathbf{r}_2)$ only depends on $r=|\mathbf{r}_1-\mathbf{r}_2|$, such that

$$C^{(2)}(\mathbf{r}_1,\mathbf{r}_2) = C^{(2)}(r) = -\sum_{ij}\widetilde{\Phi}_{ij}(\mathbf{0})\int \widetilde{\omega_i}(-\mathbf{k})\widetilde{\omega_j}(\mathbf{k})\exp(-i\mathbf{k}\cdot\mathbf{r})d\,\mathbf{k}, \tag{C.4}$$

which is analytically solvable.

In 1D,

$$C^{(2)}(r) = \left(-\frac{1-r\eta}{(1-\eta)^2}\right)\Theta\left(\sigma-r\right) \tag{C.5}$$

In 2D with the FMT free energy functional as Eq. (3.51),

$$C^{(2)}(r) = \left(-\frac{\left(1+\frac{2\eta}{1-\eta}\right)dA(r)}{1-\eta} - \frac{\eta\left(1+\frac{2\eta}{1-\eta}\right)dV(r)}{(1-\eta)^2} - \frac{C_0+C_1y_1(r)+C_2y_1(r)^2}{\pi(1-\eta)y_2(r)}\right)\Theta\left(\sigma-r\right), \tag{C.6}$$

where

$$dA(r) = \frac{2\arccos(r)}{\pi}, \tag{C.7}$$

$$dV(r) = \frac{2}{\pi}\left(\arccos\left(r\right) - r\left(1-r^2\right)\right), \tag{C.8}$$

$$y_1(r) = 1-2r^2, \tag{C.9}$$

$$y_2(r) = \sqrt{1-y_1(r)^2}, \tag{C.10}$$

and C_0, C_1, C_2 as in Eq. (3.52).

Finally, in 3D

$$C^{(2)}(r) = \left(a_1+a_2r+a_3r^3\right)\Theta\left(\sigma-r\right) \tag{C.11}$$

where the coefficients a_i for tensorial White Bear II functional (Eq. (3.46)) read

$$a_1 = -\frac{1+4\eta+4\eta^2-4\eta^3+\eta^4}{(1-\eta)^4}, \tag{C.12}$$

$$a_2 = \frac{-2+25\eta+12\eta^2-10\eta^3+2\eta^4}{3(1-\eta)^4} - 2\frac{\ln 1-\eta}{3\eta}, \tag{C.13}$$

and

$$a_3 = \frac{1-4\eta+2\eta^2-3\eta^3+\eta^4}{(1-\eta)^4} + \frac{\ln 1-\eta}{\eta}, \tag{C.14}$$

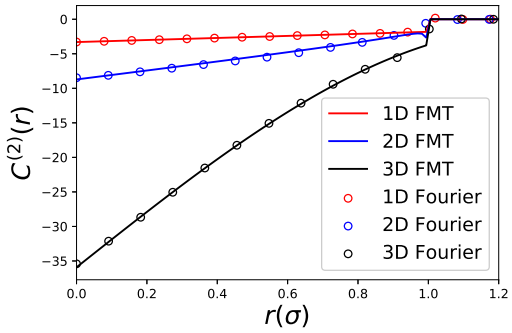

Figure C.1: $C^{(2)}(r)$ with $\eta = 0.45$. In the case of 2D, $a = \frac{11}{4}$. Solid lines are analytical results and circles are numerically obtained by Eq. (C.4).

C.2 Inhomogeneous

For an inhomogeneous fluid, for example, a crystal or fluid under external potential, Eq. (C.3) is already the simplest form. Eq. (C.3) is very challenging in numerical calculation since it is a six–dimensional calculation for 3D HS systems and four–dimensional for a 2D HD systems.

For numerical purpose, Eq. (C.3) is rewritten as

$$C^{(2)}(\mathbf{r}_1, \mathbf{r}_2) = \int J(\mathbf{r}_1, \mathbf{k}_2) \exp(i\mathbf{k}_2 \cdot \mathbf{r}_2) d\,\mathbf{k}_2 \tag{C.15}$$

with

$$J(\mathbf{r}_1, \mathbf{k}_2) = \int \sum_{ij} \widetilde{\Phi}_{ij}(\mathbf{k}_1 + \mathbf{k}_2)\widetilde{\omega_i}(-\mathbf{k}_1)\widetilde{\omega_j}(-\mathbf{k}_2) \exp(i\mathbf{k}_1 \cdot \mathbf{r}_1) d\,\mathbf{k}_1. \tag{C.16}$$

The advantage is that $J(\mathbf{r}_1, \mathbf{k}_2)$ does not depend on $\mathbf{r}_2$; thus, one needs to compute all $J(\mathbf{r}_1, \mathbf{k}_2)$ only once and uses it for all $\mathbf{r}_2$.

C.2.1 Crystal

The phase transition is absent in the 1D system; thus we add an external field and then perform the the free energy minimization. Fig.C.2 shows the equilibrium density profile ρ^{eq} and the external potential V^{ext}.

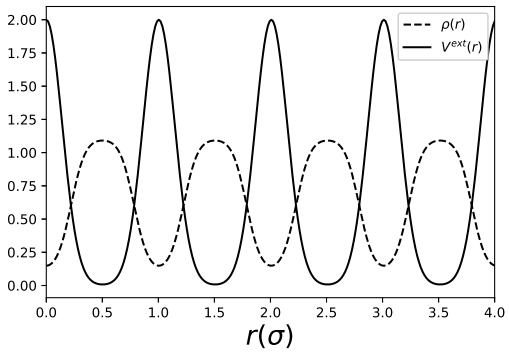

Figure C.2: $\rho^{\text{eq}}(x)$ in 1D under V^{ext}

For 1D HR, computation is rather easy; thus we determine full $C^{(2)}(r_1, r_2)$ and show in Fig.C.3.

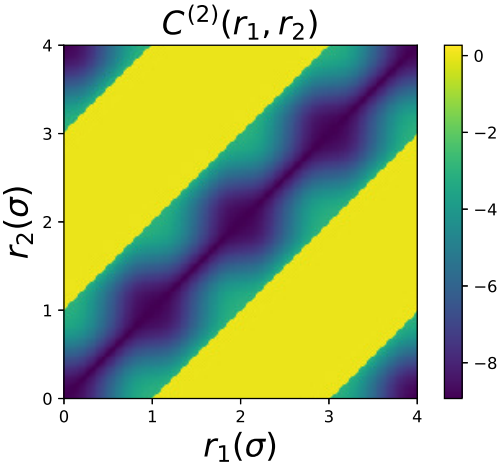

Figure C.3: $C^{(2)}(r_1, r_2)$

Moreover, in 1D, one could also directly determine $C^{(2)}$ by the OZ relation (Chapter 3) with the Percus conditions: $h^{(2)}(r_1, r_2) = -1$ and $C^{(2)}(r_1, r_2) = 0$ if $|r_1 - r_2| < 2R$. The comparison are shown in Fig.C.4.

For 2D and 3D crystal, we obtain the crystal density profiles close to fluid–crystal coexistence and determine $C^{(2)}$ by using Eq. (C.15).The results are shown in Fig. C.5 and C.6.

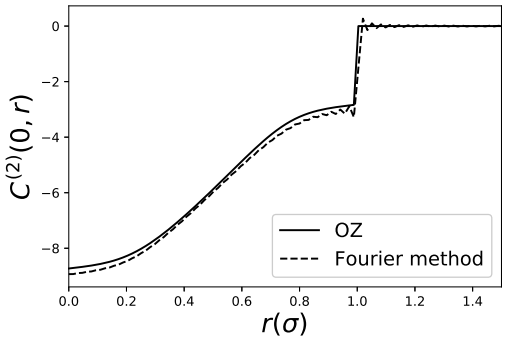

Figure C.4: $C^{(2)}$ obtained by solving the OZ equation and the Fourier method, Eq. (C.3).

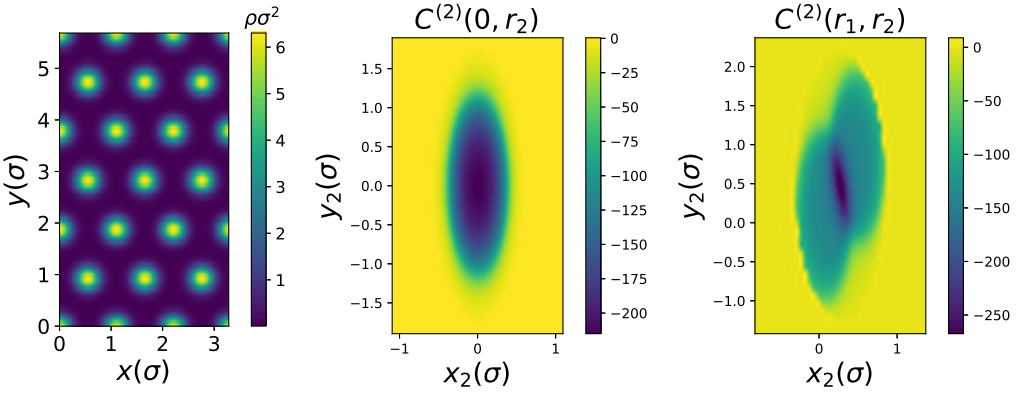

(a) (b) (c)

Figure C.5: 2D HD crystal with $a = 11/4$ and $\eta = 0.732$ (a) density profile. (b)$C^{(2)}$ with $\mathbf{r}_1 = 0$. (c) Same as (b) with $\mathbf{r}_1 = (a_x/4, a_y/4)$ with $a_{x/y}$ in the length of a unit cell in the x/y direction.

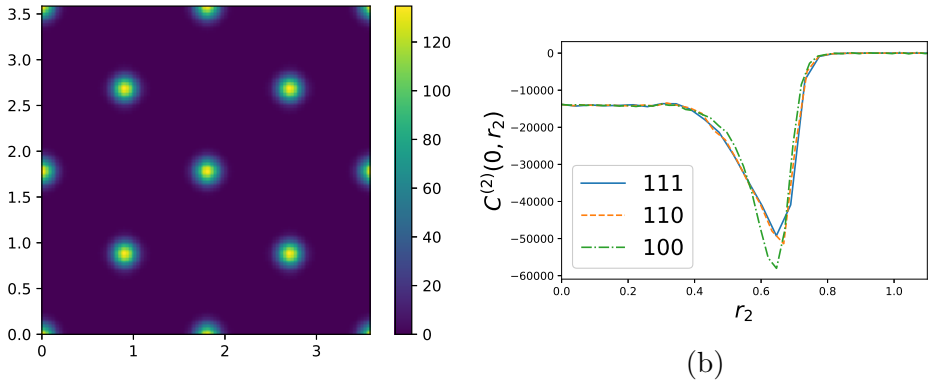

(a) (b)

Figure C.6: $C^{(2)}$ in fcc structure with $\eta = 0.545$ and $n_{\text{vac}} = 2.18 \times 10^{-5}$. (a) density profile in xy–plane. (b) $C^{(2)}$ in three directions with $\mathbf{r}_1 = 0$

C.3 Conclusion

We have successfully obtained the $C^{(2)}$ for homogeneous and inhomogeneous fluid by FMT. However, for the 3D crystal, the requirement for computational resources is still very high, for example the Fig C.6(b) takes one week with 64 GPUs, and the further investigations for the relation between $C^{(2)}$ and macroscopic crystal properties are required.

Bibliography

[1] G. Martius and C. H. Lampert, "Extrapolation and learning equations," *arXiv:1610.02995*, 2016.

[2] S.-C. Lin and M. Oettel, "A classical density functional from machine learning and a convolutional neural network," *SciPost Phys.*, vol. 6, p. 025, 2019.

[3] R. Roth, K. Mecke, and M. Oettel, "Communication: Fundamental measure theory for hard disks: Fluid and solid," *J. Chem. Phys.*, vol. 136, p. 081101, 2012.

[4] Y. Rosenfeld, "Free–energy model for the inhomogeneous hard–sphere fluid mixture and density–functional theory of freezing," *Phys. Rev. Lett.*, vol. 63, no. 9, p. 980, 1989.

[5] Y. Rosenfeld, M. Schmidt, H. Löwen, and P. Tarazona, "Fundamental–measure free–energy density functional for hard spheres: Dimensional crossover and freezing," *Phys. Rev. E*, vol. 55, no. 4, p. 4245, 1997.

[6] P. Tarazona and Y. Rosenfeld, "From zero–dimension cavities to free–energy functionals for hard disks and hard spheres," *Phys. Rev. E*, vol. 55, p. 4873, 1997.

[7] P. Tarazona, "Density functional for hard sphere crystals: A fundamental measure approach," *Phys. Rev. Lett.*, vol. 84, p. 694, 2000.

[8] R. Roth, "Fundamental measure theory for hard–sphere mixtures: a review," *J. Phys.:Condens. Matter*, vol. 22, no. 6, p. 063102, 2010.

[9] J. A. Barker and D. Henderson, "Perturbation theory and equation of state for fluids. II. A successful theory of liquids," *J. Chem. Phys*, vol. 47, no. 11, pp. 4714–4721, 1967.

[10] E. P. Bernard and W. Krauth, "Two–step melting in two dimensions: first–order liquid–hexatic transition," *Phys. Rev. Lett.*, vol. 107, no. 15, p. 155704, 2011.

[11] A. L. Thorneywork, J. L. Abbott, D. G. A. L. Aarts, and R. P. A. Dullens, "Two–dimensional melting of colloidal hard spheres," *Phys. Rev.*, vol. 118, no. 15, p. 158001, 2017.

[12] A. L. Thorneywork, R. Roth, D. G. A. L. Aarts, and R. P. A. Dullens, "Radial distribution functions in a two–dimensional binary colloidal hard sphere system," *J. Chem. Phys.*, vol. 140, p. 161106, 2014.

[13] R. Castaneda-Priego, A. Rodríguez-López, and J. Méndez-Alcaraz, "Depletion forces in two–dimensional colloidal mixtures," *J. Condens. Matter Phys.*, vol. 15, no. 48, p. S3393, 2003.

[14] S. Asakura and F. Oosawa, "On interaction between two bodies immersed in a solution of macromolecules," *J. Chem. Phys*, vol. 22, no. 7, pp. 1255–1256, 1954.

[15] S. Asakura and F. Oosawa, "Interaction between particles suspended in solutions of macromolecules," *J. Polym. Sci.*, vol. 33, no. 126, pp. 183–192, 1958.

[16] J. C. Snyder, M. Rupp, K. Hansen, K.-R. Müller, and K. Burke, "Finding density functionals with machine learning," *Phys. Rev. Lett.*, vol. 108, p. 253002, 2012.

[17] L. Li, J. C. Snyder, I. M. Pelaschier, J. Huang, U.-N. Niranjan, P. Duncan, M. Rupp, K.-R. Müller, and K. Burke, "Understanding machine–learned density functionals," *Int. J. Quantum Chem.*, vol. 116, p. 819, 2016.

[18] F. Brockherde, L. Vogt, L. Li, M. E. Tuckerman, K. Burke, and K.-R. Müller, "Bypassing the Kohn–Sham equations with machine learning," *Nat. Commun.*, vol. 8, p. 872, 2017.

[19] J. Nelson, R. Tiwari, and S. Sanvito, "Machine learning density functional theory for the hubbard model," *Phys. Rev. B*, vol. 99, p. 075132, 2019.

[20] M. Bishop, "WCA perturbation theory for onedimensional Lennard–Jones fluids," *Am. J. Phys.*, vol. 52, p. 158, 1984.

[21] M. Schmidt and H. Lipson, "Distilling free–form natural laws from experimental data," *Science*, vol. 324, p. 81, 2009.

[22] S. S. Sahoo, C. H. Lampert, and G. Martius, "Learning equations for extrapolation and control," in *Proceedings of the 35th International Conference on Machine Learning*, vol. 80, pp. 4439–4447, PMLR, 10–15 Jul 2018.

[23] J.-P. Hansen and I. R. McDonald, *Theory of simple liquids: With applications to soft matter*. Academic Press, 2013.

[24] P. Hohenberg and W. Kohn, "Inhomogeneous electron gas," *Phys. Rev.*, vol. 136, p. B864, 1964.

[25] N. D. Mermin, "Thermal properties of the inhomogeneous electron gas," *Physical Review*, vol. 137, no. 5A, p. A1441, 1965.

[26] R. Evans, "The nature of the liquid–vapour interface and other topics in the statistical mechanics of non–uniform, classical fluids," *Adv. Phys*, vol. 28, no. 2, pp. 143–200, 1979.

[27] T. Ramakrishnan and M. Yussouff, "First–principles order–parameter theory of freezing," *Physical Review B*, vol. 19, no. 5, p. 2775, 1979.

[28] Y. C. Chiew, "Percus–Yevick integral–equation theory for athermal hard–sphere chains: Part I: Equations of state," *Mol. Phys.*, vol. 70, no. 1, pp. 129–143, 1990.

[29] H. Hansen-Goos and R. Roth, "Density functional theory for hard–sphere mixtures: The white bear version mark II," *J. Phys. Condens. Matter*, vol. 18, no. 37, p. 8413, 2006.

[30] H. Hansen-Goos and R. Roth, "A new generalization of the Carnahan–Starling equation of state to additive mixtures of hard spheres," *J. Chem. Phys*, vol. 124, no. 15, p. 154506, 2006.

[31] M. Oettel, S. Görig, A. Härtel, H. Löwen, M. Radu, and T. Schilling, "Free energies, vacancy concentrations, and density distribution anisotropies in hard–sphere crystals: A combined density functional and simulation study," *Phys. Rev. E*, vol. 82, no. 5, p. 051404, 2010.

[32] A. Härtel, M. Oettel, R. E. Rozas, S. U. Egelhaaf, J. Horbach, and H. Löwen, "Tension and stiffness of the hard sphere crystal–fluid interface," *Phys. Rev. Lett.*, vol. 108, p. 226101, 2012.

[33] P. Tarazona, J. A. Cuesta, and Y. Martínez-Ratón, "Density functional theories of hard particle systems," in *Theory and Simulation of Hard–Sphere Fluids and Related Systems*, pp. 247–341, Springer, 2008.

[34] J. K. Percus, "Equilibrium state of a classical fluid of hard rods in an external field," *J. Stat. Phys.*, vol. 15, no. 6, pp. 505–511, 1976.

[35] M. Oettel, S. Dorosz, M. Berghoff, B. Nestler, and T. Schilling, "Description of hard–sphere crystals and crystal–fluid interfaces: A comparison between density functional approaches and a phase–field crystal model," *Phys. Rev. E*, vol. 86, no. 2, p. 021404, 2012.

[36] J. Mellenthin, A. Karma, and M. Plapp, "Phase–field crystal study of grain–boundary premelting," *Physical Review B*, vol. 78, no. 18, p. 184110, 2008.

[37] A. Adland, A. Karma, R. Spatschek, D. Buta, and M. Asta, "Phase–field–crystal study of grain boundary premelting and shearing in bcc iron," *Phys. Rev. B*, vol. 87, no. 2, p. 024110, 2013.

[38] R. C. Tolman, "Consideration of the Gibbs theory of surface tension," *J. Chem. Phys*, vol. 16, no. 8, pp. 758–774, 1948.

[39] R. C. Tolman, "The effect of droplet size on surface tension," *J. Chem. Phys*, vol. 17, no. 3, pp. 333–337, 1949.

[40] G. I. Tóth and L. Gránásy, "Crystal nucleation in the hard–sphere system revisited: A critical test of theoretical approaches," *J. Phys. Chem. B*, vol. 113, no. 15, pp. 5141–5148, 2009.

[41] P. Montero de Hijes, J. R. Espinosa, V. Bianco, E. Sanz, and C. Vega, "Interfacial free energy and tolman length of curved liquid–solid interfaces from equilibrium studies," *J. Phys. Chem. C*, vol. 124, no. 16, pp. 8795–8805, 2020.

[42] A. Cacciuto, S. Auer, and D. Frenkel, "Solid–liquid interfacial free energy of small colloidal hard–sphere crystals," *J. Chem. Phys*, vol. 119, no. 14, pp. 7467–7470, 2003.

[43] P. R. ten Wolde and D. Frenkel, "Computer simulation study of gas–liquid nucleation in a Lennard–Jones system," *J. Chem. Phys*, vol. 109, no. 22, pp. 9901–9918, 1998.

[44] M. Moody and P. Attard, "Curvature dependent surface tension from a simulation of a cavity in a Lennard–Jones liquid close to coexistence," *J. Chem. Phys*, vol. 115, no. 19, pp. 8967–8977, 2001.

[45] J. C. Barrett, "Some estimates of the surface tension of curved surfaces using density functional theory," *J. Chem. Phys*, vol. 124, no. 14, p. 144705, 2006.

[46] N. Bruot and F. Caupin, "Curvature dependence of the liquid–vapor surface tension beyond the tolman approximation," *Phys. Rev. Lett.*, vol. 116, no. 5, p. 056102, 2016.

[47] A. Tröter, F. Schmitz, P. Virnau, and K. Binder, "Equilibrium between a droplet and surrounding vapor: A discussion of finite size effects," *J. Phys. Chem. B*, vol. 122, no. 13, pp. 3407–3417, 2017.

[48] A. Tröster and K. Binder, "Positive Tolman length in a lattice gas with three–body interactions," *Phys. Rev.*, vol. 107, no. 26, p. 265701, 2011.

[49] J. M. Kosterlitz and D. Thouless, "Long range order and metastability in two dimensional solids and superfluids. (Application of dislocation theory)," *J Phys C: Solid State Phys*, vol. 5, no. 11, p. L124, 1972.

[50] J. M. Kosterlitz and D. J. Thouless, "Ordering, metastability and phase transitions in two–dimensional systems," *J Phys C: Solid State Phys*, vol. 6, no. 7, p. 1181, 1973.

[51] B. Halperin and D. R. Nelson, "Theory of two–dimensional melting," *Phys. Rev. Lett.*, vol. 41, no. 2, p. 121, 1978.

[52] D. R. Nelson and B. Halperin, "Dislocation–mediated melting in two dimensions," *Physical Review B*, vol. 19, no. 5, p. 2457, 1979.

[53] A. Young, "Melting and the vector Coulomb gas in two dimensions," *Physical Review B*, vol. 19, no. 4, p. 1855, 1979.

[54] K. J. Strandburg, "Two–dimensional melting," *Rev. Mod. Phys.*, vol. 60, no. 1, p. 161, 1988.

[55] S.-C. Lin and M. Oettel, "Phase diagrams and crystal–fluid surface tensions in additive and nonadditive two–dimensional binary hard–disk mixtures," *Phys. Rev. E*, vol. 98, no. 1, p. 012608, 2018.

[56] J. M. Brader, R. Evans, and M. Schmidt, "Statistical mechanics of inhomogeneous model colloid–polymer mixtures," *Mol. Phys.*, vol. 101, p. 3349, 2003.

[57] M. Mortazavifar and M. Oettel, "A fundamental measure density functional for fluid and crystal phases of the Asakura–Oosawa model," *J. Phys.:Condens. Matter*, vol. 28, no. 24, p. 244018, 2016.

[58] C. N. Likos and C. L. Henley, "Complex alloy phases for binary hard–disc mixtures," *Philos. Mag. B*, vol. 68, p. 85, 1993.

[59] J. Russo and N. B. Wilding, "Disappearance of the hexatic phase in a binary mixture of hard disks," *Phys. Rev. Lett.*, vol. 119, no. 11, p. 115702, 2017.

[60] W. G. T. Kranendonk and D. Frenkel, "Computer simulation of solid–liquid coexistence in binary hard sphere mixtures," *Mol. Phys.*, vol. 72, p. 679, 1991.

[61] M. Oettel, "Mode expansion for the density profiles of crystal–fluid interfaces: hard spheres as a test case," *J. Phys.:Condens. Matter*, vol. 24, no. 46, p. 464124, 2012.

[62] R. L. Vink, T. Neuhaus, and H. Löwen, "Fluid phase separation inside a static periodic field: An effectively two–dimensional critical phenomenon," *J. Chem. Phys.*, vol. 134, no. 20, p. 204907, 2011.

[63] A. E. Gonzalez, "Colloidal crystallization in 2D for short–ranged attractions: A descriptive overview," *Crystals*, vol. 6, p. 46, 2016.

[64] M. Amini and B. B. Laird, "Crystal–melt interfacial free energy of binary hard spheres from capillary fluctuations," *Phys. Rev. B*, vol. 78, p. 144112, 2008.

[65] C. A. Becker, D. L. Olmsted, M. Asta, J. J. Hoyt, and S. M. Foiles, "Atomistic simulations of crystal–melt interfaces in a model binary alloy: Interfacial free energies, adsorption coefficients, and excess entropy," *Phys. Rev. B*, vol. 79, p. 054109, 2009.

[66] J. Percus, "Entropy of a non–uniform one–dimensional fluid," *J. Condens. Matter Phys.*, vol. 1, no. 17, p. 2911, 1989.

[67] M. A. Kramer, "Nonlinear principal component analysis using autoassociative neural networks," *AIChE journal*, vol. 37, no. 2, pp. 233–243, 1991.

[68] P. Mehta, M. Bukov, C.-H. Wang, A. G. Day, C. Richardson, C. K. Fisher, and D. J. Schwab, "A high–bias, low–variance introduction to machine learning for physicists," *Phys. Rep.*, 2019.

[69] M. Abadi, A. Agarwal, P. Barham, E. Brevdo, Z. Chen, C. Citro, G. S. Corrado, A. Davis, J. Dean, M. Devin, S. Ghemawat, I. Goodfellow, A. Harp, G. Irving, M. Isard, Y. Jia, R. Jozefowicz, L. Kaiser, M. Kudlur, J. Levenberg, D. Mané, R. Monga, S. Moore, D. Murray, C. Olah, M. Schuster, J. Shlens, B. Steiner, I. Sutskever, K. Talwar, P. Tucker, V. Vanhoucke, V. Vasudevan, F. Viégas, O. Vinyals, P. Warden, M. Wattenberg, M. Wicke, Y. Yu, and X. Zheng, "TensorFlow: Large–scale machine learning on heterogeneous systems," 2015. Software available from tensorflow.org.

[70] A. Paszke, S. Gross, F. Massa, A. Lerer, J. Bradbury, G. Chanan, T. Killeen, Z. Lin, N. Gimelshein, L. Antiga, *et al.*, "Pytorch: An imperative style, high–performance deep learning library," in *Advances in neural information processing systems*, pp. 8026–8037, 2019.

[71] A. J. Archer, B. Chacko, and R. Evan, "The standard mean–field treatment of inter–particle attraction in classical dft is better than one might expect," *J. Chem. Phys.*, vol. 147, p. 034501, 2017.

[72] K. R. Elder, N. Provatas, J. Berry, P. Stefanovic, and M. Grant, "Phase–field crystal modeling and classical density functional theory of freezing," *Phys. Rev. B*, vol. 75, no. 6, p. 064107, 2007.

[73] M. Wertheim, "Fluids with highly directional attractive forces. i. Statistical thermodynamics," *J. Stat. Phys.*, vol. 35, no. 1–2, pp. 19–34, 1984.

[74] D. Stopper, F. Hirschmann, M. Oettel, and R. Roth, "Bulk structural information from density functionals for patchy particles," *J. Chem. Phys*, vol. 149, no. 22, p. 224503, 2018.

[75] S.-C. Lin, G. Martius, and M. Oettel, "Analytical classical density functionals from an equation learning network," *J. Chem. Phys*, vol. 152, no. 2, p. 021102, 2020.

[76] H. Hansen-Goos and K. Mecke, "Fundamental measure theory for inhomogeneous fluids of nonspherical hard particles," *Phys. Rev. Lett.*, vol. 102, p. 018302, 2009.

[77] R. Wittmann, M. Marechal, and K. Mecke, "Fundamental mixed measure theory for non–spherical colloids," *EPL*, vol. 109, p. 26003, 2015.

[78] M. Oettel, M. Klopotek, M. Dixit, E. Empting, T. Schilling, and H. Hansen-Goos, "Monolayers of hard rods on planar substrates: I. Equilibrium," *J. Chem. Phys.*, vol. 145, p. 074902, 2016.

[79] D. P. Kingma and J. Ba, "Adam: A method for stochastic optimization," *arXiv:1412.6980*, 2014.

[80] R. Tibshirani, "Regression shrinkage and selection via the lasso," *J. R. Stat. Soc. Series B Stat. Methodol.*, pp. 267–288, 1996.

[81] J. A. Cuesta and A. Sánchez, "General non–existence theorem for phase transitions in one–dimensional systems with short range interactions, and physical examples of such transitions," *J. Stat. Phys.*, vol. 115, no. 3–4, pp. 869–893, 2004.

[82] V. P. Sergiievskyi, G. Jeanmairet, M. Levesque, and D. Borgis, "Fast computation of solvation free energies with molecular density functional theory: Thermodynamic–ensemble partial molar volume corrections," *J. Phys. Chem. Lett.*, vol. 5, no. 11, pp. 1935–1942, 2014.

[83] G. Jeanmairet, M. Levesque, R. Vuilleumier, and D. Borgis, "Molecular density functional theory of water," *J. Phys. Chem. Lett.*, vol. 4, no. 4, pp. 619–624, 2013.

[84] G. Jeanmairet, M. Levesque, and D. Borgis, "Molecular density functional theory of water describing hydrophobicity at short and long length scales," *J. Chem. Phys.*, vol. 139, no. 15, p. 154101, 2013.

[85] M. Mortazavifar, *Equilibrium properties of crystals in the hard–sphere and the Asakura–Oosawa Model.* PhD thesis, Eberhard Karls Universität Tübingen, 2016.

[86] T. Bernet, E. A. Müller, and G. Jackson, "A tensorial fundamental measure density functional theory for the description of adsorption in substrates of arbitrary three–dimensional geometry," *J. Chem. Phys*, vol. 152, no. 22, p. 224701, 2020.

[87] M. Frigo and S. G. Johnson, "FFTW user's manual," *Massachusetts Institute of Technology*, 1999.

[88] D. Stopper and R. Roth, "Massively parallel GPU–accelerated minimization of classical density functional theory," *J. Chem. Phys.*, vol. 147, no. 6, p. 064508, 2017.

[89] S. Johnson, "Notes on FFT–based differentiation," 2011. Available from `https://math.mit.edu/~stevenj/notes.html`.

[90] A. Härtel, *Density functional theory of hard colloidal particles: From bulk to interfaces*. PhD thesis, Universität Düsseldorf, 2013.

[91] P. Pulay, "Convergence acceleration of iterative sequences. the case of SCF iteration," *Chem. Phys. Lett.*, vol. 73, no. 2, pp. 393–398, 1980.

[92] S. A. Orszag, "Numerical methods for the simulation of turbulence," *Phys. Fluids*, vol. 12, no. 12, pp. II–250, 1969.

Acknowledgment

In July 2016, I moved to Tübingen, Germany. At that time I joined a language school and searched for Ph.D. positions. Fortunately, Prof. Dr. Martin Oettel offered me a research assistant work and helped me applying for scholarships. In April 2017, I obtained the state fund scholarship (Landesgraduiertenförderungsgesetzes) from Baden–Württemberg and started my Ph.D. works.

In the beginning, Martin suggested tackling dynamic density functional theory (DDFT) for hard–spheres crystals. With certain investigations and improvements, we were able to stabilize the crystals but crystal-fluid interfaces are still unstable. After about six months, we shifted to two–dimensional hard–disk binary systems, where the numerical difficulty is much lower and thus we systemically investigated the phase-diagrams and crystal–fluid interfaces.

By the time summarizing and publishing the results of hard–disks mixtures, I started thinking whether there is a better way to obtain the free energy functionals for *arbitrary* particle–particle interactions. This is a decades–long problem in DFT: how to go beyond mean–field approximation? While there are almost exact functionals for hard–spheres systems, the tail parts that treated by the mean–field approximation always spoils the accuracy of the functional. In December 2017, Dr. Daniel de las Heras was invited to give a talk about using machine learning to obtain the external potential by density distributions. At the end of the talk, Prof. Dr. Roth asked: "Can machine learning give us density functionals ?". This question became a seed in my mind. After about one–month literature research and some preliminary results, Martin was convinced that it is worth investigating more. After that, we published the first paper that uses convolutional networks to obtain the explicit functionals with simple ansätze. Furthermore, we collaborated with Dr. Georg Martius to extend the flexibility and reliability of the network and learned functionals.

I want to thanks Dr. Mortazavifar, Dr. Joachim Schöpe, Dr. Bleibel and Dr. Stopper for their insightful discussions and constructive suggestions. I

also thank my dear colleagues Miriam, Paul, Frank, Eelo, Malte, and Manuel for their supports in this thesis and helps me understanding German culture; especially Miriam, without her I probably gave up the ML ideas already.

I thank my supervisor, Prof. Dr. Martin Oettel for his enthusiastic cooperation, deep understanding of colloid systems, constructive discussions, great support and thoughtful help throughout my Ph.D. studies. Without him, I have no chance to do my Ph.D. I acknowledge my second supervisor Prof. Dr. Roth, who helps me for achieving a deeper understanding of DFT. Also, I acknowledge Dr. Georg Martius, who helps me improving my ML knowledge.